MR Relaxation, Diffusion, and Stiffness Characterization of Engineered Cartilage Tissue

BY

Ziying Yin
B.S., Beijing Jiaotong University, 2006
M.S., Beijing Jiaotong University, 2008

THESIS

Submitted as partial fulfillment of the requirements
for the degree of Doctor of Philosophy in Bioengineering
in the Graduate College of the
University of Illinois at Chicago, 2014

Chicago, Illinois

Defense Committee:

Richard L. Magin, Chair and Advisor
Thomas J. Royston
Xiaohong J. Zhou
Robert Kleps, Research Resource Center
Thomas M. Schmid, Rush University

This thesis is dedicated to my parents for their endless love and their warm affection.

ACKNOWLEDGMENTS

First and foremost, I would like to express my deepest gratitude to my advisor, Dr. Richard L. Magin for his guidance over the last five years. He is the one who has taught me not only the knowledge of MRI, but also much about being a good scientist. He provided me with the opportunity to carry out this research, shared his ideas and vision with me, and motivated me to finish it. He let me fly on my own but being ever present for advice and support. I could not have asked a better advisor like him!

Secondly, I would like to acknowledge and thank the other members of my thesis committee: Dr. Thomas M. Schmid for providing me with such a wonderful culture system for my MRI research. I am very appreciative of all he has done – all support and countless hours contribution – to help me complete this project. I have benefited from the expertise of Dr. Robert Kleps, who has taught me the very first MRI scan. Dr. Xiaohong J. Zhou and Dr. Thomas J. Royston, their myriad experience with MRI and MRE have helped me to see my project in a more comprehensive vision. I am grateful for all the time, effort, and suggestions they have made.

I would like to extend my acknowledgement to Dr. Dieter Klatt for his kind support and guidance in the last of my PhD year. I have had such good opportunities to learn MRE from him, and to discuss my research with him.

ACKNOWLEDGMENTS (continued)

I also express my sincere appreciation to Dr. Weiguo Li, Yi Sui, and Dr. Temel K. Yasar, for their kind help and support. Dr. Li and Yi's considerable expertise in MRI experiment and Dr. Yasar's innumerable contributions to MRE experiment have greatly extended my knowledge of MRI and MRE.

No research can be done without help from my colleagues. I would like to thank all the people who have helped me with my Ph.D. study: Allen Ye, Yifei Liu, Steven Kearney, Benjamin Schwartz, Dr. Mrignayani Kotecha, Altaf Khan, Spencer Brinker, and others, for their ideas and discussions.

Lastly, I would like to thank my family, whose love and support have always helped me keep the right perspective. I would especially like to thank Yi Sui again, for his love, immense patience during these past 3 years, and support in every aspect of my life.

I am thankful for all the wonderful people I have met here, who have made this journey so much more enjoyable!

ZY

In this thesis, the portion of Chapter 5 has been published previously in Mary Ann Liebert, Inc. The portion of Chapter 6 has been published previously in John Wiley and Sons**.**

CONTRIBUTION OF AUTHORS

Chapter 1 is a background introduction that highlights the significance of my research. **Chapter 2** and **Chapter 3** describe the theoretical background of my research. **Chapter 4** represents a series my own unpublished experiments directed at MR relaxation and diffusion characterization of engineered cartilage tissue. **Chapter 5** represents a published manuscript (**reference 115**) for which I was the primary author and major driver of the research. Dr. Thomas Schmid provided the tissue-engineered cartilage for MR characterization, and performed the biochemical analyses. Dr. Temel Yasar developed the geometric focusing micro-MRE actuation setup. Yifei Liu assisted me in the experiments. Dr. Thomas Royston, and my research advisor, Dr. Richard Magin contributed to the writing of the manuscript. **Chapter 6** represents two new techniques, one was published (**reference 116**) for which I was the primary author and major driver of the research. Dr. Dieter Klatt proposed the idea of dMRE. Dr. Dieter Klatt and my advisor, Dr. Richard Magin contributed to the writing of the manuscript. The second technique, $T_{1\rho}$-MRE is my own unpublished technique that directed at simultaneous acquisition of $T_{1\rho}$ and MRE. I anticipate that this line of research will be continued in the laboratory after I leave and that this work will ultimately be published as part of a co-authored manuscript. **Chapter 7** represents my synthesis of the research presented in this thesis and my conclusions. The future directions of this field are discussed.

TABLE OF CONTENTS

LIST OF TABLES

LIST of FIGURES

FIGURE PAGE

LIST OF ABBREVIATIONS

AC	Articular Cartilage
ADC	Apparent Diffusion Coefficient
CS	Chondroitin Sulfate
CPMG	Carr-Purcell-Meiboom-Gill
DMEM	Dulbecco's Modified Eagle's Medium
dMRE	Diffusion-MRE
dMSG	Diffusion Motion Sensitizing Gradient
DTI	Diffusion Tensor Imaging
DWI	Diffusion-weighted Imaging
DZ	Deep Zone
ECM	Extracellular Matrix
ETL	Echo Train Length
FOV	Field of View
FSE	Fast Spin Echo
GAG	Glycosaminoglycan
IHC	Immunohistochemical

LIST OF ABBREVIATIONS (continued)

LFE	Local Frequency Estimation
MR	Magnetic Resonance
MRE	Magnetic Resonance Elastography
MRI	Magnetic Resonance Imaging
MSG	Motion-sensitizing Gradient
MEG	Motion-encoding Gradient
PDW	Proton Density Weighted
PG	Proteoglycan
PGSE	Pulsed Gradient Spin-echo
RF	Radio Frequency
SE	Spin Echo
SL	Spin-locking
SZ	Superficial Zone
TE	Echo Time
TR	Repetition Time
TSL	Time of Spin-Locking

LIST OF ABBREVIATIONS (continued)

TZ	Transitional Zone
WW	Wet Weight

SUMMARY

The primary goal of this thesis is to develop a combined MR relaxation (T_2 and $T_{1\rho}$), diffusion (ADC, apparent diffusion coefficient), and elastography (shear stiffness) method to fully characterize the development of tissue-engineered cartilage in terms of the changes in its composition, structure, and mechanical properties during tissue growth. We do this for the purpose of understanding how we may better use MR-based methodologies to noninvasively monitor and optimize the cartilage tissue engineering process without sacrificing the constructs.

While conventional T_2 and ADC have been widely used in the studies of engineered cartilage tissues, there were few $T_{1\rho}$ and MRE studies related to it. We begin by demonstrating the potential capabilities of T_2, $T_{1\rho}$, ADC, and shear stiffness in characterization of a scaffold-free engineered cartilage tissue. We examine the correlations between MR parameters and biochemical determined macromolecule contents in tissue-engineered cartilage. We show that, in addition to the conventional T_2 and ADC, $T_{1\rho}$ and MRE can be used as potential biomarkers to assess the specific changes in proteoglycan content and mechanical properties of engineered cartilage during tissue growth.

Secondly, to increase the efficiency of MR characterization of engineered tissues, we develop two new methodologies for simultaneous acquisition of MRI and MRE data: (1) diffusion and MRE (dMRE) and (2) $T_{1\rho}$ and MRE ($T_{1\rho}$-MRE), respectively. Conventional $T_{1\rho,}$ diffusion, and MRE acquisitions are performed as separate measurements that prolong the imaging protocols. The dMRE and $T_{1\rho}$-

MRE are developed to overcome this problem by acquiring two pieces of information in one temporally resolved scan. This allows the simultaneous characterization of both biochemical and mechanical properties of engineered cartilage tissues. We carry out dMRE and $T_{1\rho}$-MRE experiments on tissue-mimicking phantoms to show the feasibilities of two techniques. The results obtained show a good correspondence between simultaneous acquisitions and conventional separate acquisition methods. We expect that the combined MRI/MRE methods will benefit the optimal cartilage tissue engineering process.

1 INTRODUCTION

1.1 Background

Musculoskeletal disorders affect nearly one in three Americans annually, with injuries to cartilage having a higher incidence among these afflictions (1). It has been reported that 22.7% (52.5 million) of U.S. adults reported doctor-diagnosed arthritis from 2010-2012 (2). Due to the avascular nature of articular cartilage, cartilage defects often heal poorly. Current clinical treatments for these injuries include bone marrow stimulation procedure, autologous chondrocyte implantation, osetochondral autograft transfer, engineered cartilage replacement, etc. (3-5). In particular, cartilage tissue engineering promises to repair the damaged cartilage by developing a functional tissue-engineered graft.

1.1.1 Articular Cartilage

Synovial joints (ankle, elbow, hip, knee, shoulder, and those of the fingers and wrists) enable normal, pain-free movement. Under healthy conditions, they function in a nearly frictionless and almost entirely wear-resistant manner. The tissue that contributes the most to these extraordinary functional capacities is the articular cartilage (AC) that forms the bearing surface of all synovial joints.

AC is a thin layer (~ 0.5-5 mm thick) of heterogeneous connective tissue, and consists of sparsely distributed cells called chondrocytes (~ 1%) that are embedded in an extensive extracellular matrix (ECM) as shown in ***Figure 1.1***. The major component of matrix is tissue fluid (~ 60-85% of wet weight), and the

remainder is mostly solid macromolecules, including type II collagen fibers (~ 15-22% of wet weight) and large aggregating proteoglycans (PG) (~ 4-7% of wet weight) (6,7). The type II collagen forms the primary component of the cross-banded fibrils that give cartilage its form and tensile strength. PGs bind to collagen or become mechanically entrapped within the collagenous network to enhance the network strength and stiffness. The tissue fluid that mainly contains water and a high concentration of cations fills this molecular framework. A high density of fixed negative charges associated with PGs attract positive charged ions and repel negative charged ions, which makes the cartilage matrix exhibiting a significant Donnan osmotic pressure effect and thus giving the tissue its compressive strength (6,7).

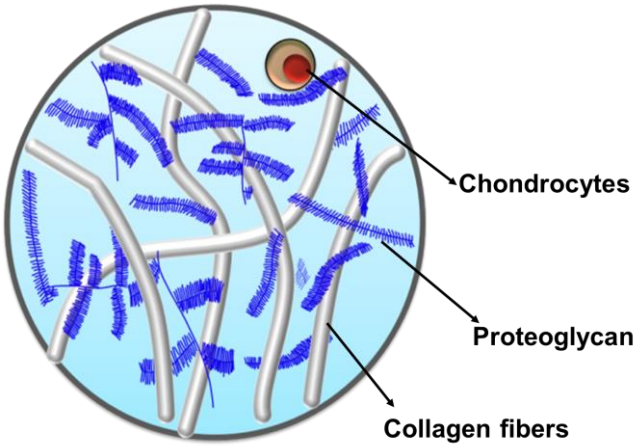

Figure 1.1. Schematic diagram of extracellular matrix of native articular cartilage tissue with chondrocytes, proteoglycans, and type II collagen fibers.

The composition and organization of cartilage matrix vary with the depth from the articular surface to the subchondral bone. It has been suggested that AC can be identified as four zones or layers: the superficial zone (SZ), the transitional zone (TZ), the deep zone (DZ), and the calcified cartilage zone (6,7). The collagen content is highest in the SZ, and lower in the TZ and DZ. The PG is inversely related to the collagen content, being lowest in the SZ and higher in the TZ and DZ. Water content variations reflect those seen for collagen, being the highest at the surface and decreasing in the deep zone. Moreover, the collagen fibrils are organized parallel to the articular surface in the SZ, randomly in the TZ, and perpendicular to the surface in the DZ as illustrated in ***Figure 1.2***. The layer appearance of cartilage ultrastructure is suggested to respond differently to mechanical loadings (6). For example, the dense mat of collagen fibrils lying parallel to the joint surface in the SZ serves as a gliding surface to joint, and may resist shear stresses generated during motions; the perpendicular collagen fibrils with the highest concentration of PGs could distribute loads and resist compression. This unique framework of ECM gives the cartilage its mechanical properties of stiffness and resilience.

Cartilage has been reported to experience degeneration as a consequence of normal aging, degenerative joint diseases, or acute joint injury (8). In the event of degeneration, the failure of the bearing surface of cartilage means the failure of the bearing to provide its essential functions. Unfortunately, the avascular nature of cartilage limits the self-repair of the degraded or damaged cartilage. The cartilage defects generally do not heal, or heal only partially under certain

biological conditions (9). Therefore, repair of articular cartilage becomes an enormous medical problem – the number of U.S. adults with cartilage degeneration is projected to rise to 67 million by 2030 (10).

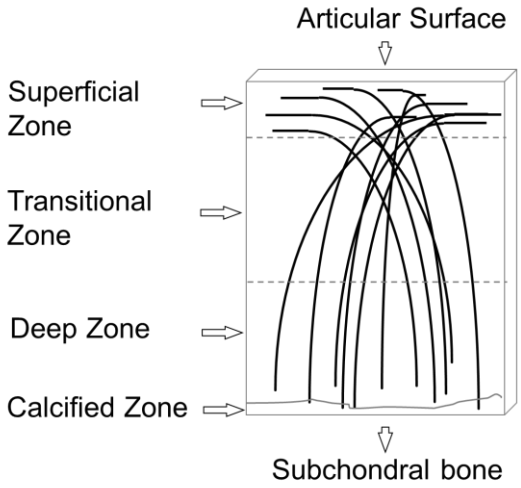

Figure 1.2. Schematic diagram of the organization of the collagen network throughout the different zones of native articular cartilage.

1.1.2 Cartilage Tissue Engineering

Cartilage tissue engineering, as one of the most interesting regenerative techniques, has been developed to replace cartilage defect with a newly grown tissue. Since being introduced in Sweden in 1987, this cell-based approach has gained increasing acceptance (11-13). It combined the cell therapy, scaffolds as well as various signal factors, alone or in combination. The optimal cell source for cartilage tissue engineering is still being identified. Chondrocytes, fibroblasts, and stem cells have all been explored for their potential for cartilage repair (14). The

cells can be either seeded into scaffolds or totally scaffold-free. Scaffolds are produced from natural or synthetic biomaterials and can be in the forms of hydrogels, sponges, meshes, or nanofibers (15,16). Bioscaffolds are selected based on their abilities 1) to maintain the chondrocytic phenotype and promote the ECM production, 2) to provide the requisite degree of mechanical integrity, and 3) to be non-toxic, sterile, biodegradable, and biocompatible. In contrast to the use of scaffolds, the scaffold-free tissue-engineered cartilage is proposed to avoid the complexities (e.g., immune/inflammatory responses, biocompatibility, and biodegradability) arise in the use of foreign substances to the subsequent implantation. In addition to the cell sources and scaffold types, various chemical or mechanical stimulating factors have employed to induce, accelerate, and/or enhance hyaline-like cartilage formation (14,16).

1.2 Motivation

While various cartilage tissue engineering approaches have been developed over the years that aim to restore the articular surface with a hyaline-like tissue, optimal strategies are not yet fully established for complete repair, regeneration, or replacement (13,17). Improvements in these techniques with new cell types, scaffolds, growth factors, and mechanical stimuli are currently being investigated as promising solutions to further improve the treatment of cartilage injures (13,18). There is thus a need for clinicians and researchers to evaluate new regenerative approaches to show clearly advantages and disadvantages with respect to the more traditional approaches.

The common ways to assess the regenerated cartilage tissues are through the use of microscopy and histology; the mechanical properties are typically measured by compressive, tensile, and/or shear mechanical testing (19,20). These techniques are informative and quantitative, but commonly destructive and non-localized. While attempting to recreate functional tissues, we really want to know how we can monitor developing tissue structure without damaging it. How can we assess with confidence that our measurements truly reflect the underlying tissue structure? Moverover, how can we control and optimize the repair and regeneration processes? Noninvasive imaging characterization methods are therefore an essential adjunct to follow the progress of tissue growth and maturation.

Since the first magnetic resonance (MR) image of a phantom in 1973 (21) and its introduction into clinical practice in the 1980s, MR imaging (MRI) has evolved into a powerful and noninvasive medical imaging technique with high spatial resolution, versatile soft-tissue contrast, and full 3D capabilities. The contrast of MRI can be tuned into different aspects of tissue properties from chemical composition to structural information and to mechanical properties. Specifically, MR relaxation times (e.g., spin-spin relaxation time T_2 and spin-lattice relaxation time in the rotating frame $T_{1\rho}$) have been shown to reflect the chemical compositions of biological tissues (22,23); water apparent diffusion coefficient (ADC) can be used to probe the tissue microstructure (24); and MR elastography (MRE) as a phase-contrast based MRI technique, is rapidly being employed to assess the mechanical properties of soft tissues via measurement of shear

properties (25,26). These MR-derived parameters are thus of great value in the evaluation of changes of biochemical and mechanical properties associated with the engineered cartilage tissue maturation.

In cartilage tissue engineering, one of the successful culture approaches is able to regenerate a tissue that can synthesize cartilage-specific molecules (e.g., type II collagen and PG) and then closely resemble native tissue in its composition and structure. Besides that, the knowledge of mechanical properties of tissue-engineered cartilage is essential, because an ideal engineered implant would not only closely resemble the native tissue in its matrix composition, but also mimic its mechanical capability of withstanding the large content stresses and strains. It is thus expected that MR relaxation, diffusion, and elastography can provide such thorough and quantitative characterization of engineered cartilage tissues without sacrifice and staining.

1.3 Dissertation Objectives

The formation of engineered cartilage is a process of remodeling the ECM in which PG and collagen accumulation are major markers. MR relaxation time (T_2 and $T_{1\rho}$), ADC, and shear stiffness of tissue can provide quantitative information that is highly correlated with tissue-level alterations in composition, structure, and mechanical properties. Among all these MR-derived parameters, while conventional T_2 and ADC have been widely used in the studies of engineered cartilage tissues (27,28), there were few $T_{1\rho}$ and MRE studies related to it.

Therefore, the **first objective** of this study is, in addition to the conventional T_2 and ADC, to investigate the potential capabilities of $T_{1\rho}$ and MRE in monitoring and evaluation of engineered cartilage growth. This study proposes to provide the first thorough evaluation of biochemical and mechanical properties of engineered cartilage tissue by using MR-derived imaging methodologies *in vitro*. Furthermore, to increase the efficiency of MR characterization of engineered tissues, the **second objective** of this study is to develop the new methodologies for simultaneous acquisition of MRI and MRE data, which allow the simultaneous characterization of both biochemical and mechanical properties of engineered cartilage tissues. Tissue engineers could use these combined MRI/MRE methods to monitor the current tissue growth and to test new culture methods in a more efficient way. If it becomes evident that tissue growth is not adequate, adjustments in culture conditions could be made without sacrificing the constructs. I expect that the combined MRI/MRE methods will benefit the optimal cartilage tissue engineering process. To that end, the following specific aims were proposed:

Aim 1: Use MRI to periodically monitor and assess the growth of engineered cartilage *in vitro*. To achieve this aim, we first developed high-resolution MRI-based methods to measure parameters such as, T_2, $T_{1\rho}$, and ADC on an 11.7 T micro-MR imaging system. The sensitivities of these MRI-based parameters to biochemical changes in tissue composition were validated in native bovine knee articular cartilage samples. Next, the validated T_2, $T_{1\rho}$ and ADC measurements were performed weekly on a scaffold-free engineered cartilage (chondrocyte pellets) *in vitro* for up to 3 weeks. The MRI results were then

correlated with the PG and collagen content determined by immunohistochemical (IHC) and biochemical assays.

Aim 2: Use MRE to periodically monitor and assess the growth of engineered cartilage *in vitro*. In this aim, we used a developed geometric focusing micro-MRE method to investigate the same type of engineered cartilage tissues developed in Aim 1. The sensitivity of MRE shear stiffness to the changes of mechanical behaviors of tissue were first tested in calcium-alginate beads. Then the validated MRE method was performed weekly to measure the shear stiffness of the chondrocyte pellets. The shear stiffness were also correlated with the PG and collagen content determined by IHC and biochemical assays.

Aim 3: To develop advanced MRI/MRE methods to allow simultaneous acquisition of MRI ($T_{1\rho}$ and ADC) and MRE parameters in phantom samples. In this aim, two advanced simultaneous MRI/MRE acquisition (dMRE and $T_{1\rho}$-MRE) were developed and validated by using tissue-mimicking phantoms. The dMRE method was developed to acquire MRE and diffusion data simultaneously. The $T_{1\rho}$-mre method was developed for concurrent $T_{1\rho}$ and MRE. The two new techniques were validated by using a tissue phantom composed of a gel bead embedded in a hydrated mixture of agarose and gelatin.

1.4 Dissertation Organization

The chapter-wise organization of this thesis is as follows:

Chapter 1 introduces the general background of articular cartilage tissue and tissue engineering treatments to cartilage injuries. It also describes the

motivations, the overall objectives for this project, and the specific aims to achieve the objectives. The following chapters (Chapters 4, 5, and 6) correspond to the three specific aims, respectively.

Chapter 2 introduces the theoretical foundations of magnetic resonance imaging involved in this study. The basic principles of tissue relaxometry and diffusion are described, and the corresponding acquisition schemes used in this study follow.

Chapter 3 describes the basis of magnetic resonance elastography. It starts with a detailed description of MRE system – vibration, motion encoding gradient, and inversion algorithm. At the end, a specific MRE setup, geometric focusing micro-MRE, is introduced.

Chapter 4 focuses on the MRI characterization of *in vitro* tissue-engineered cartilage. Bovine native articular cartilage plugs are first examined as a phantom to demonstrate the feasibilities of T_2, $T_{1\rho}$, and ADC characterization of PG and collagen, which present a natural distribution along the cartilage depth. Following a description of the preparation of engineered tissues, the high resolution MRI system and the methods used to measure the T_2, $T_{1\rho}$, and ADC parameters are then stated. Biochemical and IHC analyses used to biochemically analyze engineered tissues are presented and the correlations with the measured MRI parameters are discussed in this chapter.

Chapter 5 focuses on the MRE characterization of *in vitro* tissue-engineered cartilage. It starts with the alginate beads preparation for MRE

phantom validation. The geometric focusing micro-MRE method and the setup used to measure the shear stiffness of alginate beads and tissue-engineered cartilage are then described. Finally, the MRE results and the correlation with biochemical analyses are presented and discussed in this chapter.

Chapter 6 describes the two advanced methods of simultaneous acquisition of MRI and MRE: dMRE and $T_{1\rho}$-MRE. Theories of the simultaneous dMRE and $T_{1\rho}$-MRE methods are first explained, followed by the validation experiments of the proposed techniques on tissue-mimicking phantoms.

Chapter 7 provides a summary of the project, highlighting original contributions and limitations of the current study, and pointing to future research directions.

2 MAGNETIC RESONANCE IMAGING

Magnetic resonance imaging (MRI) is one of the most important developments in medical diagnosis since the discovery of X-rays. In contrast to X-rays, in which ionizing radiation penetrates tissue to reach a photographic plate behind the patient, MRI uses non-ionizing radio waves to induce a signal from paramagnetic nuclei within the tissue (29). Although there are many nuclei possess spins (e.g., ^{1}H, ^{13}C, ^{23}Na, ^{31}P) that can generate MRI signal, this dissertation focuses on the nucleus of hydrogen atoms (^{1}H proton) in water, because of its high sensitivity and abundance in the human body.

2.1 Theoretical Background of MRI

Magnetic resonance is based on the interactions between the spins and two magnetic fields: (1) static magnetic field B_0 to create a bulk magnetization $\mathbf{M_0}$, and (2) radiofrequency (RF) magnetic field B_1 to generate a measurable MR signal (30).

The nucleus of a hydrogen atom is a single positively charged proton. The magnetic moment $\boldsymbol{\mu}$ of the proton is directly proportional to the angular momentum $\mathbf{J}$,

$$\boldsymbol{\mu} = \gamma \mathbf{J} \qquad [2.1]$$

where γ is a constant called the gyromagnetic ratio (42.67 MHz/T for ^{1}H proton).

When a proton is placed in a strong external magnetic field B_0, it experiences a turning force, known as a torque that makes it precesses around

the direction of the field B_0 (***Figure 2.1***). The angular momentum of the spin changes according to the equation,

$$\left|\frac{d\mathbf{J}}{dt}\right| = \left|\boldsymbol{\mu} \times B_0\right| = \left|\gamma \mathbf{J} \times B_0\right| = \gamma J B_0 \sin\theta \qquad [2.2]$$

where θ is the angle between the magnetic moment and the magnetic field.

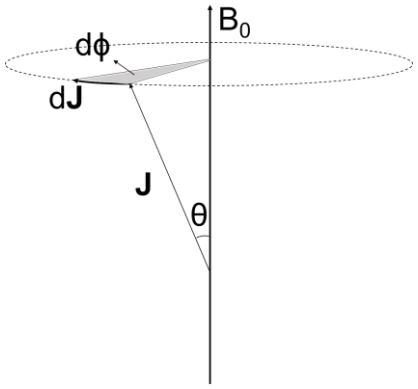

Figure 2.1. Precession of the magnetic moment **μ** around the main magnetic field B_0 (adapted from (30)).

It is easy to show that *dJ* is given by

$$dJ = J \sin\theta d\phi \,. \qquad [2.3]$$

Then from ***Eqs. 2.2*** and ***2.3***, we can derive that the precessional frequency is given by so called the ***Larmor equation***,

$$\omega_0 = \gamma B_0 \qquad [2.4]$$

where the precessional frequency of the proton is proportional to the external magnetic field. So the protons in this strong external magnetic field B_0 all precess at the same Larmor frequency ω_0, not any old frequency. This is known as a resonance condition.

According to the theory of quantum mechanics, when a large number of protons are placed in magnetic field B_0, not all nuclei orient in the direction of B_0. They experience two orientations, known as parallel and anti-parallel states (***Figure 2.2***). Since anti-parallel direction requires slightly more energy than the parallel direction, eventually, enough extra spins point up to make the net magnetization $\mathbf{M_0}$ pointing in the direction of B_0.

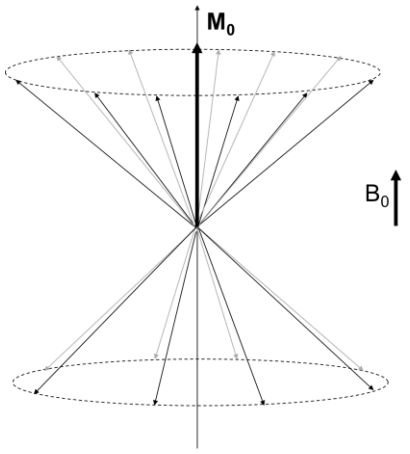

Figure 2.2. At thermal equilibrium, extra spins point up at main magnetic field B_0 creating a net magnetization $\mathbf{M}_0$ vector along B_0 direction (adapted from (31)).

In order to measure this bulk magnetization $\mathbf{M_0}$, it needs to be “flipped” into the transverse x-y plane to generate a readable signal by applying a RF pulse.

Consider a 3-dimentional (x, y, and z) coordinate system, the direction of $\mathbf{M_0}$ point in the z-direction (***Figure 2.3a***). If an RF pulse is transmitted along the x-axis, the protons that were previously aligned with the external magnetic field B_0 in the z direction will now also begin to precess about the x-axis – axis of the new RF magnetic field B_1. If the frequency ω_1 of RF pulse matches the Larmor frequency ω_0, then resonance occurs. Resonance results in the RF pulse adding energy to the protons. As energy is added by the RF pulse to flip the up-pointing protons to the higher energy state, the RF pulse causes the spins to begin precessing in phase with each other. The vector sum of these in-phase precessing protons lies in the transverse plane as if the net magnetization "flips" into x-y plane (***Figure 2.3b***). Having rotated M_0 into the transverse plane, it then can be measured by detecting the voltage induced in a RF receiver coil that is sensitive only to the magnetization perpendicular to B_0.

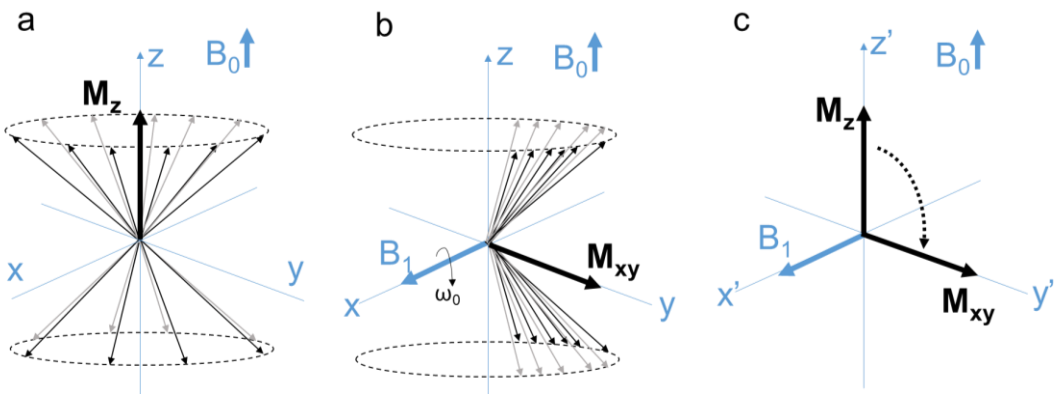

Figure 2.3. (a) A thermal equilibrium of magnetization at magnetic field B_0. (b) A RF B_1 filed along x-axis rotates the magnetization towards y-axis. (c) Excitation of magnetization in the rotating frame (adapted from (29)).

To simplify the concept of “flipping” of the spins, it is helpful to use a rotating frame of the reference, where the coordinate system is rotating at the Larmor frequency. Such a frame of reference makes the “flipping” as the slow precession of the protons from the z axis in to the x-y plane as if they were moving in a simple arc (***Figure 2.3c***). The rotating reference frame will be used as the basis for all future discussions in this thesis.

2.2 MRI Relaxation

2.2.1 The Bloch Equation and Basic Relaxation: T_1 and T_2

The application of RF pulses disturbs spins from their equilibrium states (low energy state). The term “relaxation” means that the excited spins are relaxing back into their lowest energy state. Having excited the protons to flip them into the transverse plane (higher energy state), they begin to relax back to their equilibrium position (lower energy state) as soon as the RF pulse is turned off. The protons will have to realign with the axis of the B_0 field and give up all their excess energy. This is reflected by two main features of the relaxation: T_1 relaxation and T_2 relaxation (30,31).

T_1 is called ***spin-lattice relaxation time*** because it refers to the time it takes for the spins to give back the energy they obtained from the RF pulse to the surrounding lattice in order to go back to their equilibrium state. This action rebuilds the longitudinal (z) magnetization $M_z(t)$ to its equilibrium value M_0 (***Figure 2.4***). The rate at which $M_z(t)$ recovers to M_0 at a rate characterized by T_1:

$$\frac{dM_Z(t)}{dt} = \frac{1}{T_1}(M_0 - M_Z(t)) \qquad [2.5]$$

T_1 is defined as the time taken for the longitudinal magnetization to reach 63% of the equilibrium value M_0.

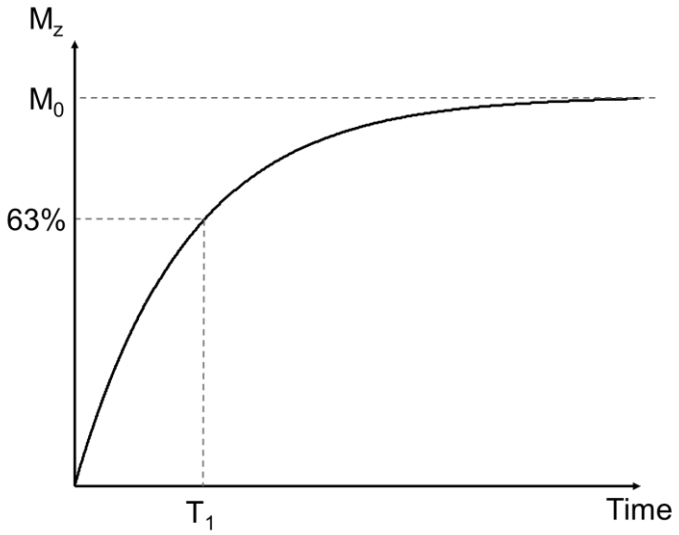

Figure 2.4. T_1 recovery of M_z to M_0 controlled by an exponential function.

As the longitudinal magnetization vector $M_z(t)$ recovers, the transverse vector $M_{xy}(t)$ decays at a rate characterized by T_2, named as ***spin-spin relaxation time*** (***Figure 2.5***):

$$\frac{dM_{xy}(t)}{dt} = \frac{M_{xy}(t)}{T_2} \qquad [2.6]$$

T_2 is defined as the time taken for the transverse magnetization to reach 37% of its initial value.

Unlike T_1 relaxation, where the loss of energy occurs in the spins during their interaction with the surrounding lattice (tissue), there is no net loss of energy in T_2 spin-spin relaxation. The decay of the transverse magnetization is due to the interactions between spins as they move around within the tissues. When two spins are next to each other, the magnetic field of one spin affects the spin next to it. The difference in the magnetic environment created by these proton interactions makes a difference in the overall homogeneity of the magnetic field to which the spins are exposed; spins are getting out of phase. The vector sum of the magnetic moments, which is the signal we detect in the MR receiver, gradually decays from a maximum down to zero.

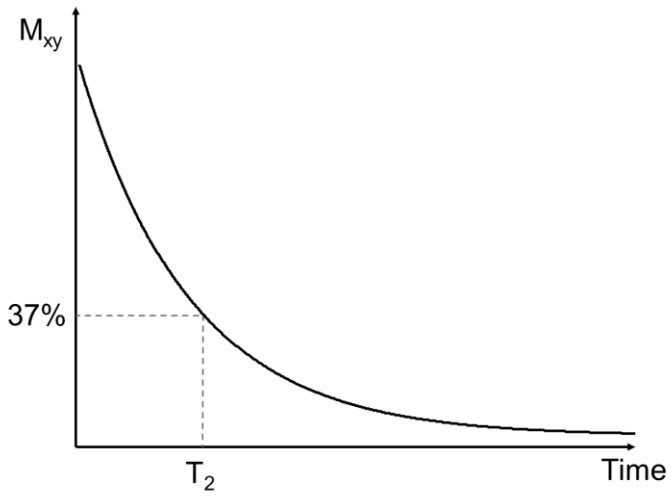

Figure 2.5. T_2 decay of M_{xy} to zero controlled by an exponential function.

The differential equations of two relaxation behavior of the spins ***Eqs. 2.5*** and ***2.6*** can be combined, and described by the ***Bloch Equation*** (30):

$$\frac{d\mathbf{M}}{dt} = \gamma\mathbf{M} \times \mathbf{B}_{ext} - \frac{(M_Z - M_0)}{T_1}\mathbf{k} - \frac{(M_x\mathbf{i} + M_y\mathbf{j})}{T_2} \qquad [2.7]$$

where B_{ext} is the applied magnetic fields that comprises the static B_0 field along the z-direction and the RF B_1 field in the x-direction. If the system was initially in equilibrium and the RF pulse was a 90° pulse applied along the +x-axis, the solution to the Bloch equation is given by:

$$M_Z(t) = M_0[1 - \exp(\frac{-t}{T_1})] \qquad [2.8]$$

$$M_{xy}(t) = M_0[\exp(\frac{-t}{T_2})] \qquad [2.9]$$

The T_1 relaxation time, ranges from hundreds to thousands of milliseconds for protons in tissue, and increases with increasing field strength B_0. The T_2 relaxation time is in the order of tens of milliseconds for protons in most tissues, and is much shorter than T_1 for the same tissue (***Figure 2.6***). In addition, for most of tissues, T_2 values are much shorter for solids than liquids. The time difference between T_1 and T_2 in different tissues are the basics of MR contrast, and the underlying principle is known as the ***BPP theory of relaxation***.

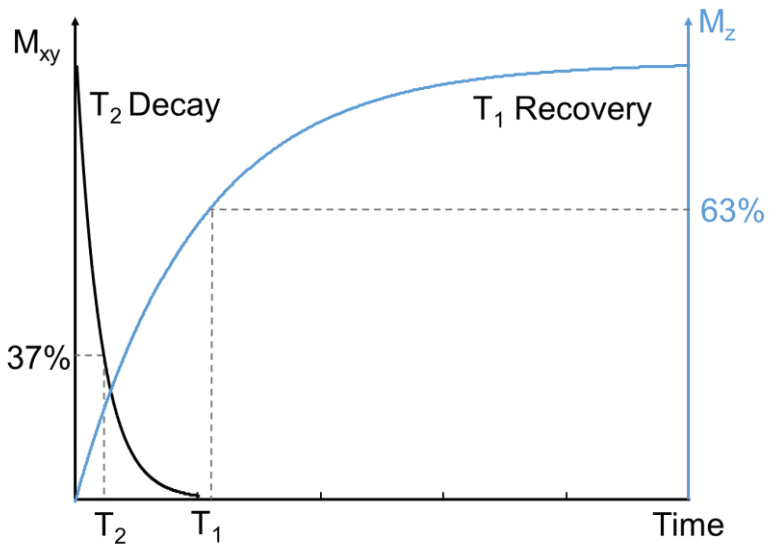

Figure 2.6. T_1 and T_2 relaxation occur simultaneous, but T_2 is much shorter than T_1.

The term “lattice” is an oversimplification of a complex entity, including every atom and molecule that may interact with the spin. Every atom or molecule is rotating, vibrating and translating at different frequencies and in random directions. Not only that, molecules change their motion rapidly as they collide with each other, so they will be vibrating at this moment and translating the next. Actually, a molecule spends only a tiny fraction of a second in a particular state of motion, as little as 10^{-12} s, before suffering a collision to change to something different. This is known as the correlation time τ_c of the molecule. The BPP theory (23,31,32) describes the T_1 and T_2 relaxation rates (inversely relaxation time) in terms of the correlation time τ_c of the molecule and the Larmor frequency ω_0:

$$\frac{1}{T_1} = K[\frac{\tau_c}{1+\omega_0^2\tau_c^2} + \frac{4\tau_c}{1+4\omega_0^2\tau_c^2}] \qquad [2.10]$$

$$\frac{1}{T_2} = \frac{K}{2}[3\tau_c + \frac{5\tau_c}{1+\omega_0^2\tau_c^2} + \frac{2\tau_c}{1+4\omega_0^2\tau_c^2}] \quad [2.11]$$

where K is a constant that depends on nuclear parameters.

In pure water, the water molecules are in free state (free water) and move quicker, leading to a shorter τ_c compared to water molecules in biological tissues, where water molecules (bound water) are bound to large hydrophilic macromolecules such as polysaccharides and proteins. There is also a third state of water molecules considering as structured water, where a proton is in the intermediate situation between bound and free (33). In biological tissues, there is believed to be a continuum of 'binding' from the tightly bound protons close to the surface to the 'free' protons furthest away from large molecules, so there is a range of motional frequencies ω, statistically described by the ***spectral density function*** J(ω), given by

$$J(\omega) \propto \frac{\tau_c}{1+\omega^2\tau^2} \quad [2.12]$$

This simply shows the number of nuclei that tumble in a range of frequencies for a given lattice (***Figure 2.7***) (31).

The T_1 of a tissue is relate to the efficiency of energy transfer from the spin system to the surrounding lattice. The most efficient energy transfer occurs when the natural motional frequency (rotation, vibration, and translation) of protons are at the Larmor frequency. Recall that the Larmor frequency ω_0 is proportional to the strength of the magnetic field (***Eq. 2.4***), in most of MRI scanners, it is in the range of tens to hundreds MHz. So if the lattice contains a large number of motions

tumbling near this frequency range (as structured water in ***Figure 2.7***), the energy transfer is efficient, and the spins relax back to their lower energy state quickly. The net result is a shortening in T_1.

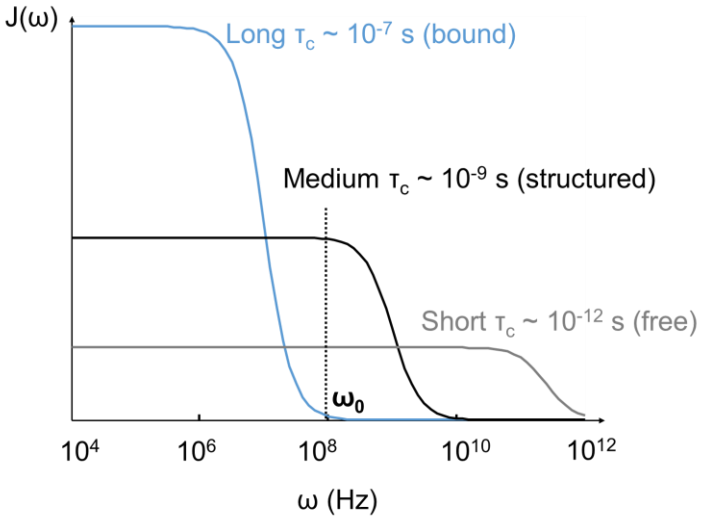

Figure 2.7. Dependence of the relationship between spectral density function J(ω), and frequency ω, on correlation time τ_c (adapted from (31)).

The T_2 relaxation arises from the exchange of energy between spins – a different mechanism from T_1. The decay rate is determined by the rate of loss phase coherence in spin system from intrinsic magnetic field inhomogeneities. When molecules are tumbling slowly (e.g., bound protons with long τ_c), a particular proton will "sense" the local magnetic field from its neighbors that changes more efficiently over a few milliseconds and will be more dephased. Conversely, a rapidly tumbling molecule (e.g., free protons with short τ_c) will see a relatively homogeneous local field due to motional averaging and will be less dephased with

respect to bound protons, resulting in a long T_2. So we can predict that with the increasing size and mass of macromolecules in biological tissues, there will be more bound or structured water formed. Hence, the T_2 values of such tissues are short due to increased dephasing effect.

2.2.2 From T_1 and T_2 Relaxation to $T_{1\rho}$ Relaxation

The basic T_1 and T_2 relaxation arise from the complex interactions between protons and macromolecules in their surrounding environment. The T_1 relaxation is sensitive to the molecular motions at the Larmor resonance frequency, whereas T_2 reflects slow molecular motions associated with the large macromolecules. So T_2 relaxation is considered to be more suitable for tissue characterization because most molecular motions in biological tissues are in slow interaction category. On the other hand, since T_1 relaxation is more efficient at Larmor frequency, it can be expect that T_1 would also be tissue-specific at low B_0 field. However, MR imaging at Larmor frequency below 0.1 MHz is impractical due to poor signal-to-noise ratio at low B_0 magnetic field. This is where $T_{1\rho}$ developed.

$T_{1\rho}$ is called the ***spin-lattice relaxation time in the rotating frame*** that was first introduced in 1955 (34). $T_{1\rho}$ enables the measurement of low frequency molecular motional processes at high MRI field strengths. This is done by applying a low-amplitude spin-locking (SL) pulse (35). The SL pulse creates a small new magnetic field B_1 that is oriented in the transverse plane, parallel to the bulk magnetization after flipped to transverse plane (***Figure 2.8a***). If there were no SL pulse, the magnetization would decay due to T_2 relaxation. The presence of this

SL field alters the tendency of the spins to precess at Larmor frequency, and "forces" spins precess at this new B_1 field - B_{SL} (***Figure 2.8b***).

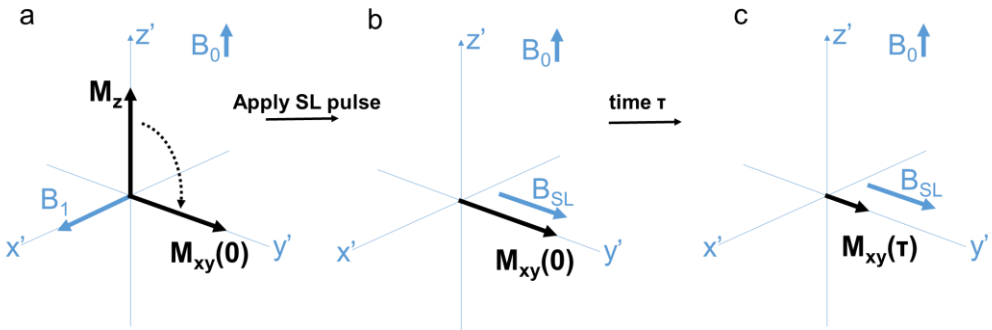

Figure 2.8. Application of a spin-locking pulse to induce $T_{1\rho}$ relaxation. (a) The longitudinal magnetization is flipped into x-y plane. (b) A spin-locking (SL) pulse is applied along the transverse magnetization. (c) The pulse is on for duration τ, resulting that the magnetization decays under the influence of the SL pulse.

While the SL pulse on for a period of time τ, the lower energy state is now determined by B_1 field. The large magnetization vector that was initially polarized in B_0 will decay to reach the new equilibrium value caused by much smaller B_1 field, along the SL pulse direction with the time constant $T_{1\rho}$ (***Figure 2.8c***). The intensity of the measured magnetization is given by,

$$M(t) = M_0[\exp(\frac{-\tau}{T_{1\rho}})]. \qquad [2.13]$$

where τ is the duration of SL pulse.

The SL pulse creates a new environment that affects the spins' interactions with the lattice. The most efficient relaxation between the spins and the lattices

now occurs at the “new” Larmor frequency ω_1, i.e., the SL frequency determined by the low-amplitude SL field B_1. Typically, ω_1 is much slower than ω_0. For example, the Larmor frequencies of water protons for current MRI scanners (1.5 T – 11.7 T) are in the range of 64 MHz to 500 MHz, whereas the SL frequencies used in most research and clinical work are in the range of 100 to 1000 Hz (36). Since there are far more spin-lattice interactions operating at these low frequencies than at high frequencies, the $T_{1\rho}$ relaxation is thus more sensitive to the slower molecular motions than T_1. The amplitude and duration of SL pulse can be set to arbitrary values, which indicates the $T_{1\rho}$ relaxation is dependent on the SL pulses applied. The dependence of $T_{1\rho}$ on the SL pulse field is called $T_{1\rho}$ dispersion (23). $T_{1\rho}$ dispersion is quantified by measuring $T_{1\rho}$ with a range of SL pulse amplitudes.

Similar to BPP equations of T_1 and T_2, $T_{1\rho}$ relaxation rate obeys the following equation (23):

$$\frac{1}{T_{1\rho}} = K[\frac{3}{2}\frac{\tau_c}{1+4\omega_1^2\tau_c^2} + \frac{5}{2}\frac{\tau_c}{1+\omega_0^2\tau_c^2} + \frac{\tau_c}{1+4\omega_0^2\tau_c^2}] \qquad [2.14]$$

where τ_c is the correlation time, and ω_0 and ω_1 are the frequencies corresponding to main magnetic field and SL pulse, respectively. From ***Eqs. 2.10, 2.11*** and ***2.14***, it can be seen that $T_{1\rho}$ is related to T_1 and T_2 as follows: (1) as the SL frequency ω_1 approaches zero, $T_{1\rho}$ approaches T_2; (2) as ω_1 approaches ω_0, $T_{1\rho}$ approaches T_1; (3) for most of biological tissues, $T_1 > T_{1\rho} > T_2$.

2.2.3 Pulse Sequences for Relaxation Time Measurements

In MRI, a pulsed RF field is applied to generate an MR signal that contains information about the entire tissue being imaged. In order to form an MR image, an additional, spatially varying magnetic field, called gradient field is necessary to localize the MR signal. One gradient is required in each of the x, y and z directions. Depending on their function, these gradients are called slice-selection gradient (G_{ss}), frequency-encoding gradient (G_{fe}), and phase-encoding gradient (G_{pe}), respectively. To obtain a readable MR image, the RF pulses and gradients are applied in a controlled fashion to form an MR pulse sequence (30,37). Here, taking a commonly used pulse sequence, spin-echo (SE) imaging pulse sequence as an example to show how it manages to localize the MR signal (***Figure 2.9***).

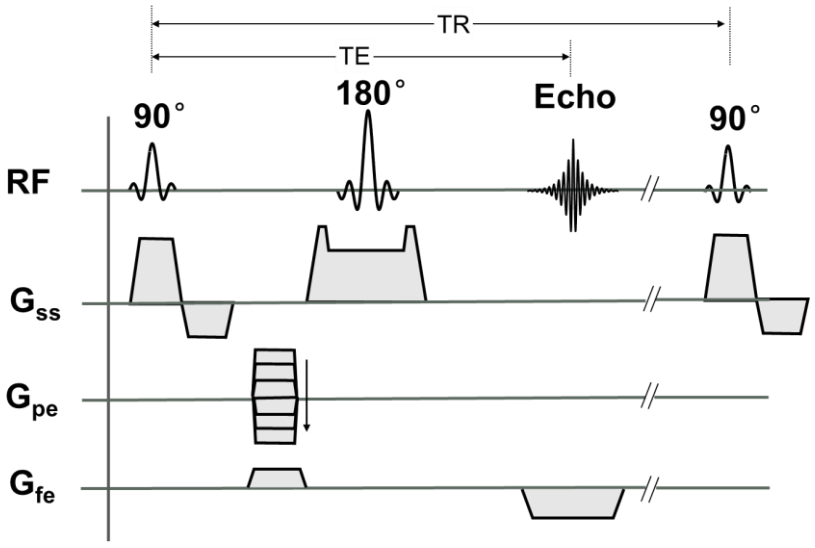

Figure 2.9. Diagram of spin-echo (SE) pulse sequence.

Briefly, slice selective 90° and 180° RF pulses are applied simultaneously with a slice-selective gradient G_{ss} to excite a two-dimensional slice. By choosing the RF pulse with an appropriate frequency and bandwidth, one can select a slice at a particular position with a particular thickness. The 90° and 180° pulses are separated by a time of τ. After a time of 2τ after the 90° RF pulse, an echo signal from the whole slice will be formed. This 2τ time is referred to as echo time (TE). Next, before the echo is received, a phase-encoding gradient G_{pe} is applied in a direction orthogonal to the slice selection. The frequency-encoding gradient G_{fe} is turned on in the third direction during the time period during which the echo is received. The in-plane MR signal is now encoded in terms of the different spatial frequencies depending on the different location within the excited slice. The whole sequence pattern has to be repeated to collect every spatial frequency that exists within the slice, corresponding to a different value of G_{pe} at each cycle. The time interval between the application of one 90° pulse and the next is called repetition time (TR). Once all the data are acquired a two-dimensional Fourier transform is applied to convert the acquired data into an image. The T_2 and $T_{1\rho}$ relaxation times can then be measured based on such a SE pulse sequence.

For T_2 measurement, one could simply apply a series of SE sequences with varying TE, and measure the signal at each TE. T_2 relaxation time can therefore be determined by solving ***Eq. 2.9*** as a function of variable TE values. Rather than repeating an experiment with a different echo time to measure T_2, it is common to collect data for more than one echo of the original RF excitation being much more time-efficient. This is accomplished by applying multiple 180° pulses after a single

90° pulse. This is known as Carr-Purcell T_2 measurement (38). A further improvement known as Carr-Purcell-Meiboom-Gill (CPMG) sequence was made to compensate for imperfections in the 180° pulses that would lead to accumulated errors in the determination of T_2 (39). In CPMG (***Figure 2.10***), the initial 90° pulse is on the +x axis and the train of 180° pulses are on the +y axis. If the 180° pulse is imperfect, the first and every odd-numbered echoes will be smaller, but even echoes will be the correct. The even-numbered echoes can then be used to determine T_2 without accumulated errors from imperfection of 180° pulses.

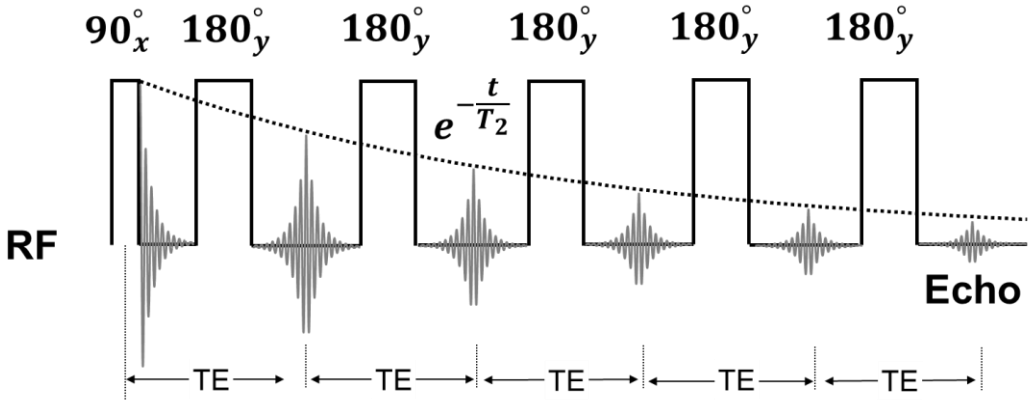

Figure 2.10. Echo train of CPMG Sequence (adapted from (40)).

To measure $T_{1\rho}$ relaxation time, one must allow the spins to relax in the presence of a SL pulse at some point in time during the sequence. This is done by applying a SL preparatory pulse in front of any imaging sequence (35). As shown in ***Figure 2.11***, after applying a 90° RF hard pulse along the +x direction, the net magnetization will flip into the transverse plane along the y-axis. Then immediately

applying a long, low powered SL pulse parallel to the magnetization (y-axis), the net magnetization will be locked in the y direction and start to decay at a rate of $T_{1\rho}$. The last 90° pulse is applied at -x direction to re-store this $T_{1\rho}$ prepared magnetization to z-axis for imaging. A crusher gradient is applied right after the last 90° pulse to dephase any residual transverse magnetization. According to ***Eq. 2.13***, the $T_{1\rho}$ relaxation can be measured by analyzing the intensity of MR signal collected as a function of the duration of the SL pulse, called TSL.

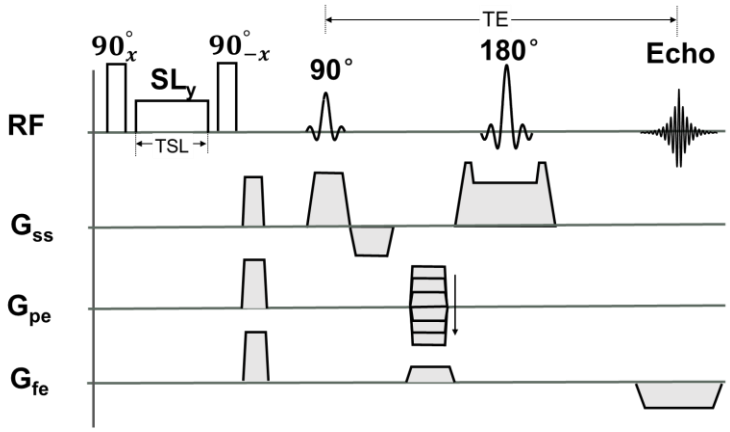

Figure 2.11. Three $T_{1\rho}$ preparatory pulses in front of a SE pulse sequence. The first hard pulse flips the magnetization into the transverse plane. The following SL pulse applied with amplitude B_{SL} and duration T_{SL} allows the $T_{1\rho}$ relaxation occur. The third hard pulse restores the $T_{1\rho}$ prepared magnetization into longitudinal axis.

However, when the 90° pulse cannot perfectly flip the magnetization into the transverse plane, this will cause an artifact in the final image. To correct this artifact, a self-compensation preparatory pulse was developed (41). The second

half the SL pulse is phase-shifted by 90° with respect to the first half (***Figure 2.12***). This design helps to correct the imperfect rotations from imperfection of 90° pulse.

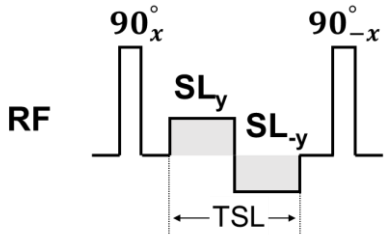

Figure 2.12. $T_{1\rho}$ preparatory pulse cluster with self-compensation. The second half of the SL pulse is phase-shifted 90° with respect to the first hard SL pulse (adapted from (41)).

2.3 Diffusion MRI

2.3.1 From Classical Diffusion to Molecular Self-diffusion

The classical description of diffusion is a mass transport process that takes place without bulk fluid motion in the presence of concentration gradient. It goes from regions of higher concentration to regions of lower concentration. The physical law behind this phenomenon is called Fick's first law (42),

$$\mathbf{J} = -D\nabla C \qquad [2.15]$$

where the net diffusion flux **J** is proportional to the concentration gradients ∇C as well as to the diffusion coefficient D. However, this macroscopic description of diffusion focuses on the evolution of the concentration gradient over time and space, and is not concerned with the movements of molecules themselves.

On a molecular level, the diffusion also occurs when there is no concentration gradient, referred to as ***molecular self-diffusion***. The first observation of such phenomenon was by *Robert Brown* in 1827, who noted that the particles moved randomly through the water without apparent cause while looking through a microscope at pollen grains in water (43). In 1905, it was *Albert Einstein* that explained in precise details about how the motion that *Brown* had observed was a result of the pollen grains being moved by individual water molecules (44). Einstein used a probabilistic concept – displacement distribution – to describe the motion of an ensemble of diffusive molecules. He proved that the mean squared displacement $\langle r^2 \rangle$ of molecules from their starting point over a time t, averaged over all the molecules in the sample, is directly proportional to the observation time t. This relationship is given in the form of ***Einstein's Equation***:

$$\left\langle r^2 \right\rangle = 6Dt \qquad [2.16]$$

where proportional constant D is the same as classical diffusion coefficient defined in Fick's first law (***Eq. 2.15***). In free diffusion, the displacement distribution is a Gaussian function whose width is determined by the diffusion coefficient. Larger diffusion coefficients lead to broader displacement probabilities suggesting increased diffusional mobility.

2.3.2 Hindered Diffusion and Apparent Diffusion Coefficient

Einstein's equation (***Eq. 2.16***) tells us that the mean squared displacement is directly proportional to observation time. In the case of free diffusion – a cube of free water at 37°C – from classical diffusion experiment, the diffusion coefficient of

water is 3×10^{-3} mm^2/s. Therefore, if the observation time were 25 ms, the water molecules would have displaced, on average, 21 μm in all directions. However, in biological tissues, the water molecules may encounter some hindrances while moving, such as cell membranes, macromolecules, organelles, fibers, or other cellular structures (45). Then the mean squared displacement per unit time will be lower than what observed in free water. Thus, when we apply ***Eq. 2.16*** to compute the diffusion coefficient of this hindered diffusion, it will "appear" that the diffusion coefficient is lower, though the theoretically value of diffusion coefficient of water molecules is equal to 3×10^{-3} mm^2/s. Diffusion MRI does not measure diffusion coefficient directly. It infers the ***apparent diffusion coefficient (ADC)*** from observations of the displacements over a given time period. So clearly, the geometric structure of the tissue environment would influence the diffusional processes of water molecules, and thus being detected by diffusion MRI.

2.3.3 Pulse Sequence for Diffusion Measurement

MR provides a way to measure the diffusion displacement by using a pair of magnetic field gradients (45), i.e., a magnetic field is made to vary in a linear manner over the volume of interest. Almost any MRI pulse sequence can be modified to become sensitive to diffusion. Here, the pulsed gradient spin-echo (PGSE) diffusion sequence is explained as an example.

The concept of PGSE diffusion weighting was introduced by *Stejskal and Tanner* in 1965 (46) by the application of a pair of bipolar magnetic field gradients after excitation and before signal acquisition (***Figure 2.13***). After excitation, spins are in-phase. With the application of the first diffusion gradient lobe, the spins at

different locations experience the different magnetic fields. Because a spin's precession frequency is determined by the local magnetic field as shown in ***Eq. 2.4***, the gradient imposes a position-dependent precessional frequency across the sample. After a certain time δ, the spins acquire different phase shifts depending on their locations. When the first gradient is turned off, all spins precess again at the same frequency, but retain their relative phases. There is a gradient in phase accrual over the volume.

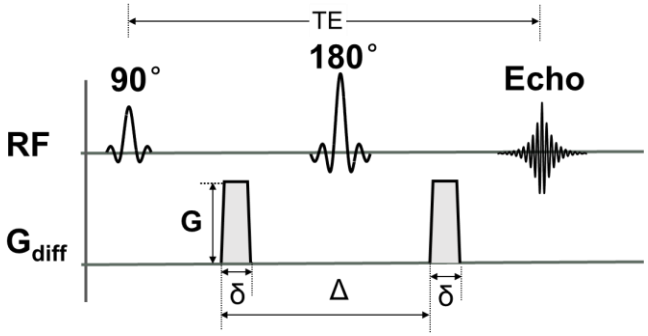

Figure 2.13. Schematic diagram of pulsed field gradient spin-echo (PGSE) pulse sequence. A pair of diffusion-weighting gradients are placed at two sides of 180° pulse with gradient duration, δ, and separation time, Δ.

Clearly, if the spins remain stationary before the application of the second gradient, this phase accrual can be reversed by the second gradient with the same gradient amplitude, duration, and polarity followed after the 180° pulse. The resulting magnitude of the echo will be unchanged. However, if spins diffuse randomly throughout the excited volume over the time period Δ, a particular spin will see a change of local magnetic field over time due to the random movements

of its neighbors. This results in a net phase change. Then the second gradient can only reverse the phase change induced by the first gradient, but it cannot remove the diffusion-induced net phase change. This incomplete cancellation results in phase dispersion of spins across the volume. Therefore, the sum vector of the magnetic moments of all spins is reduced. The greater the rate of the diffusion, the greater the spread of displacement (i.e., phase dispersion), and thus the greater the loss of signal.

Under the assumption of free diffusion, the measured MR signal is attenuated exponentially by the product of diffusion coefficient D and a factor b, given by

$$S = S_0 \exp(-bD) \qquad [2.17]$$

where S and S_0 are the signal intensities acquired with and without the diffusion gradient, respectively. The image contained with the diffusion information S is called ***diffusion-weighted image (DWI)***. The b-value is a factor of diffusion sequence, which is used to characterize the influence of the gradients on the diffusion. Its values is dependent on the applied gradient strength G, duration δ, and separation Δ. The generalized equation for b is:

$$b = \gamma^2 \int_0^{TE} \left[\left(\int_0^t G(t')dt' \right)^2 \right] dt \qquad [2.18]$$

For the PGSE experiment, the b-factor is given by:

$$b = \gamma^2 G^2 \delta^2 (\Delta - \frac{\delta}{3}) \qquad [2.19]$$

The ADC can be calculated by collecting a set of data acquired with two or more b-values.

It should be noted that the calculated ADC only reflects diffusion along the direction of the diffusion-weighting gradients. DWI or associated ADC values highlight the differences in water molecule mobility along this particular direction. There are certain structured tissues such as nerve fibers with organization in bundles of axons running in parallel that can create obstacles to orientate the motion of water molecules. Water molecules have tendency to displace themselves in one or several particular direction. ***Diffusion Tensor imaging (DTI)***, on the other hand, studies the directions of water molecule motions by performing diffusion-weighted acquisitions in at least six directions (47). The acquired images are used to characterize the anisotropic diffusion coefficient, fractional anisotropy (FA), preferred directions, etc. In addition to the mono-exponential model given by ***Eq. 2.17***, there are a variety of other diffusion models proposed to analyze the diffusion data, e.g., bi-exponential (48), stretched exponential (49), fractional-order calculus-based (50), and Kurtosis models (51).

3 MAGNETIC RESONANCE ELASTOGRAPHY

Magnetic resonance elastography (MRE) is an emerging imaging modality that maps the elastic properties of tissue such as the shear modulus on to MR images (25,52). Like other elasticity imaging modalities, it follows the general steps of elastography: (1) apply a known cyclic shear stress to the tissue; (2) measure the internal tissue displacements using magnetic resonance method; and (3) infer the mechanical properties from the measured mechanical response (displacement), using either a simplified or continuum mechanical model. The acquired image is an elastogram. In this chapter, the three steps of MRE are described in details.

3.1 Generate Propagating Shear Waves in Tissue

The mechanical vibrations applied to tissue fall into three categories: a transient, quasi-static, or harmonic. MRE typically uses harmonic vibrations generated by an external driver device to perturb the tissue. In harmonic excitation, a low-frequency acoustic wave (20 Hz to several kHz) is transmitted within the tissue using a sinusoidal mechanical source, for example, a functional generator. When the shear stresses (amplitude of microns) are applied to the top surface of a material with certain frequency, the induced waves are propagating into the tissue and every point in the tissue reciprocates in this micromotion (***Figure 3.1***).

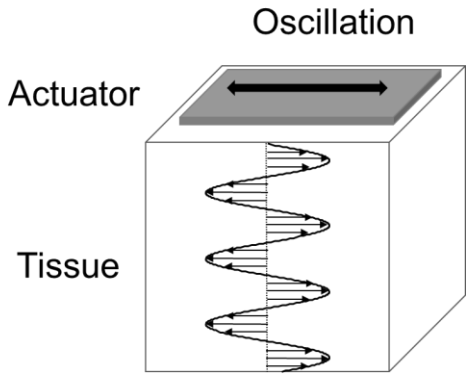

Figure 3.1. An actuator is coupled to the tissue of interest to generate propagating shear waves within a soft material.

The tissue response to the applied harmonic excitation is represented in terms of waves propagating within the tissue. Two types of plane wave, shear wave and compression wave propagate independently in the bulk material. Under the assumption of homogenous, isotropic, and linearly elastic, the dynamic response of such material is governed by the wave equation given by (53)

$$-\rho \frac{\partial^2 \mathbf{u}}{\partial t^2} = \nabla \cdot \mu \nabla \mathbf{u} + \nabla(\lambda + \mu)\nabla \cdot \mathbf{u} \qquad [3.1]$$

where ρ is the density of the material, **u** is the displacement vector, λ and μ are Lamé constants.

3.2 Pulse Sequence for MRE Motion Encoding

After the mechanical excitation, a phase-contrast based pulse sequence is used to encode the shear wave motion into the MR phase signal by using a series of magnetic field gradients called motion-sensitizing gradients (MSG) or motion-encoding gradients (MEG). The MSG is typically applied after RF excitation pulses

and before signal acquisition. An example of SE based MRE pulse sequence is shown in ***Figure 3.2***. The encoding is obtained through the application of MSGs that are synchronized with the mechanical excitations (25,52).

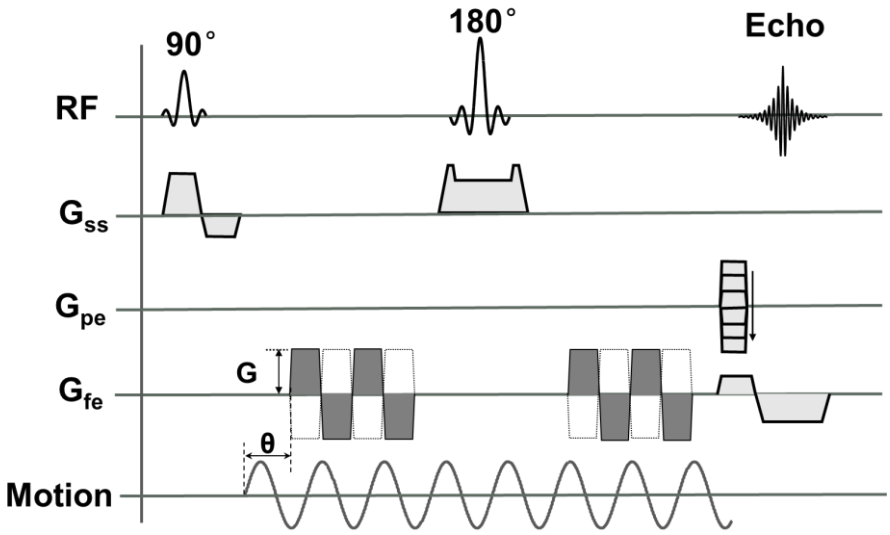

Figure 3.2. Schematic diagram of SE-based MRE pulse sequence. The MSG is shown as oscillating gradients (solid line) at G_{fe} direction. The MSG is synchronized with mechanical motion to encode this wave motion into the MR signal. The phase difference θ between the MSG and vibrational motion is adjustable. Negative MSG (dotted line) is used to create phase difference images.

As discussed before, in the presence of a magnetic field gradient G, at a particular time t', an ensemble of spins (also called ***isochromat***) situated at position x experiences a magnetic field of $B_0 + G_x(t')$. If the spin isochromat moves from one position to another as a function of time t, then after a certain time τ, the isochromat will accrue a phase shift given by:

$$\phi(\tau) = \gamma \int_0^{\tau} \mathbf{G}_r(t) \cdot \mathbf{r}(t) dt \qquad [3.2]$$

where γ is the gyromagnetic ratio characteristic of the nuclei, $\mathbf{G}_r(t)$ is the time-dependent magnetic gradient vector, $\mathbf{r}(t)$ is the time-dependent displacement vector, and τ is the duration of the gradient.

Considering an arbitrary point (isochromat) in an elastic sample oscillating in up and down directions (***Figure 3.3***), the MSG is applied along the same direction.

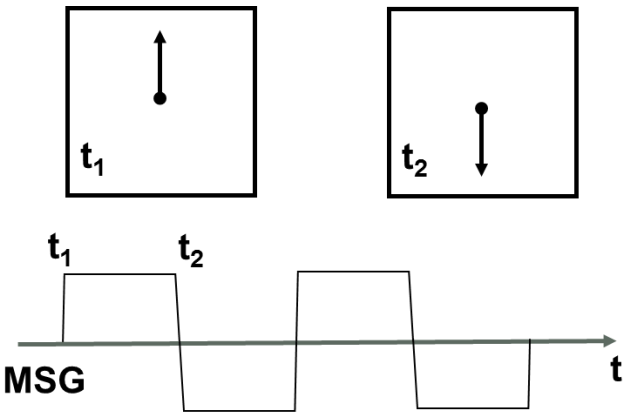

Figure 3.3. MSG and the local oscillation.

When the isochromat starts moving up at time t_1, the gradient is set to at the positive value. In this moment, small phase shift occurs until time t_2 by the motion towards up. Next, the isochromat moves downwards. In this moment, the polarity of the MSG is switched to the negative direction, thus the resulting polarity of the phase shift derived from the negative MSG and the motion of negative

direction becomes the same as previous one. With the several repetition of such cycles, an accumulated phase shift is occurred.

In MRE, the displacement vector of tissue produced by harmonic vibration can be assumed as a pure sinusoid given by

$$\mathbf{r}(t) = \mathbf{r}_0 + \xi_0 \exp(\, j(\mathbf{k}\cdot\mathbf{r} - \omega t + \theta)) \qquad [3.3]$$

where $\mathbf{r}_0$ is the mean position of the isochromat, $\mathbf{k}$ is the wave number, ξ_0 is the peak displacement of the isochromat from its mean position $\mathbf{r}_0$, ω is the angular frequency of the external vibration, and θ is the initial phase offset.

In the following we consider the MSG as an ideal rectangular gradient waveform that turns on for a duration τ (τ = NT, N is the number of MSG cycles). The MSG is switched in polarity as the same frequency f as the mechanical harmonic vibration described by

$$\mathbf{G}_r(t) = \begin{cases} +|G|; t \in [nT, (2n+1)T/2] \\ -|G|; t \in [(2n+1)T/2, (n+1)T] \end{cases} \qquad [3.4]$$

where n = 0,1,2, …N-1, T = 1/f = 2πω, and G is the gradient amplitude. Then by substituting ***Eqs. 3.3-3.4*** into ***Eq. 3.2***, the accumulated phase of the moving isochromat can be written as

$$\phi(\tau) = \frac{2\gamma NT(\mathbf{G}\cdot\xi_0)}{\pi}\sin(\mathbf{k}\cdot\mathbf{r} + \theta) \qquad [3.5].$$

This phase information is obtained in the phase component of the complex MR signal, and the value depends on the duration of the MSG, the strength of the MSG, and the phase difference between the mechanical motion and MSG. If the gradient

is applied along the direction of the external vibration, the ***Eq. 3.5*** can be rewritten as

$$\phi(\tau) = \left(\frac{2\gamma NTG}{\pi}\right)\ \xi_0 \sin(\mathbf{k}\cdot\mathbf{r} + \theta) \qquad [3.6].$$

It shows that the measured phase is proportional to the displacement vector, and the proportional constant 2γNTG/π is called the MRE encoding efficiency. It is the synchrony of the cyclic gradient with the micromotion that causes the high sensitivity of MRE to the small cyclic displacements (~microns) associated with wave propagation. In the phase image, the signal of each pixel represents the direction and amount of displacement vector. The phase image that contains the information of the propagating wave is thus called wave image.

In real MRE measurement, a phase difference image is typically used by phase subtraction or complex division of two phase images acquired from two MRE scans with reversed polarity of MSG (as dotted line in ***Figure 3.2***). In doing so, (1) the phase errors due to the static magnetic field from other imaging gradients are removed, and (2) the motion efficiency is doubled in the subtraction.

The ***Eq. 3.5*** also shows that the phase accumulation is dependent on the initial phase offset θ between the mechanical motion and MSG. The measured phase signal at particular phase offset θ thus only provides a snapshot of the tissue displacement caused by propagating mechanical waves through its encoding. By adjusting the phase offset θ, shear wave images at different time offsets spaced equally over a cycle can be acquired. This enables (1) displaying wave propagation over time; (2)reconstruction of complex valued shear wave propagation images;

and (3) extraction of the harmonic component at the frequency of interest, which is critical for advanced multi-frequency or multi-direction MRE encoding schemes (54,55).

3.3 MRE Mechanical Parameter Reconstruction

From the acquired wave images, inverse reconstruction algorithms based on wave equation (***Eq. 3.1***) can be used to convert the displacement data to mechanical properties (53,56). The mechanical quantity that MRE characterizes typically is shear modulus (μ), which describes the proportionality relationship between the shear stress and strain. Since the MRE excitation is primarily shear and the displacements in MRE are very small (~ microns), it can be assumed that there is no volume change as layers of material move in shear, perpendicular to the direction of the wave propagation, i.e., $\nabla \cdot \mathbf{u} = 0$. The wave equation ***Eq. 3.1*** can be simplified as

$$-\rho \frac{\partial^2 \mathbf{u}}{\partial t^2} = \nabla \cdot \mu \nabla \mathbf{u} \qquad [3.7]$$

For harmonic displacement, the time-independent ***Eq. 3.7*** in the frequency domain can be further written as

$$-\rho \omega^2 \mathbf{u} = \mu \nabla^2 \mathbf{u} \qquad [3.8]$$

where ω is the angular frequency of the mechanical motion. If the Voigt model is used to extract the mechanical properties, the shear modulus μ can be written as $\mu = \mu_r + j\omega\mu_i$. Here, μ_r and μ_i denote shear elasticity and shear viscosity. The shear modulus then can be calculated from the direct inversion of wave equation ***Eq. 3.8***

(57). If assuming solely single motion direction, the shear modulus can be estimated given by (Helmholtz inversion),

$$\mu = \frac{-\rho\omega^2\mathbf{u}}{\nabla^2\mathbf{u}} \quad [3.9]$$

Assuming that shear waves propagate with plane wavefronts, the shear wave speed c_s is related to the complex shear modulus μ* as follow:

$$c_s = \frac{1}{\Re\left(\sqrt{\frac{\rho}{\mu^*}}\right)} \quad [3.10]$$

In the assumption of an isotropic, homogeneous medium, the wave speed itself can be reported as the effective shear stiffness (58), defined as

$$\mu_s = \rho c_s^2 = \rho(\lambda_s f)^2 \quad [3.11]$$

which represents the shear modulus of an elastic material that exhibits the observed wave speed. Here, λ_s is the wavelength ($\lambda_s = c_s/f$) of propagating waves. In tissue exhibiting only a modest amount of attenuation (e.g., $\mu_i < 0.1\mu_r$), shear stiffness is an approximation of the real part or magnitude of the complex shear modulus. For example, for 0.75% w/v agarose gel, the value of shear stiffness μ_s (~ 9.15 kPa) is close to the magnitude of the shear modulus |μ*| (~ 8.99 kPa) at a driving frequency of 550 Hz (59). The shear stiffness μ_s can be calculated if the wavelength λ_s is measured, as the frequency is known and the density of most soft tissues is close to the density of water (1000 kg/m^3). A variety of approaches have been used to estimate the localized wavelength, such as LFE (local frequency estimation (60)) and PG (phase gradient (58)).

3.4 From MRE to Geometric Focusing Microscopic MRE

The image of the mechanical properties of tissue determined from MRE is referred as elastogram. The resolution of elastogram is dependent on the imaging resolution that is determined by the MR system itself. For example, the typical voxel resolution of clinical MRE performed at 1.5 T or 3 T magnetic field is 1 mm × 1 mm × 10 mm, which is sufficient to image shear waves in large tissues or internal organs, such as brain, liver, and muscle. However, if the size of tissue of interest is in the order of millimeters (e.g., tissue-engineered cartilage), it requires a higher imaging spatial resolution to extend MRE to the submillimeter scale. This can be done by employing an MRI system with a higher magnetic field (11.7 T versus 1.5 T) to obtain a better signal-to-noise ratio, so called microscopic MRE (micro-MRE or μMRE) (59). To obtain a higher spatial resolution, micro-MRE also uses stronger MR imaging gradients (200 G/cm versus 5 G/cm) and more compact mechanical actuators to generate higher excitation frequencies than those used in the clinic.

In addition to high spatial resolution, for stiffness determination of small and stiff tissues, MRE needs to be performed at excitation frequencies in the kHz range. This is because the spatial wavelength decrease with the increase of external mechanical frequency. Higher excitation frequency could ensure that at least half a wavelength is visible across the tissue of interest. However, there are two competing effects: (1) higher resolution at higher frequency, since the wavelength is smaller, but (2) higher attenuation due to stronger dampen, thus low signal. In order to overcome rapid wave attenuation at higher frequencies for this particular

application, *Yasar et al*. made an improvement in excitation setup, so called geometric focusing MRE (61). This vibration setup utilizes the focusing effect of cylindrically inward propagating waves. The target tissues are often embedded in the gel in a MRE tube. Considering axisymmetric harmonic vibrating the MRE tube vertically, and assuming a welded contact of the tube wall with the gel inside it, as the waves attenuate while traveling away from the tube wall, the attenuated waves are largely overcome by the geometric focusing effect. Yasar et al. have used the agarose and Ecoflex phantoms to show that geometrically focused shear waves acquired at a driven frequency of 5 kHz result in a more uniform amplitude throughout the entire region within the tube (61,62).

4 MRI EVALUATION OF TISSUE-ENGINEERED CARTILAGE

4.1 Introduction

The ultimate goal of cartilage tissue engineering is to produce an engineered tissue that functions as well as native cartilage (5,16). The ability of articular cartilage to serve as a load-absorbing and low-friction surface is attributable to its extracellular matrix (ECM): the three dimensional network of viscoelastic proteoglycans (PG) and tension-resistant collagen (6). Successful culture of ECM requires the synthesis of cartilage-specific molecules (e.g., type II collagen and PG) in a 3D pattern that closely resembles native tissue in its composition and structure. Evaluation of the structure and composition of ECM requires biochemical assays that are destructive and time consuming. Therefore, noninvasive MRI techniques are under active investigation for monitoring the matrix development of engineered cartilage tissue *in vitro* and *in vivo*.

Previous MRI studies of native cartilage and its degeneration have established the correlations between MRI parameters (such as T_2 relaxation time, $T_{1\rho}$ relaxation time, and ADC) and the PG, collagen and water content in cartilage tissues (63-66). Particularly, $T_{1\rho}$ is a more PG-sensitive and more reproducible measure than T_2 in native cartilage with enzymatic degradation (63,67,68). Since PG consists of a central core protein with multiple glycosaminoglycan (GAG) side chains, proton exchange between water molecules and NH and OH groups in GAG has been suggested to be an important contributor to $T_{1\rho}$ relaxation (69). The formation of engineered cartilage tissue is considered as a process of

accumulating such macromolecule-rich (PG and collagen) matrix by chondrocytes. It is thus expected that the changes in matrix composition and structure that occur during tissue growth can be reflected by the changes of MRI-based parameters (T_2, $T_{1\rho}$, and ADC).

Recent developments in high filed MRI (magnetic field > 7 T), particularly, with the capacity of the higher signal-to-noise ratio and spatial resolution have facilitated the MRI study of engineered tissue development. *Kotecha et al*. presented a comprehensive review of MRI contrast mechanisms in cartilage tissue engineering (28). For example, the T_2 was found to be correlated with the water, collagen, and PG contents of the synthesized matrix over a 4-week period in a hollow fiber bioreactor system; while the ADC was correlated well with the water and PG contents (70-75). Moreover, multi-exponential T_2 relaxation and multivariate analyses were shown to provide improved sensitivity to changes in matrix development in tissue-engineered cartilage (76,77). For $T_{1\rho}$, although a previous study has used $T_{1\rho}$ mapping to compare the characteristics between the week-8 cartilage-like tissue and native cartilage (78), to the best of our knowledge, it has not been fully analyzed to characterize the growth of engineered cartilage tissue and matrix components during the development. The objective of this part of study is, in addition to the conventional T_2 and ADC, to investigate the potential capability of $T_{1\rho}$ in its monitoring and evaluation of engineered cartilage growth.

As discussed in ***Chapter 2*** in ***section 2.2.2***, $T_{1\rho}$ has a feature known as $T_{1\rho}$ dispersion, i.e., $T_{1\rho}$ is dependent on the amplitude of the applied spin-locking (SL) pulse. In this chapter, to determine the most efficient SL pulse field at which $T_{1\rho}$ is

the most sensitive to PG change, a $T_{1\rho}$ dispersion was first characterized by varying the amplitude of SL pulse in chondroitin sulfate (CS) phantom with different concentrations. Here, CS was used because it is an important structural component of PG (~ 55-90%) (79). Next, since cartilage tissue itself has a natural distribution of PG and collagen across the cartilage depth, the sensitivities of MRI-based parameters (T_2, $T_{1\rho}$, and ADC) to the cartilage-specific macromolecules were validated in native bovine knee articular cartilage plugs. Finally, the validated T_2, $T_{1\rho}$ and ADC measurements was performed weekly on engineered cartilage tissues *in vitro* for up to 3 weeks. The MRI results were correlated with the PG and collagen contents determined by biochemical assays. In this study, a scaffold-free culture system was used to generate engineered tissues in a chondrocyte pellet culture. Although the scaffold-based culture has been used extensively in cartilage regeneration, the use of scaffolds raises the concerns of degradation and biocompatibility to the subsequent implantation (80). In contrast, a scaffold-free culture with careful mix of cells and growth factors avoids such possible, and has shown the encouraging results in the presence of PG and type II collagen *in vitro* and *in vivo (81,82)*.

4.2 Materials and Methods

4.2.1 Sample Preparation

a. Preparation of Chondroitin Sulfate Phantom

Four different concentrations of CS phantoms at 2.5% (w/v), 5%, 10%, and 20% were made, using double distilled water in the capillary tubes and then put in

a 10 mm diameter NMR tube for $T_{1\rho}$ measurements. ***Figure 4.1*** demonstrates the schematic structure of CS phantom.

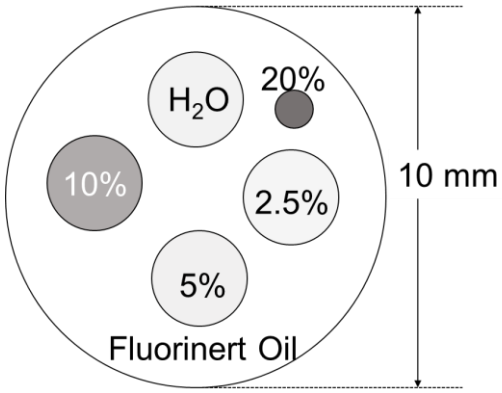

Figure 4.1. Schematic drawing of chondroitin sulfate (CS) phantoms prepared with five separate capillary tubes. Water (H_2O) is used as a standard liquid.

b. Preparation of Bovine Articular Cartilage Plug

Bovine knees were obtained from a 6-month-old bovine within 24 hours of death from the local slaughterhouse, and frozen at -80°C freezer before measurements. Thirteen cartilage plugs (4 mm diameter) with subchondral bone were harvested from non-weight bearing sides of medial femoral condyle using a 4 mm biopsy punch. For MRI measurement, each cartilage plug was placed in a 5 mm MRI tube filled with Fluorinert liquid to reduce susceptibility mismatch and to prevent dehydration, as illustrated in ***Figure 4.2***.

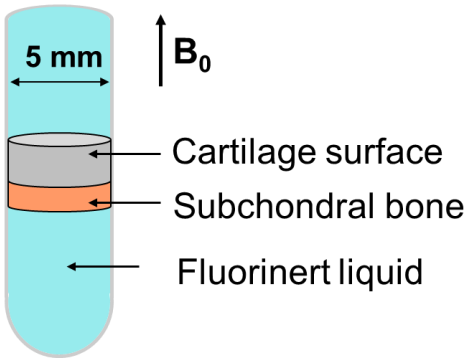

Figure 4.2. Schematic drawing of cartilage plug prepared in a 5-mm NMR tube. The imaging plane is parallel to the main magnetic field B_0.

c. Preparation of Scaffold-free Chondrocyte Pellet

Bovine metacarpophalangeal joints were obtained from an 18-month-old bovine within 24 hours of death from the local slaughterhouse. Bovine chondrocytes were harvested based on a previous protocol (83). Specifically, chopped slices of cartilage were acquire from the full depth of the joint. Chondrocytes were released from the enzymatic digestion of cartilage slices using 0.2% pronase (Calbiochem) for 1 hour followed by treatment with 0.025% bacterial collagenase P (Roche Applied Science) overnight at 37°C. The chondrocytes were collected by passing the digested mixture through a 70-µm filter and centrifuging the remainder at 1200 rpm for 10 minutes. The collected chondrocytes were re-suspended in Dulbecco's Modified Eagle's Medium/Ham's F-12 Nutrient Mixture (DMEM/F12) culture medium (Mediatech Inc.) containing 20% fetal bovine serum (FBS, Atlanta Biologicals) and 25 µg/mL ascorbic acid-2-phosphate (Sigma).

Next, a chondrocyte pellet was formed by transferring chondrocytes (at a density of 5×10^5 cells/mL) with culture medium into a 1.5 mL microfuge tube, and

centrifuging at 1000 rpm for 6 minutes. The resulting cell pellets were first cultured within the microfuge tube for 3 days in a 37°C, 5% CO_2 and 100% humidity incubator, and then were transferred into a 15 mL conical tube at day 3, and allowed to grow *in vitro* for 3 weeks. ***Figure 4.3*** shows the diagram of culture process of chondrocyte pellets. The tube lids were loosely capped to allow for gas exchange. The culture medium was changed every day for the first 3 days and every second day for the remainder of the culture period. The whole culture process was repeated by three times.

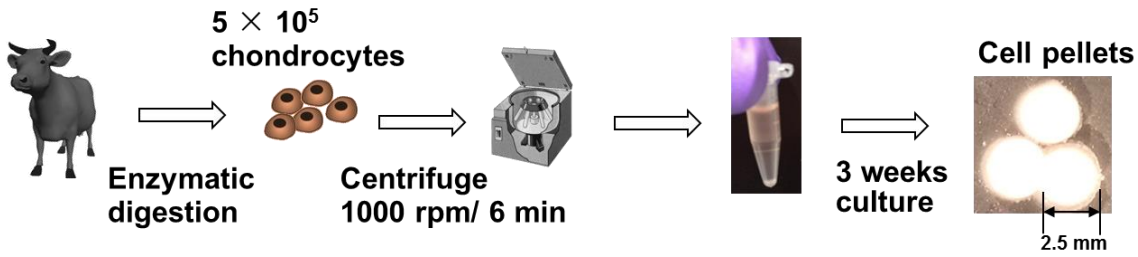

Figure 4.3. Flow diagram of culture process of chondrocyte pellets.

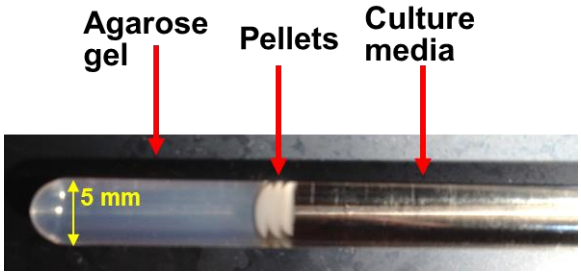

Figure 4.4. Scaffold-free chondrocyte pellets in a 5 mm MRI tube. The agarose gel is used as a biocompatible holder to maintain the center position of the pellets.

At each time point (day 3, 7, 14, and 21), three pellets (~ 2.5 mm diameter) were stacked in layers and placed into a 5 mm NMR tube filled with media for MRI study. ***Figure 4.4*** is the photography of chondrocyte pellets at week 1.

4.2.2 MRI System and Measurement Protocols

The MRI experiments were performed using a vertical bore (54mm diameter) Bruker DRX 11.74 T (500MHz for protons) Avance MR Spectrometer (Oxford Instruments). A Bruker linear triple-axis gradient system with a maximum magnetic field gradient strength of 200 G/cm and a microimaging probe were used for all experiments. The Bruker 5 mm and 10 mm saddle coils were used for imaging. The scanner platform is Bruker ParaVision Version 4.0. The whole MRI system is shown in ***Figure 4.5***.

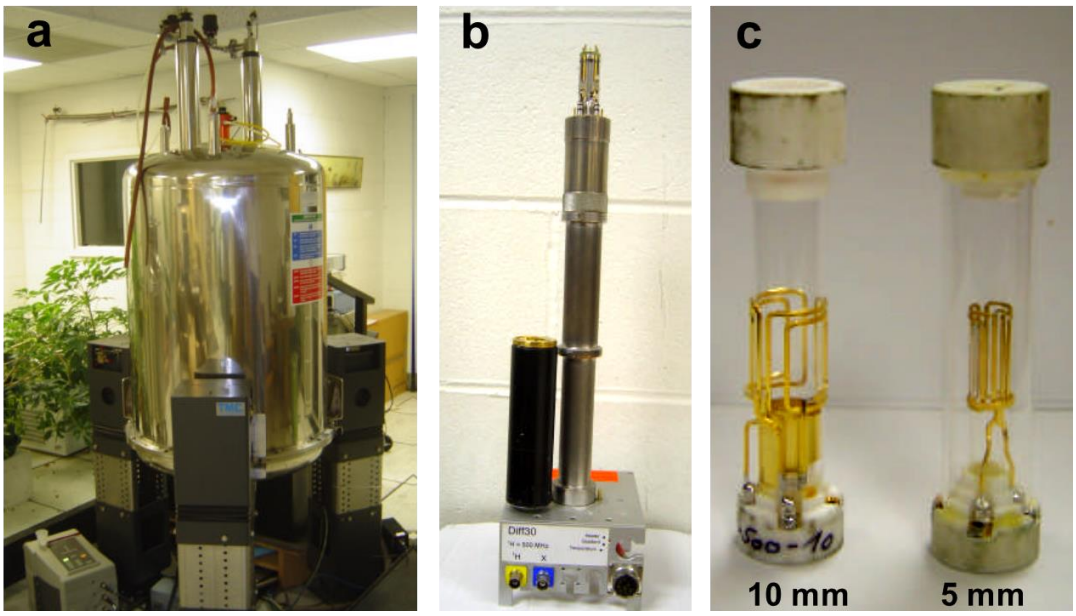

Figure 4.5. Bruker 11.7 T MRI System. (a) Bruker magnet of Avance MR Spectrometer. (b) Micro-imaging probe with a Bruker linear triple-axis gradient system. (c) Bruker 10 mm and 5 mm RF saddle coils.

a. $T_{1\rho}$ measurement

$T_{1\rho}$ relaxation time was measured using a self-compensation preparatory pulse followed by a manufacturer supplied fast spin-echo (FSE) imaging sequence (RARE, Bruker). The principle of this $T_{1\rho}$ sequence was introduced in ***section 2.2.3***. The self-compensation pulse was used here to correct the artifact induced by imperfect 90° pulse (***Figure 4.6***).

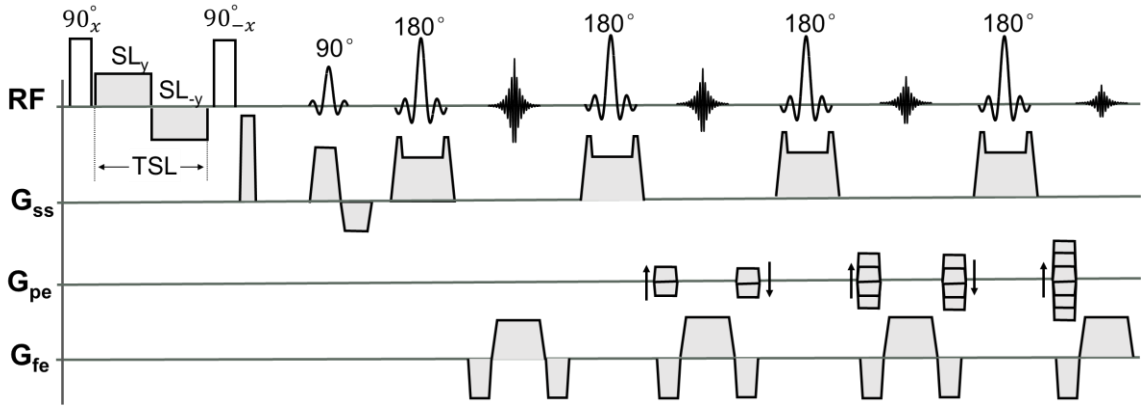

Figure 4.6. Diagram of $T_{1\rho}$ self-compensation FSE pulse sequence with echo train length of four in one TR (RARE factor = 4 for Bruker scanner).

To test it, an artifact was manually introduced by setting the flip angle of the first hard pulse to be 80°. Both images acquired without and with the self-compensation are shown in ***Figure 4.7***.

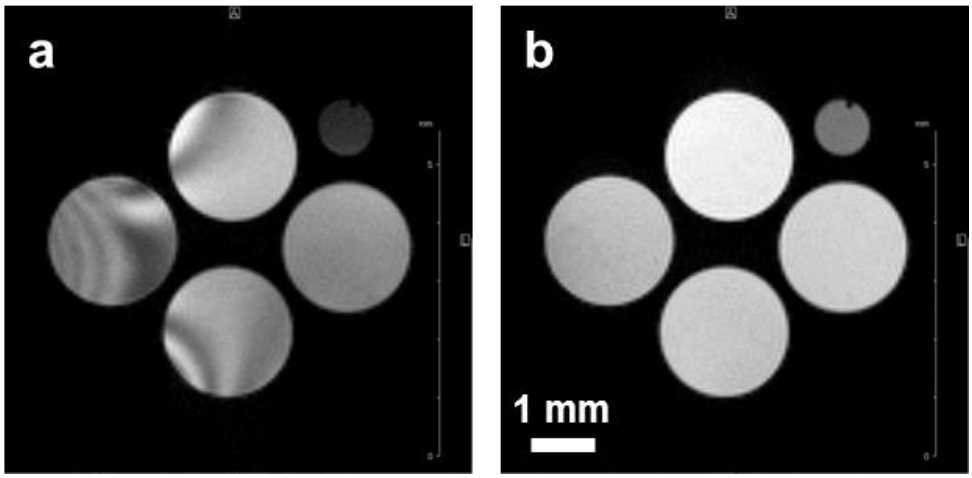

Figure 4.7. $T_{1\rho}$-weighted images acquired (a) without and (b) with self-compensation pulse sequence. The artifact in the (a) has been removed in the (b).

The $T_{1\rho}$ acquisition parameters for CS phantoms, cartilage plugs, and chondrocyte pellets are listed as follows.

CS phantom: TR/TE = 5000/8 ms; SL frequency: 300, 500, 800, 1000, and 1500 Hz; TSL at each frequency: 0, 20, 40, 80, 160, 320, and 400 ms; field of view (FOV) = 8 mm × 8 mm; matrix size = 128 × 128; in-plane resolution = 62.5 μm × 62.5 μm; axial slice, slice thickness = 2 mm.

Bovine cartilage sample: TR/TE = 3000/8 ms; SL frequency = 500 Hz; TSL = 0, 10, 20, 40, 80, 160 ms; FOV = 5 mm × 5 mm; matrix size = 128 × 128; in-plane resolution = 39 μm × 39 μm; sagittal slice, slice thickness = 0.5 mm; number of average = 2.

Chondrocyte pellets: TR/TE = 5000/8 ms; SL frequency = 500 Hz; spin-lock TSL = 0, 20, 40, 80, 160, 320, and 400 ms; FOV = 8.4 mm × 4.2 mm; matrix size

= 128 × 64; in-plane resolution = 67 µm × 67 µm; sagittal slice; slice thickness = 0.5 mm.

b. T_2 measurement

T_2 relaxation time was measured using a modified CPMG sequence based on a manufacturer supplied multi slice multi echo imaging sequence (MSME, Bruker). The principle of CPMG sequence was introduced in ***section 2.2.3***. The modification was made by placing the bipolar read-refocusing gradient pair after the 180° pulse to eliminate the diffusion losses (***Figure 4.8***) (84).

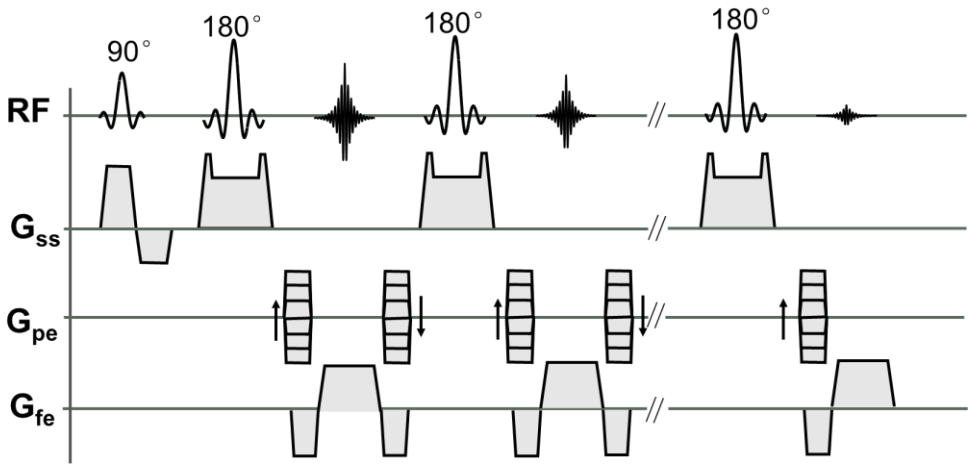

Figure 4.8. Diagram of T_2 CPMG pulse sequence with the bipolar read-refocusing gradient pair after the 180° pulse.

The T_2 acquisition parameters for cartilage plugs and chondrocyte pellets are listed as follows.

Bovine cartilage sample: TR = 5000 ms; TE: 7 ms – 224 ms, 32 echoes evenly spacing; FOV = 5 mm × 5 mm; matrix size = 128 × 128; in-plane resolution = 39 µm × 39 µm; sagittal slice, slice thickness = 0.5 mm; number of average = 2.

Chondrocyte pellets: TR = 5000 ms; TE: 5.8 ms – 448 ms, 64 echoes evenly spacing; FOV = 8.4 mm × 4.2 mm; matrix size = 128 × 64; in-plane resolution = 67 µm × 67 µm; sagittal slice, 3 slices; slice thickness = 0.5 mm.

c. ADC measurement

The ADC was measured using a manufacturer supplied diffusion-weighted spin-echo (DW-SE) imaging sequence (***Figure 4.9***, DtiStandard, Bruker). The principle of DW-SE sequence was introduced in ***section 2.3.3***.

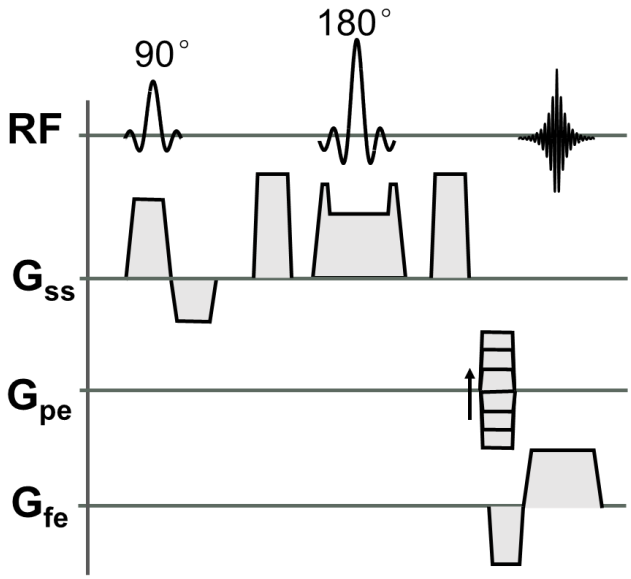

Figure 4.9. Diagram of DW-SE pulse sequence with diffusion gradient applied along the slice selection gradient direction.

The ADC acquisition parameters for cartilage plugs and chondrocyte pellets are listed as follows.

Bovine cartilage sample: TR/TE = 5000/25 ms; δ/Δ = 3/18 ms, b = 0, 200, 400, 600, 800, and 1000 s/mm^2; FOV = 5 mm × 5 mm; matrix size = 128 × 128; in-plane resolution = 39 µm × 39 µm; sagittal slice, slice thickness = 0.5 mm; number of average = 2.

Chondrocyte pellets: TR/TE = 5000/25 ms; δ/Δ = 3/18 ms, b = 0, 91, 234, 443, 717, 1057, and 1463 s/mm^2; FOV = 8.4 mm × 4.2 mm; matrix size = 128 × 64; in-plane resolution = 67 µm × 67 µm; sagittal slice, 3 slices; slice thickness = 0.5 mm.

4.2.3 Biochemical and Immunohistochemical Analysis

PG and collagen characterization: Cartilage samples were stored frozen for biochemical and IHC analysis after the MR experiments were completed. To determine the depth-wise PG concentration, after thawing, thirteen cartilage slices with a thickness of 100-µm were cut by layers from cartilage surface towards bone. The biochemical assays for PG and collagen characterization are based on the well-established protocols. Briefly, the cartilage slices or chondrocyte pellets, respectively, were subsequently treated with papain (100 µg/0.5 mL, Sigma) at 60 °C and digested overnight. The total PG content was measured using the dimethyl-methylene blue (DMB) assay based on a ratio of absorbance at 530/595 nm (83). The total collagen content was measured from aliquots of the papain digest of the pellets after acid hydrolysis (6.0 N HCl, 108 °C, 24 h) using a

colorimetric hydroxyproline assay (85). Using purified hydroxyproline standards, the total collagen content was calculated from 8.2 times the total hydroxyproline content. The measured PG and collagen contents were normalized to the wet weight (WW) of pellets.

Characterization of collagen types: frozen sections from separate pellets were stained with anti-type II (II6B3, Developmental Hybridoma Bank) and anti-type I collagen monoclonal antibodies (Sigma, #C-2456) to visualize the different types of collage (83). The collagen types were separated by SDS-PAGE (sodium dodecyl sulfate polyacrylamide gel electrophoresis) on 6% polyacrylamide gels in a Laemmli buffer system and stained with Coomassie blue. Purified rat tail type I collagen was used as a control.

4.2.4 Data Analysis

Custom software was written in MATLAB (Mathworks, MA, USA) to analyze the MRI data. A fully enclosed MATLAB toolbox was created that accepts raw data from Bruker scanner and allows for region of interest (ROI) selections to calculate the T_2, $T_{1\rho}$, and ADC parameters (***Figure 4.10***).

For data analysis, selecting ROIs covered the entire regions of CS phantoms and chondrocyte pellets. The T_2, $T_{1\rho}$, and ADC values were calculated through the mono-exponential fitting of the averaged MR signal to ***Eqs. 2.9, 2.13***, and ***2.17***, respectively. The T_2, $T_{1\rho}$, and ADC maps were created on a pixel-by-pixel basis using exponential fitting.

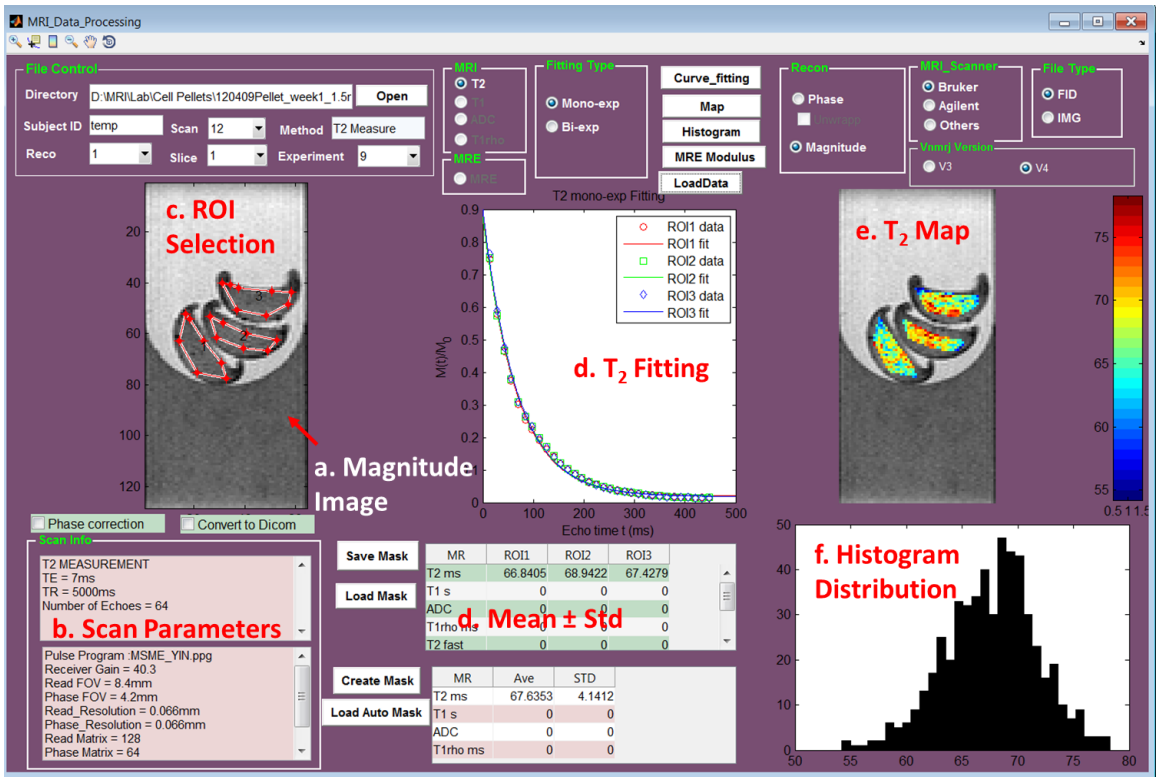

Figure 4.10. MATLAB Toolbox for MRI data processing. It has the functions of (a) accepting raw data from both Bruker and Agilent scanners, (b) retrieving acquisition parameters, (c) allowing the ROIs selection, (d) calculating T_2, T_1, $T_{1\rho}$, and ADC values, (e) creating T_2, T_1, $T_{1\rho}$, and ADC maps, and (f) generating T_2, T_1, $T_{1\rho}$, and ADC histograms. The T_2 data is used here as an illustration.

For CS phantom, the $T_{1\rho}$ dispersion was quantified by plotting $T_{1\rho}$ values over the different SL pulse amplitudes. For bovine cartilage samples, the MRI profiles along with cartilage depth were computed by averaging the columns across the cartilage over eight samples. For chondrocyte pellets, T_2, $T_{1\rho}$, and ADC values at each time point were calculated by averaging values from three culture groups. Both the MRI data and biochemical data are reported as mean ± standard deviation. For statistical tests, a one-way analysis of variance was performed to compare the means measured at each week over the 3-week culture period using

SPSS software (SPSS, Inc.). Pearson's correlation analysis was applied to assess the relationship between MRI parameters (T_2, $T_{1\rho}$, and ADC) and the corresponding PG and collagen content of the pellets. Statistical significance was set to $p < 0.05$.

4.3 Results

4.3.1 $T_{1\rho}$ dispersion of Chondroitin Sulfate Phantom

Figure 4.11 displays the $T_{1\rho}$-weighted image of CS phantoms with the strength of SL pulse = 500 Hz (12 μT) and TSL = 80 ms. It can be seen that signal intensity decreases as an increase of CS concentration, which indicates a shorter $T_{1\rho}$ relaxation time at higher concentration.

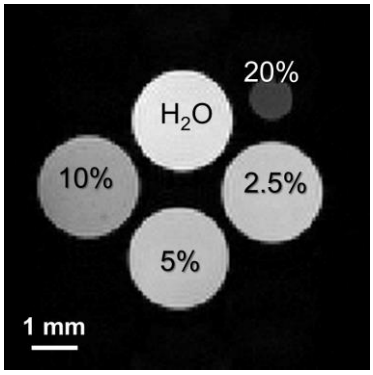

Figure 4.11. $T_{1\rho}$-weighted image (TSL = 80 ms) of CS phantoms at varying concentrations from 2.5 % to 20 %.

The $T_{1\rho}$ dispersion curve of CS is plotted in ***Figure 4.12*** as a function of the strength of the applied SL pulse. From this figure, it should be noted that (1) at any

given SL field, the $T_{1\rho}$ values of CS with lower concentrations are greater than that of higher concentrations; (2) there is a nonlinear increase in $T_{1\rho}$ relaxation time with the increase of SL filed strength; and (3) the $T_{1\rho}$ values plateaued between 1000 – 1500 Hz.

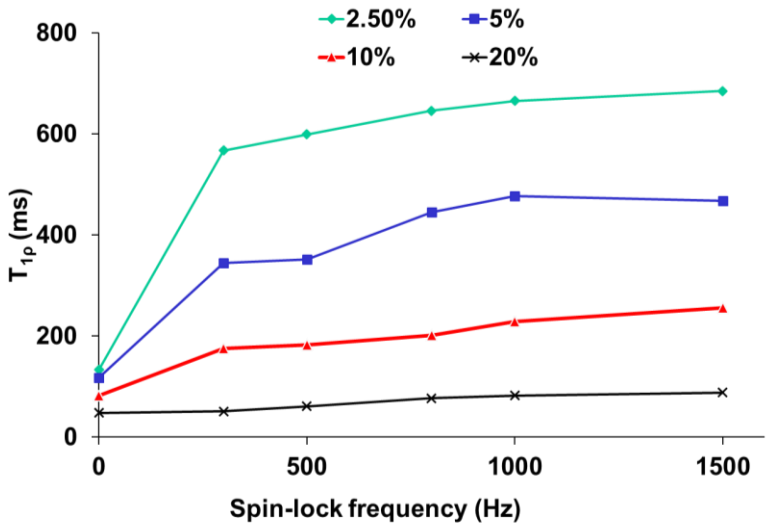

Figure 4.12. $T_{1\rho}$ dispersion curves of CS phantoms over a range of SL frequencies. $T_{1\rho}$ is a function of CS concentration, but is also a function of the amplitude the applied SL pulses. Note that the T_2 values of CS phantoms were used here as approximation of $T_{1\rho}$ values at SL frequency = 0 Hz.

4.3.2 Results of Bovine Cartilage Samples

The high resolution (39 × 39 × 500 μm^3) proton density-weighted (PDW) MR images and MRI maps from one bovine cartilage sample are shown in ***Figure 4.13***. The variations of the T_2, $T_{1\rho}$, ADC values, and PG content across the cartilage samples (n = 8, marked with red arrow in ***Figure 4.13***) – from the articular

surface towards the cartilage-bone interface – are plotted against the distance from cartilage surface in ***Figure 4.14***. Three cartilage zones – superficial zone (SZ), transitional zone (TZ), and deep zone (DZ) – are divided according to Ref (86).The bulk T_2, $T_{1\rho}$, and ADC distributions of three zones are shown in ***Figure 4.15***.

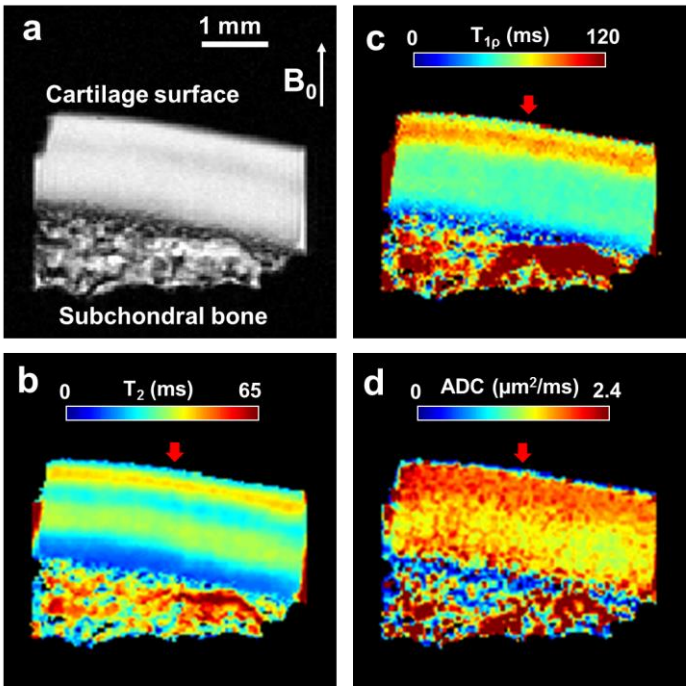

Figure 4.13. Illustrations of MRI maps of one bovine cartilage. (a) The PDW MR imaging with TE/TR = 5/3000 ms. The sagittal imaging plane is parallel to the B_0 field. The angle between the cartilage surface and the B_0 field was 80° for this sample case. (b) T_2 map. (c) $T_{1\rho}$ map. (d) ADC map.

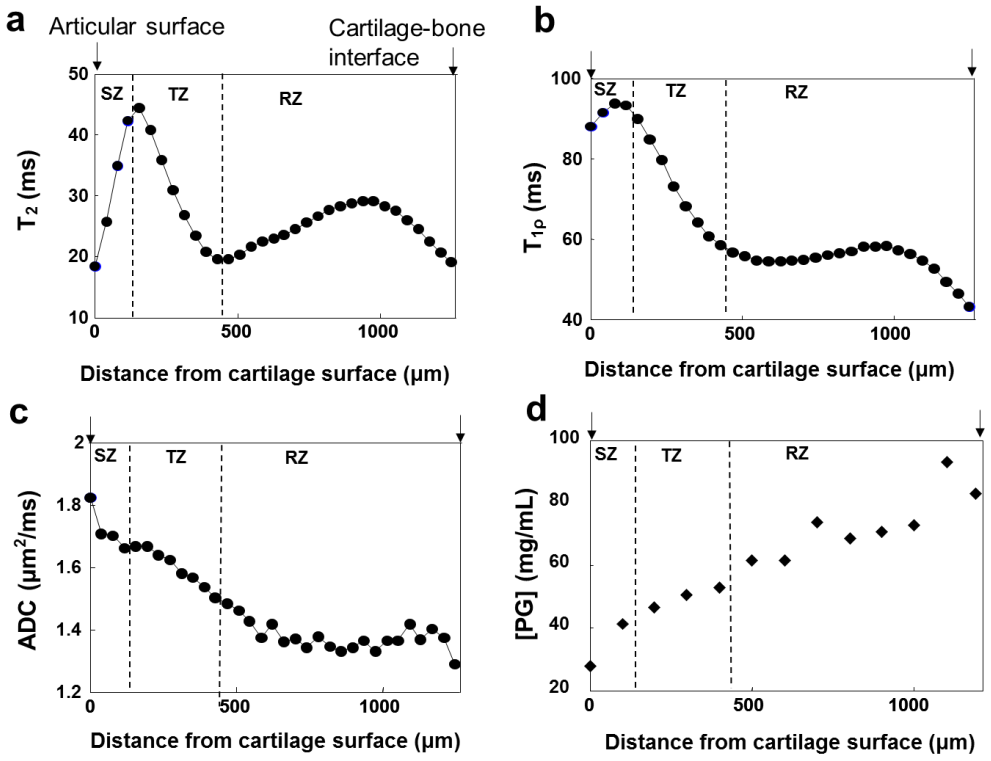

Figure 4.14. (a) T_2, (b) $T_{1\rho}$, (c) ADC, and (d) PG profiles along with cartilage depth. The MR profiles were computed by averaging the columns across the cartilage (marked by red arrows in Figure 4.13). Three different cartilage zones (SZ, TZ, and RZ) are defined according to Ref (86).

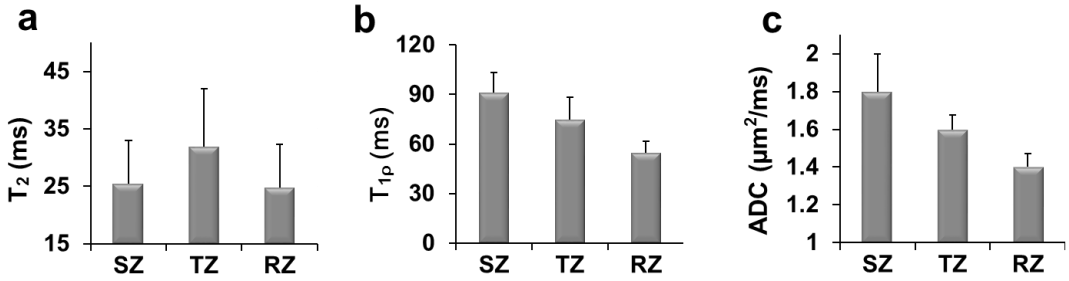

Figure 4.15. Bulk (a) T_2, (b) $T_{1\rho}$, and (c) ADC distributions of three cartilage zones. The averaged values were calculated based on the region divisions defined in *Figure 4.14*.

The laminar structure of cartilage is well revealed in the T_2 map (***Figure 4.13b***, ***Figure 4.14a***, and ***Figure 4.15a***) with short T_2 in SZ and RZ and long T_2 in TZ. The $T_{1\rho}$ map and profile show a decreasing tread with highest $T_{1\rho}$ values in the SZ (***Figure 4.13c***, ***Figure 4.14b***, and ***Figure 4.15b***). The ADC profile shows a monotonically decreasing trend from the SZ to the RZ (***Figure 4.13d***, ***Figure 4.14c***, and ***Figure 4.15c***). The depth-wise MR profiles were adjusted to 100-μm resolution for correlation analysis with PG (***Figure 4.16***). The PG content shows strong negative correlations with $T_{1\rho}$ ($r = -0.88$, $p = 0.0002$) and ADC ($r = -0.91$, $p = 0.00003$), while no correlation with T_2 ($r = -0.44$, $p = 0.16$).

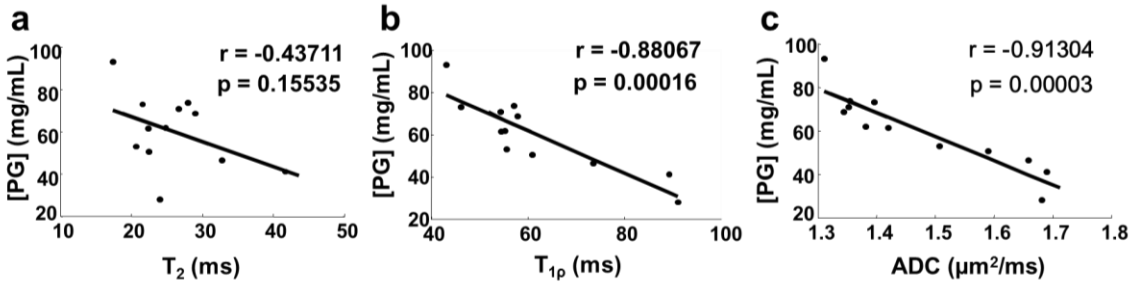

Figure 4.16. Scatter plots of the correlations between the PG concentration and (a) T_2, (b) $T_{1\rho}$, and (c) ADC of bovine cartilage tissues. The correlation coefficients and the corresponding p-values are shown in each graph.

4.3.3 Results of Chondrocyte Pellets

The sagittal T_2-weigthed images of chondrocyte pellets over 3-week culture are shown in ***Figure 4.17***. The intensities of the water signal in the MR images for the pellets decreased with tissue development. Increasing tissue heterogeneity

over time in each pellet is also observed. The initial chondrocyte pellets had conical shapes with smooth boundaries, and appeared homogenous. After two weeks of growth, the pellets appeared involuted with regions by hyper- and hypo- signal intensities in T_2-weighted images.

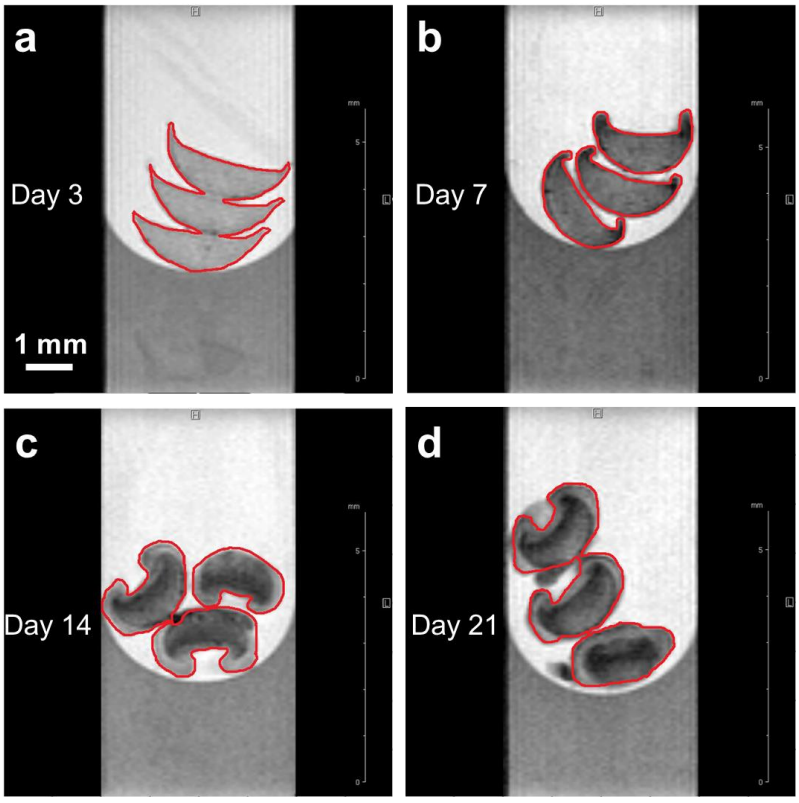

Figure 4.17. T_2-weigthed images (TE/TR = 56/5000 ms) of pellets cultured at different time points: day 3, 7, 14, and 21. Red contours indicate the ROIs selected.

Figure 4.18 shows the changes in $T_{1\rho}$, T_2, and ADC values for different growth stages of the chondrocyte pellets. The $T_{1\rho}$, T_2, and ADC decreased with an increase in culture time. More specifically, the $T_{1\rho}$ relaxation times were 198 ± 10

ms at day 3; with tissue development, this value dropped to 132 ± 12 ms by day 21 (34% decrease, $p < 0.05$). The T_2 relaxation times decreased from 79 ± 1 ms at the start of culture to 54 ± 3 ms at day 21 (32% decrease, $p < 0.05$). The ADC decreased from 1.46 ± 0.11 $\mu m^2/ms$ at day 3 to 0.98 ± 0.05 $\mu m^2/ms$ at day 21 (33% decrease, $p < 0.05$). The tissue heterogeneity is also reflected in the measured MR relaxation times: starting from day 14, regions near the periphery had longer relaxation times, corresponding to a time when T_2-weighted images revealed a more heterogeneous morphology (higher signal intensity near the periphery region).

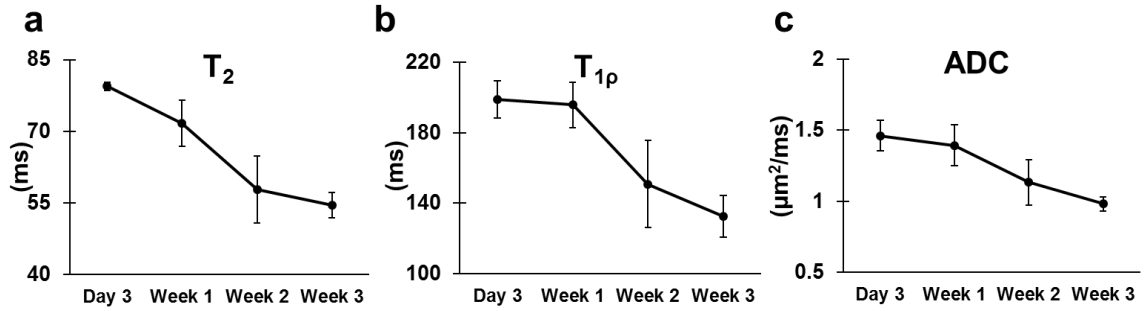

Figure 4.18. (a) T_2, (b) $T_{1\rho}$, and (c) ADC values of the pellets decreased with an increase of culture time. Values were averaged over three groups of pellets at each time point (n = 6 at each time point).

A progressive accumulation in both collagen and PG was observed during the 3-week culture period (***Figure 4.19***). The collagen content rose progressively from day 3 to week 3 (day 3: 0.05 ± 0.01 %; week 1: 0.08 ± 0.03 %; week 2: 0.10 ± 0.04 %; week 3: 0.16 ± 0.03 %). The PG content increased from 0.4 ± 0.3 % at

day 3 to 0.88 ± 0.1 % at week 3. The collagen and PG contents showed a significant increase from day 3 to day 21 ($p < 0.05$).

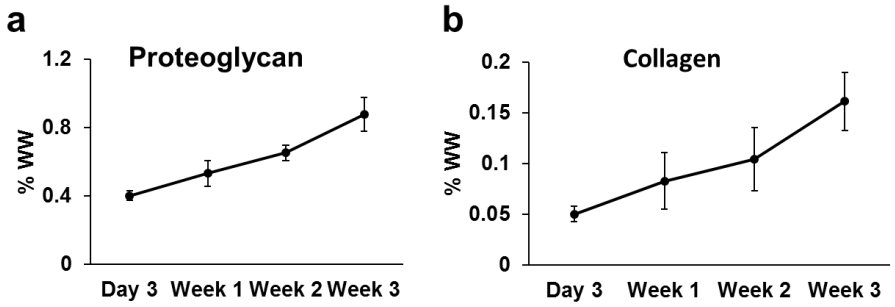

Figure 4.19. Accumulation of (a) PG and (b) collagen (%, normalized to WW) in the pellets over 3 weeks (n = 4 per time point).

Pearson's correlation analysis was performed to establish the correlation with the $T_{1\rho}$, T_2, and ADC values of the chondrocyte pellets and the PG and collagen contents (***Figure 4.20***). $T_{1\rho}$ showed a strong correlation with PG ($r = -0.867$, $p < 0.001$), but a relatively weaker correlation with collagen ($r = -0.757$, $p = 0.007$). Both T_2 and ADC are found to be strongly correlated with PG ($r = -0.803$, $p = 0.003$; $r = -0.848$, $p = 0.001$) and collagen ($r = -0.783$, $p = 0.004$; $r = -0.819$, $p = 0.002$).

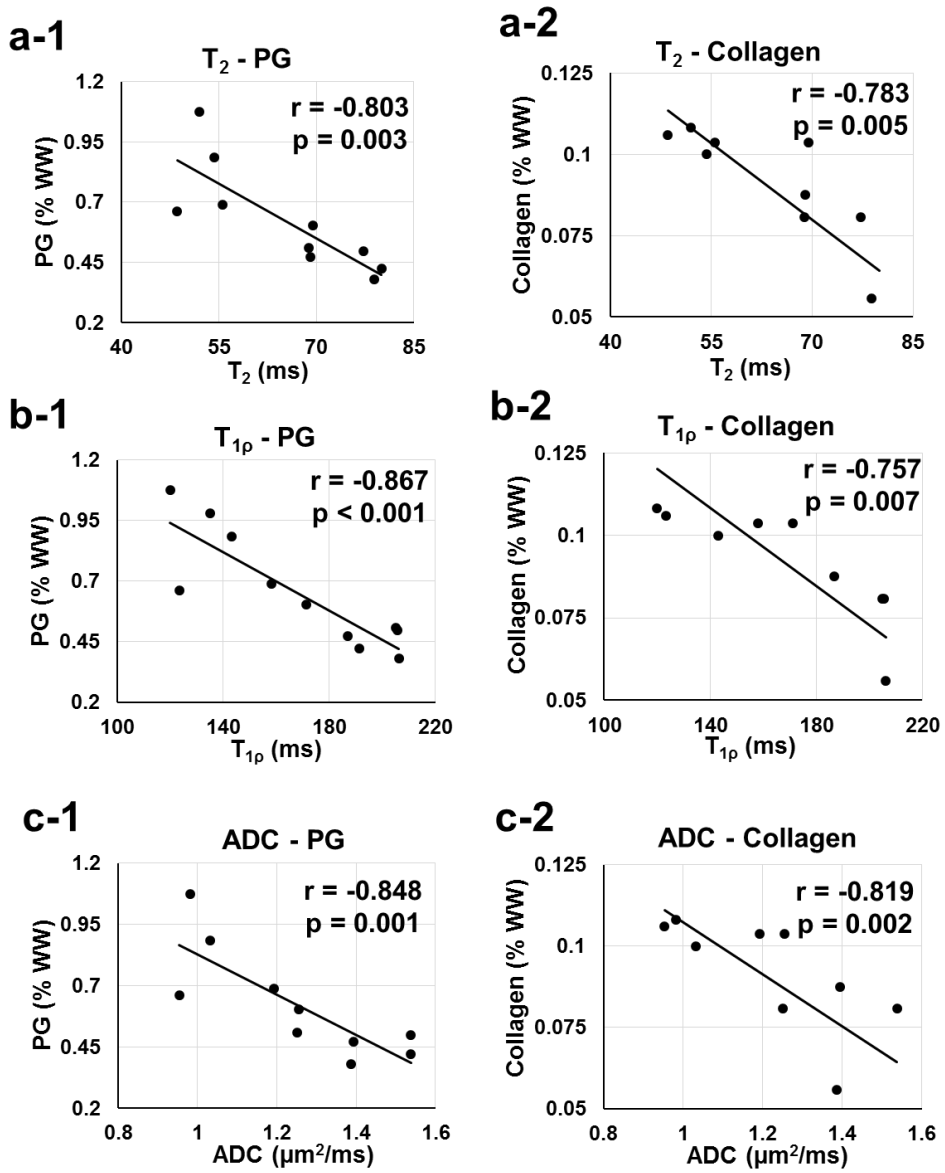

Figure 4.20. The correlations between (a-1) T_2 and PG, (a-2) T_2 and collagen, (b-1) $T_{1\rho}$ and PG, (b-2) $T_{1\rho}$ and collagen, (c-1) ADC and PG, and (c-2) ADC and collagen of chondrocyte pellets. The correlation coefficients and the corresponding p-values are shown in each graph.

As tissue heterogeneity was observed starting from week 2, the collagen type analysis was performed on week-2 pellets, and the staining results are shown in ***Figure 4.21***. Type II collagen was positively stained throughout the pellets at

week 2 using type II collagen antibody staining (***Figure 4.21b***). This was confirmed by SDS-PAGE results (***Figure 4.21c***). Pure type I collagen has a α1/α2 ratio of 2.0, while type II collagen only has a α1 chain with no α2 chain. Although a small amount of type I collagen was stained in the thin rim area surrounding the pellets (***Figure 4.21a***), only type II collagen was detected in the SDS-PAGE result.

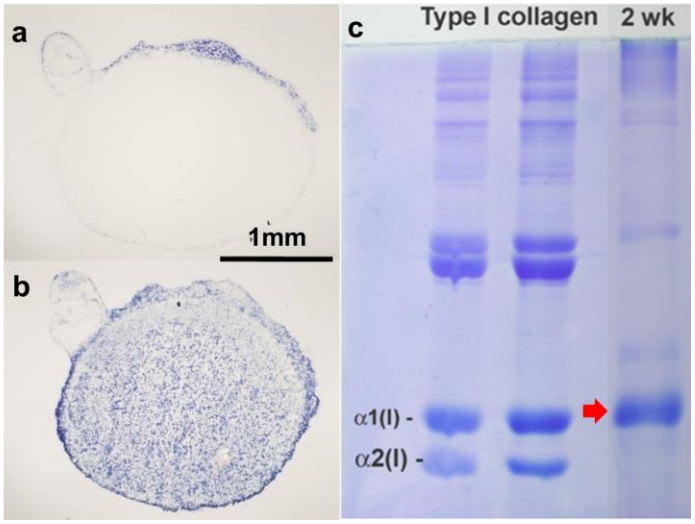

Figure 4.21. IHC results for (a) type I and (b) type II collagen on week-2 pellets. (c) Characterization of the types of the collagen accumulated on week-2 pellet (right column, red arrowhead). Purified rat tail type I collagen was run as a control (left 2 columns) to show the position of α(1) and α(2) chains.

4.4 Discussion and Conclusion

In this part of study, MRI was used to assess the matrix development of tissue-engineered cartilage by monitoring changes in MR $T_{1\rho}$, T_2, and ADC parameters in terms of PG and collagen accumulation.

PG contains a large number of negative side chains – GAGs, which immobilize water molecules at the charged surface. The major components of GAG is CS (79). So in order to determine the most efficient SL pulse field at which $T_{1\rho}$ is the most sensitive to PG change, a $T_{1\rho}$ dispersion was first characterized by varying the amplitude of SL pulse in phantoms with different CS concentrations. As shown in ***Figure 4.12***, at SL frequencies higher than 500 Hz, $T_{1\rho}$ shows a good sensitivity in the changes of CS concentrations. To reduce the RF power deposition as much as possible (87) while maintaining the maximum sensitivity, 500 Hz was chosen as the SL field strength in the following $T_{1\rho}$ studies of cartilage and chondrocyte pellets.

$T_{1\rho}$ map of bovine cartilage tissue showed a decreasing trend from the articular surface towards subchondral bone, while PG concentration increases from the SZ to the DZ (***Figure 4.13c***, ***Figure 4.14b***, and ***Figure 4.15b)***. The linear negative correlation demonstrated the previous reported correlations between $T_{1\rho}$ and PG. $T_{1\rho}$ is short in regions with higher PG concentration (***Figure 4.16b***). It is suggested that water protons undergo exchange with amide and hydroxyl protons in PG at a relatively low frequency, creating a slow motion with correlation time around 10^{-3}-10^{-4} s (69), which is a significant contributor to the low frequency (500 Hz in this study) $T_{1\rho}$ dispersion in cartilage tissues. Shorter $T_{1\rho}$ in the deep layer of the cartilage may be due in part to the increased proportion of slow motions as the increase of PG content.

In bovine cartilage tissue, no correlation was observed between T_2 values and PG content cross the cartilage depth (***Figure 4.16a***). Rather, T_2 map showed

a layered appearance (***Figure 4.13b***, ***Figure 4.14a***, and ***Figure 4.15a***), which also demonstrated the previous reported laminar appearance of T_2 map in native cartilage (64,86). T_2 values are prone to the magic angle effect due to spatial variations in collagen orientation (88). The cartilage has multiple layers with different patterns of collagen orientation. At a specific layer, for example, the collagen fibers may orient mainly around magic angle (~ 55°) to the main magnetic field. The dipole interaction between two protons falls to zero at magic angle, i.e., the two protons sense a small magnetic field variation from each other, and hence reducing the T_2 relaxation effect, resulting in a higher T_2 value at this layer.

Since ADC measures the mobility of water molecules in certain environment, the decreased ADC from the SZ to DZ indicates a more complicated matrix that hinders the isotropic movements of water molecules in the deep layer of cartilage. Furthermore, the strong negative correlation between ADC and PG enhances the fact that interactions between water molecules and PG result in more hindered water molecules within the DZ, causing an overall decrease of ADC.

The MR $T_{1\rho}$, T_2, and ADC studies of native cartilage tissue suggested that, within a highly ordered matrix structure, $T_{1\rho}$ is more sensitive to the changes of PG than T_2, whereas T_2 is prone to the collagen orientation that enables the detection of structural and compositional changes in collagen, and ADC can reflect the overall change of matrix complexity. Then validated $T_{1\rho}$, T_2, and ADC methods were used as biomarkers to study the development of tissue-engineered cartilage.

To the best of our knowledge, this work provides the first $T_{1\rho}$ relaxation time characterization of the growth of engineered cartilage in an *in vitro* system.

Although there was one study using $T_{1\rho}$ to compare an 8-week cartilage-tissue with native cartilage tissue (78), it only provided a single time-point measurement and did not show the change of $T_{1\rho}$ during the tissue development. In the current study, the stronger correlation between $T_{1\rho}$ and PG ($r = -0.867$, $p < 0.001$) than $T_{1\rho}$ and collagen ($r = -0.757$, $p = 0.007$) suggests that, the dominant proton changes between water and the synthesized amide and hydroxyl groups in PG dominate the $T_{1\rho}$ relaxation processes. With an increasing of PG content during tissue growth, more water molecules start to interact with PG, resulting an overall increase of slow motions from the lattice. Correspondingly, $T_{1\rho}$ was decreased over time during tissue development.

It is interesting to note that T_2 showed no correlation with PG in native cartilage tissue ($r = -0.44$, $p = 0.16$), but a strong correlation with PG in engineered cartilage tissue ($r = -0.803$, $p = 0.003$). This indicates that the low frequency exchange of PG side groups with water protons affects not only the $T_{1\rho}$ relaxation, but also the T_2 relaxation. However, in native tissue, the dipolar interaction on collagen due to magic angle effect masks out the changes in T_2 due to exchange mechanism. In tissue-engineered cartilage, because the mature collagen network has not yet been completely formed, i.e., collagen fibers are not heterogeneously oriented but of random nature, the T_2 relaxation is, therefore, subject to both proton exchange on PG, and dipolar interaction on collagen. T_2 is then dependent on both collagen and PG contents in chondrocyte pellets.

Although ADC has the same decreasing trend as T_2 and $T_{1\rho}$ and also correlates with both PG ($r = -0.848$, $p = 0.001$) and collagen ($r = -0.819$, $p = 0.002$)

contents, it provides a different information in terms of matrix development from T_2 and $T_{1\rho}$. The mechanism of MR diffusion determines that any structural changes would alter the way that water molecules diffuse, thus leading to a change in ADC. During tissue growth, the synthesized matrix develops from a gel into a more solid-like phase as the macromolecules (PGs and collagen) form large insoluble macromolecular complexes around and between the chondrocytes. The increasing heterogeneous tissue compartments could slow down the motions of water molecules, and cause a decrease in ADC values. The T_2 and ADC results are consistent with pervious MRI studies in which a decrease in T_2 and ADC during the growth of engineered cartilage tissue was reported (70-72,74,75). Conversely, an increase in T_2 has been reported in a scaffold-based engineered tissue in which they inferred that the increase might be affected by the agarose scaffold (73).

The formation of hyaline-like engineered cartilage in a scaffold-free pellet culture was confirmed by the synthesis of type II collagen and PG. The expression of type II collagen is a well-accepted marker for the differentiated phenotype of chondrocytes (89). Although a thin rim area of growth tissue on the edges of pellets tends to be stained as type I collagen, it is clear from the SDS-PAGE results that the chondrocytes maintained their phenotype by synthesis of type II collagen. The positive stain for type I collagen at the edge could be due to a very small amount of type I collagen in the pellets; however, type I collagen synthesis was almost negligible.

In this chapter, in addition to the conventional T_2 and ADC, we have shown that $T_{1\rho}$ can be used as a potential biomarker to assess the specific changes in PG content of engineered cartilage during tissue growth.

5 MRE EVALUATION OF TISSUE-ENGINEERED CARTILAGE

5.1 Introduction

As introduced above, the ability of cartilage to resist compressive loads and internal shear stresses relies on the functional integrity of its extracellular matrix (ECM). The ECM consists of a solid network of macromolecular polymers (PG and collagen) surrounded by a fluid phase of water (6). The frictional interactions between the solid and fluid phases establish the viscoelastic behavior of cartilage, which is important for normal lubrication and load transmission in the joint (90). In the event of injury, when this integrity is breached, the avascular nature of cartilage limits the self-repair of the damaged cartilage. Therefore, implantation of tissue-engineered cartilage is being explored as a potential therapy.

Current efforts in cartilage tissue engineering have focused on optimizing the mechanical properties of the implant to withstand the loading conditions after transplantation (91). While a variety of culture systems, growth factors and mechanical stimuli have been developed to fulfill this requirement, optimal strategies are not yet fully established. Ideally, the successful engineering of cartilage implants should restore the viscoelastic properties of native cartilage. Cartilage exhibits flow-dependent and flow-independent viscoelasticity under different forces. Compressive loading causes interstitial fluid flow within the matrix, so the resulting viscoelastic behavior of cartilage is mainly due to the resistance to fluid flow through the ECM. In contrast, the interstitial fluid flow is minimal in shear, and the measured properties largely depend on the deformations of the solid ECM

rather than the fluid exudation and redistribution (92). Given that the viscoelastic properties of the solid ECM from flow-independent measurements are highly sensitive to biochemical alterations of the matrix constituents (90), it is therefore important to frequently monitor the flow-independent viscoelastic properties of the engineered cartilage throughout its development.

Shear testing by small torsional displacements has been widely used to study the viscoelastic properties of the solid ECM of engineered cartilage under flow-independent conditions (20,92). However, such methods only give the bulk or average properties of the sample rather than the specific mechanical properties of local tissues. To address this problem, imaging-based methods, such as MRI, have emerged as a promising way to nondestructively visualize the deformation and to measure the mechanical properties of soft tissues (56). MRI spin-tagging registration and MRI phase contrast methods have been used to track the deformation of cartilage explants (native and engineered) under static or cyclic compressive loading (93,94). Although these MR-based methods can help elucidate the compressive properties of engineered tissues, they cannot decouple the solid matrix viscoelastic effects from the flow-dependent viscoelastic effects under compression. In contrast, MRE has been proposed as a nondestructive way to measure the shear modulus (or shear stiffness) of soft tissues under dynamic shear loading (25,26). MRE uses small shear displacements (~ microns) and enables direct assessment of shear properties of the solid ECM. The measured shear modulus (or stiffness) thus only reflects the deformation of the solid ECM network produced by cells.

Microscopic MRE (micro-MRE or μMRE) has extended MRE to the submillimeter scale to image shear waves in biological tissues and engineered tissues with high spatial resolution (59,95-97). As introduced in ***Chapter 3***, micro-MRE is achieved by coupling a mechanical actuator to the targeted sample. A phase-contrast MRI technique is used to visualize and quantitatively measure propagating shear waves in the sample subjected to harmonic mechanical excitation. From the observed wave pattern, the local shear stiffness can be calculated on a pixel-by-pixel basis to provide a quantitative tissue stiffness map. Such maps can be used to depict changes of the ECM stiffness during tissue development. In previous studies conducted on larger engineered bone and fat tissues (4-5 mm), micro-MRE was applied using surface excitation at frequencies between 20 Hz – 2 kHz to assess changes in shear stiffness at different growth stages (95-98). However, using micro-MRE to evaluate even smaller sizes (2-3 mm) of stiffer engineered cartilage tissues (e.g., above 100 kPa) is challenging as it requires a higher excitation frequency (> 2.5 kHz) to shorten the shear wavelength. One drawback of an increased excitation frequency is an increased wave attenuation in the targeted tissue (99). To overcome rapid wave attenuation at higher frequencies in a relatively small and stiff material, *Yasar et al.* have developed a geometric focusing method for *in vitro* micro-MRE by utilizing the focusing effect of cylindrically inward propagating waves (61). In geometric focusing micro-MRE, the samples are embedded into an agarose gel in a test tube. A small, harmonic shear displacement is applied to the samples by vibrating the entire tube axially at the desired high frequency (1 – 10 kHz). This motion

generates a uniform axisymmetric shear wave that propagates concentrically inward. The waves attenuate as they travel away from the tube wall due to viscous loss in the gel and the embedded sample, but this attenuation is largely overcome by the geometric focusing. Previous studies have demonstrated the potential of this approach to assess the shear viscoelastic properties of the soft gel sample/phantom using shear waves in the frequencies range from 200 Hz to 7.75 kHz (62,100).

The objective of this part of study was to apply this geometric focusing micro-MRE method (at 5 kHz) to quantify the biomechanical shear properties of tissue-engineered cartilage *in vitro*, demonstrating the sensitivity of micro-MRE measurement over a range of material properties. Specifically, we first tested this new technique by monitoring the changes of shear stiffness in a calcium cross-linked alginate bead model, whose mechanical behaviors can be modified by exposure to different ion concentrations (101). Then we used geometric focusing micro-MRE to evaluate changes in the shear stiffness of scaffold-free engineered cartilage tissues (chondrocyte pellets) during a 3-week culture period. The MRE results were correlated with biochemical analyses of the PG and collagen content in the chondrocyte pellets.

5.2 Materials and Methods

5.2.1 Sample Preparation

a. Preparation of Alginate Bead

Calcium cross-linked alginate beads (~ 2.5 mm diameter) were made using an extrusion-dripping method (83). Briefly, alginate (Sigma) was dissolved in a 0.15 M NaCl solution. Low viscosity sodium alginate solutions (1.2% w/v) were slowly extruded through a 22-gauge needle into spherical drops that immediately fell into a $CaCl_2$ solution (102 mM). The resulting beads were allowed to polymerize in $CaCl_2$ solution for 10 minutes before two consecutive washes with 0.15 M NaCl solution to remove the unbounded, free calcium ions.

b. <u>Preparation of Chondrocyte Pellet</u>

Chondrocyte pellets were prepared and cultured the same as introduced in ***Chapter 4*** (***section 4.2.1***). At the end of each week, sample pellets (~ 2.5 mm diameter) taken from the incubator for MRE and biochemical analysis.

c. <u>Micro-MRE Sample Preparation and Experimental Design</u>

For each micro-MRE experiment, three samples were embedded in 1% (w/v) agarose gel (Lonza) in a 10 mm customized MRE plastic tube. The agarose gel was used to promote the transfer of shear wave motions into the enclosed samples. The temperature of the agarose solution was approximately 37°C to minimize damage to the embedded samples. The agarose was allowed to congeal at room temperature for 10 minutes prior to the start of the measurements.

In the first experiment, the mechanical properties of the embedded alginate beads were modified by changes in the surrounding agarose gel. Two groups of agarose gels were prepared by dissolving agarose 1% (w/v) in tissue culture medium (DMEM/F12) or in a 1 mM $CaCl_2$ solution. The medium-based gel was

used to induce changes in the mechanical properties of the alginate beads, while the calcium-based gel was used as a control in which the concentration of $CaCl_2$ was chosen to match its respective concentration (1 mM) in culture medium (101,102). The shear stiffness of the beads was measured every 30 minutes for 7 hours by micro-MRE.

In the second experiment, the chondrocyte pellets were taken weekly for micro-MRE analysis. The 1% (w/v) medium-based agarose gel was used to enclose the pellets. The medium-based agarose was required here to maintain chondrocyte cell viability by minimizing osmotic and pH changes between gel and enclosed living constructs. To confirm the mechanical stability of our gel/pellet preparations, the shear stiffness of the week 1 pellets were measured every 30 minutes for 4 hours.

5.2.2 Micro-MRE Setup and Measurement Protocols

MRE experiments were performed on the same MRI system as introduced in ***Chapter 4*** (***Figure 4.5***): a vertical bore (54 mm diameter) Bruker DRX 11.74 T (500 MHz) Avance MR Spectrometer, a Bruker linear triple-axis gradient system (maximum gradient strength of 200 G/cm), a micro-imaging probe, and a Bruker 10 mm saddle coil.

The design and implantation of the micro-MRE actuation system can be found in previous publications (61,62). Specifically, as illustrated in ***Figure 5.1***, steady state harmonic mechanical motions (5 kHz) were generated using a

piezoceramic stack actuator, which can provides 11.6 µm displacements at 100 volts.

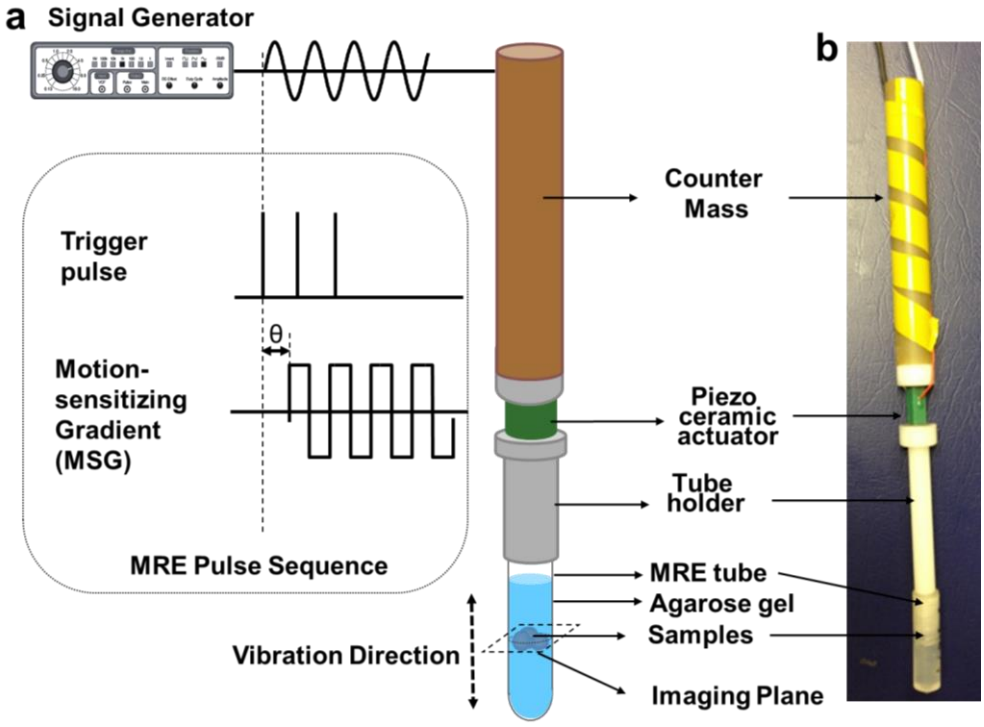

Figure 5.1. (a) Diagram of micro-MRE setup. The MRE pulse sequence that encodes the mechanical motion through the application of MSG is shown at the bottom left. The piezoceramic actuator applies concentrically focused shear waves to the gel-embedded samples by vibrating the entire test tube axially at 5 kHz. The MSG and the actuator are synchronized using trigger pulses sent from the MRI scanner (adapted from (103)). (b) Photography of micro-MRE setup.

The mechanical actuator assembly was fixed to the top of a 10 mm diameter MRE cylindrical tube that contains the gel-embedded pellets or beads, while the RF saddle coil was positioned on the outside of the test tube, and with its center aligned with the middle of the sample. A key aspect of this assembly is that the

vertical motion of the wall of the MRE tube serves as the source of the concentrically focused shear wave propagating uniformly into the gel/bead or pellet sample. Before starting the MRE pulse sequence, the MR system sent a trigger to a function generator (33220A Function/Arbitrary Waveform Generator, 20 MHz, Agilent Technologies Test and Measurement, Englewood, CO) to initiate the mechanical motion and synchronize with the MSGs.

The MRE experiments were acquired using a modified MRE sequence based on a manufacturer supplied gradient echo imaging sequence (***Figure 5.2*** FLASH, Bruker).

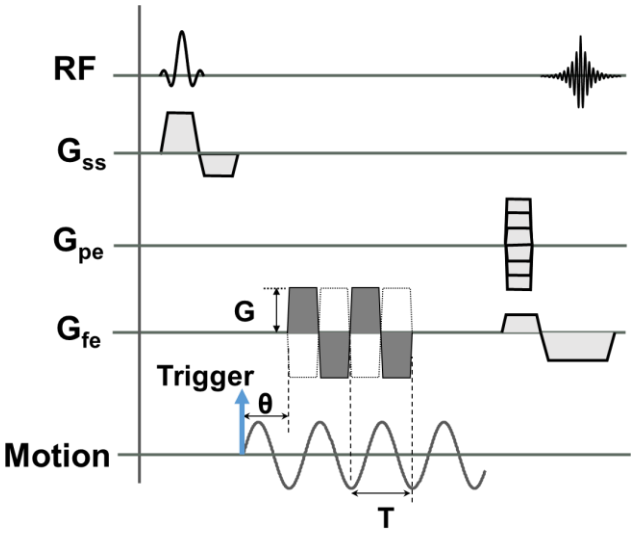

Figure 5.2. The diagram of gradient echo-based MRE sequence with trapezoid MSG (solid line) as well as negative MSG (dotted line). Please see Ref (30) for details about gradient echo sequence.

The acquisition parameters were: TR/TE = 1000/6 ms; flip angle = 30°; FOV = 10 mm; slice thickness = 0.5 mm; 2 slices; in-plane resolution = 78 μm × 78 μm; MSG strength = 120 G/cm. To monitor the propagation of the shear wave, eight temporal measurements were obtained by shifting the phase offset θ between the MSG and vibrational motion. At each time step, two MR phase images were acquired. One was acquired with the MSGs as illustrated in ***Figure 5.2*** (solid line), and another was acquired after reversing the polarity of the MSGs (dotted line). The phase difference (wave) image was formed by complex division of two phase images. The T_2-weighted MR images were also acquired by using a SE sequence with the following imaging parameters: TR/TE = 3000/64 ms; field of view = 10 mm; slice thickness = 0.5 mm; in-plane resolution = 78 μm × 78 μm.

5.2.3 Biochemical Analyses

Each week, separate pellets (n = 5) were first blotted dry and weighed to obtain the wet weight (WW). The pellets were subsequently digested with papain for PG and collagen content determination. The same biochemical assays were used as introduced in ***Chapter 4*** (***section 4.2.3***). The measured PG and collagen contents were then normalized to the WW of pellets.

5.2.4 Data Analyses

A custom-made MATLAB (MathWorks, Inc.) program was used to calculate the shear stiffness and to create stiffness maps (***Figure 5.3***). The shear stiffness values were calculated according to ***Eq. 3.11***. The wavelengths λ were estimated using a 2D local frequency estimation (LFE) algorithm (104). For data analysis,

selecting ROIs covered the entire regions of the embedded samples. The shear stiffness maps were created on a pixel-by-pixel basis.

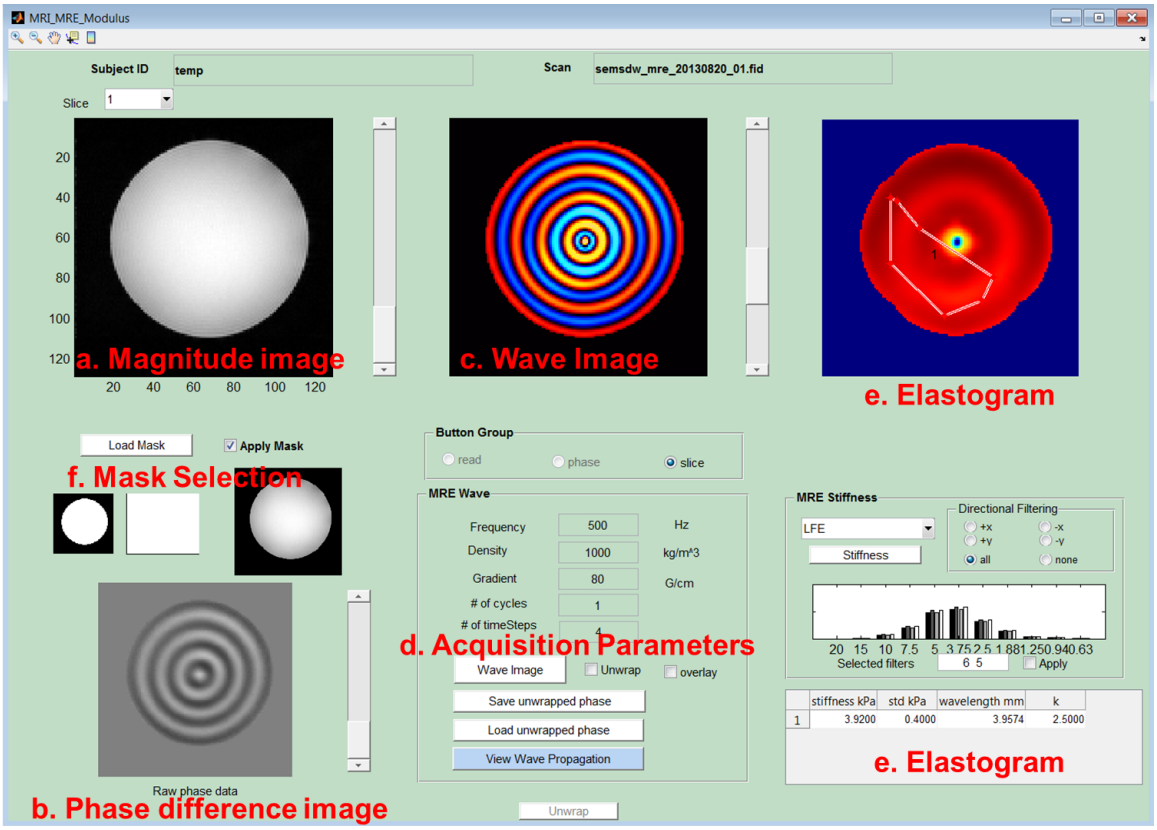

Figure 5.3. MATLAB Toolbox for MRE data processing. It has the functions of (a-b) accepting raw magnitude and phase data from both Bruker and Agilent scanners, (c) calculating 3D complex wave images, (d) retrieving acquisition parameters, (e) calculating shear stiffness values based on the selected ROIs, and (f) allowing the mask selection. The gel MRE data is used here as an illustration.

Both the MRE data and biochemical data are reported as mean ± standard deviation. . For statistical tests, a one-way analysis of variance was performed to compare the means measured at each week over the 3-week culture period using

SPSS software (SPSS, Inc.). Pearson's correlation analysis was applied to assess the relationship between shear stiffness and the corresponding PG and collagen contents of the pellets. Statistical significance was set to $p < 0.05$.

5.3 Results

5.3.1 Results of Alginate Beads

The MRE-derived shear stiffness of alginate beads was measured over 7 hours following embedding in two different formulations of agarose gels (***Figure 5.4***). The shear stiffness of beads embedded in the medium-based gel decreased from 8.45 ± 0.23 kPa to 2.01 ± 0.09 kPa over 7 hours, while no change in shear stiffness was observed in beads suspended in a calcium-based agarose gel.

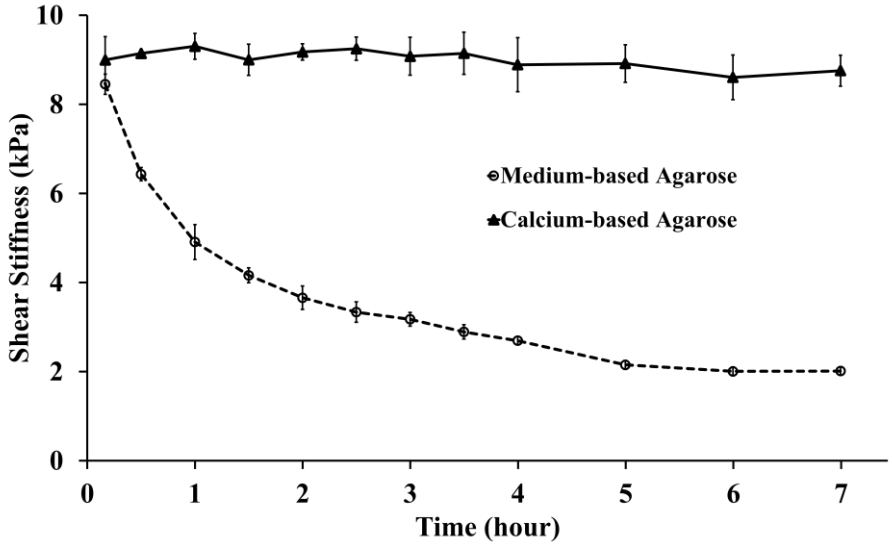

Figure 5.4. MRE-derived shear stiffness at 5 kHz of alginate beads embedded in calcium-based (▲) and medium-based (○) agarose gels plotted versus time. The beads enclosed in the calcium-based gel were mechanically stable, while the beads suspended in the medium-based gel became softer. The plotted values represent mean ± standard deviation (n = 6 per group) (adapted from (103)).

Shear wave images of alginate beads embedded in the medium-based agarose gel for 10 minutes, 1 hour, and 7 hours are displayed in ***Figure 5.5a-1, a-2, a-3***, respectively. The corresponding T_2-weighted MR images (with a voxel resolution of 78 × 78 × 500 μm^3) are shown in ***Figure 5.5b-1, b-2, b-3***. Finally, the computed shear stiffness maps at 10 minutes, 1 hour and 7 hours generated by the LFE algorithm are presented in ***Figure 5.5c-1, c-2, c-3***. In these figures, it is observed that the shear wavelength decreases over time with the swelling of beads. The shorter wavelength reflects softer samples with averaged shear stiffness at the measured times of 8.45 ± 0.23 kPa, 4.91 ± 0.39 kPa, and 2.01 ± 0.09 kPa, based on the wavelengths of 0.6 mm, 0.43 mm, and 0.28 mm, respectively.

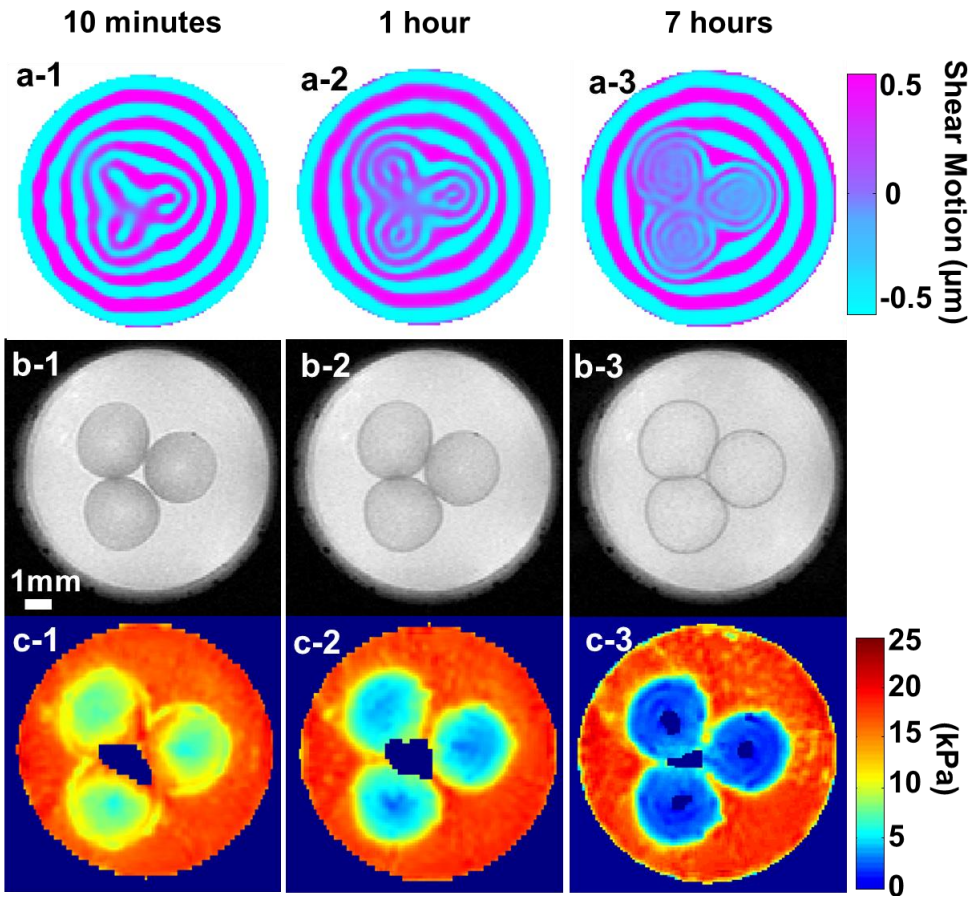

Figure 5.5. Micro-MRE results of alginate beads embedded in the medium-based agarose gel. The first column displays alginate beads measured 10 minutes after embedding in the medium-based gel; the middle column displays beads at 1 hour after embedding, and the last column presents beads embedded for 7 hours. The first row (a-1, a-2, a-3) displays the shear wave images of an axial slice of the beads. The second row (b-1, b-2, b-3) displays the corresponding T_2-weighted MR images. The third row (c-1, c-2, c-3) displays the shear stiffness maps (adapted from (103)).

5.3.2 Results of Chondrocyte Pellets

Although the medium-based agarose gel induced stiffness changes in alginate beads, no change in shear stiffness was observed for chondrocyte pellets after embedding in the medium-based agarose gel over 4 hours (***Figure 5.6***).

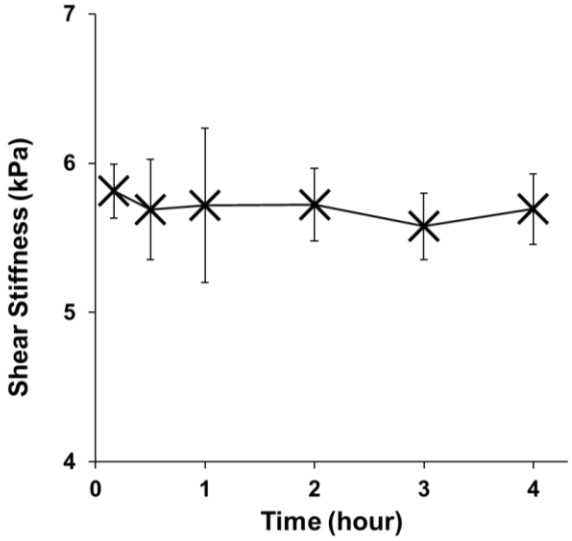

Figure 5.6. Shear stiffness of pellets embedded in the medium-based agarose gel plotted versus time at week 1 (adapted from (103)).

The shear stiffness of the chondrocyte pellets was measured over 3 weeks. Shear wave images of chondrocyte pellets acquired each week are shown in ***Figure 5.7a-1, a-2, a-3***, respectively. We observed an increase in the wavelength within the constructs with tissue development. The corresponding shear stiffness maps generated by the LFE algorithm are presented in ***Figure 5.7b-1, b-2, b-3***. As shown in ***Figure 5.8***, the shear stiffness of the pellets increased from 6.19 ± 0.57 kPa at week 1 to 12.01 ± 1.06 kPa at week 2, to 16.45 ± 0.46 kPa by the end of the third week, based on the wavelengths of 0.5 mm, 0.63mm, and 0.8 mm, respectively. There was a significant increase in shear stiffness between successive weeks ($p < 0.05$).

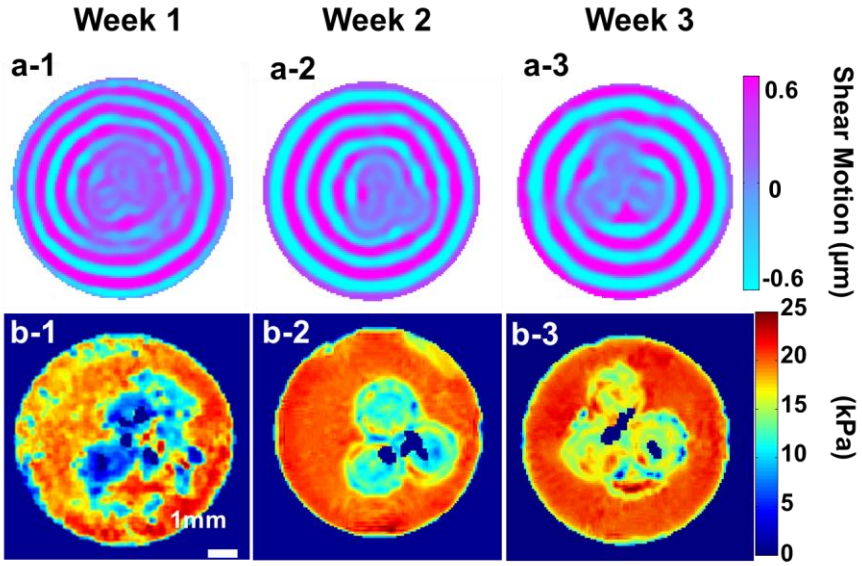

Figure 5.7. Micro-MRE results of chondrocyte pellets measured at 5 kHz weekly. (a-1, a-2, a-3) Shear wave images acquired each week. (b-1, b-2, b-3) Shear stiffness maps (adapted from (103)).

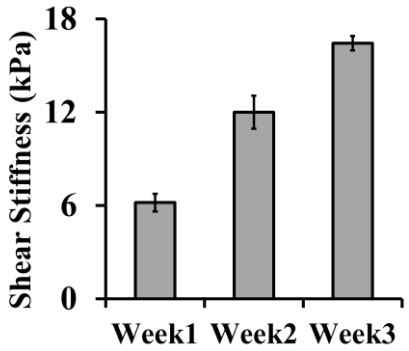

Figure 5.8. Shear stiffness of pellets during the 3-week culture period. The plotted values represent mean ± standard deviation (n = 6 at each time point) (adapted from (103)).

A progressive accumulation in both collagen and PG was observed during the 3-week culture period (***Figure 5.9***). The collagen content rose progressively during the culture period (week 1: 0.08 ± 0.03%; week 2: 0.10 ± 0.04%; week 3:

0.16 ± 0.03%). The PG content increased from 0.53 ± 0.08% at week 1 to 0.88 ± 0.1% at week 3. The collagen and PG contents showed a significant increase from day 7 to day 21 ($p < 0.05$).

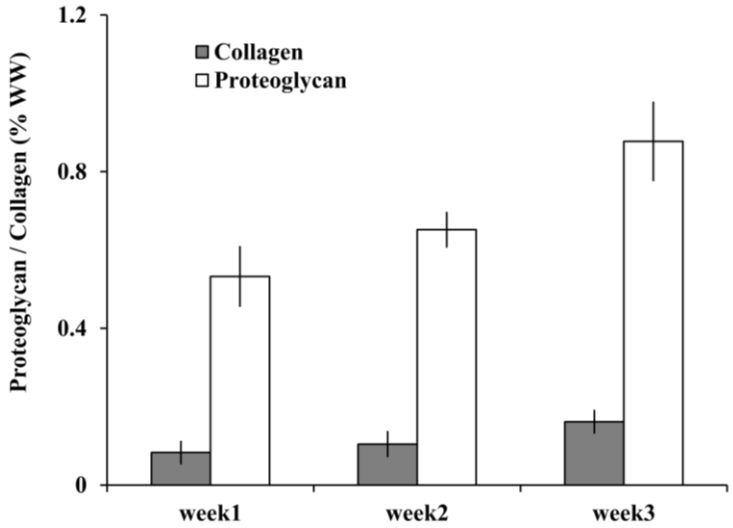

Figure 5.9. Accumulation of PG and collagen in the pellets over 3 weeks (n = 5 per time point) (adapted from (103)).

Pearson's correlation analysis revealed that the shear stiffness of the chondrocyte pellets was linearly related to PG and to collagen contents (***Figure 5.10***), while shear stiffness increased with increasing matrix content over the 3-week culture period. Specifically, the measured shear stiffness was highly correlated with both PG and collagen (r = -0.881 and -0.851, respectively).

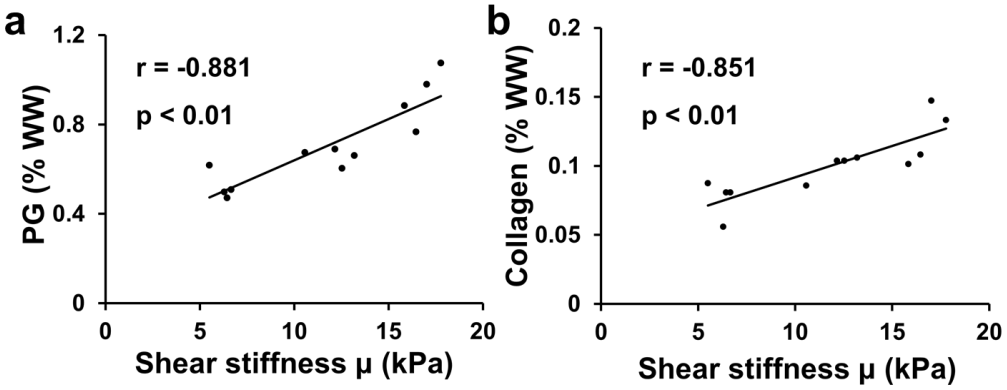

Figure 5.10. Correlations between MRE-derived shear stiffness and the corresponding (a) PG and (b) collagen contents. The correlation coefficients and the corresponding p-values are shown in each graph (adapted from (103)).

5.4 Discussion and Conclusion

The present study shows that micro-MRE with geometric focusing is able to nondestructively measure the shear stiffness of tissue-engineered cartilage under high-frequency (e.g., 5 kHz) shear loading. Micrometer shear wave motion was introduced into the constructs using geometric focusing excitation. The acquired MR wave images encode shear displacements and wave motion. Measurement of cyclic shear wave motions in the constructs provides the quantitative shear stiffness maps. Such maps can be used to monitor the formation of the ECM during tissue development.

Given that reliable estimation of shear stiffness requires the ability to detect at least half a wavelength in the measurement region, MRE measurement of tissue-engineered cartilage is often challenged by the small size (diameter less than 5 mm) and high stiffness (shear modulus greater than 50 kPa) of the material.

The small and stiff samples need a higher driven frequency to reduce the spatial wavelength. For example, the shear wavelength of 0.7% agarose gel is much smaller at a driven frequency of 5 kHz (0.7 mm) than at 550 Hz (5.5 mm) (7,62). Considering a stiff sample (100 kPa) with a diameter of 2 mm, which are typical properties for tissue-engineered cartilage, and using 1000 kg/m^3 for the density, then according to ***Eq. 3.11***, the mechanical actuator should be driven at a frequency of 2.5 kHz or higher to ensure that at least half a wavelength is visible. While previous micro-MRE studies reported by *Othman et al.* have used surface excitation of gels in NMR tubes to study the development of engineered bone and fat constructs at frequencies up to 2 kHz (95-98), the wave penetration using surface excitation is diminished by an increase in wave attenuation at higher frequencies. The advantage of geometric focusing micro-MRE is its ability to compensate for rapid wave attenuation at higher frequencies (> 2.5 kHz). *Yasar et al.* have used the agarose and Ecoflex phantoms to show that geometrically focused shear waves at 5 kHz result in a more uniform amplitude throughout the entire region within the tube, compared with the application of shear waves from the medium surface which attenuate exponentially in amplitude (61,62).

In this study, micro-MRE with geometric focusing was first applied to alginate beads embedded in agarose gel, demonstrating its sensitivity to the changes of shear properties. The calcium cross-linked alginate beads were used because their mechanical properties could be easily modified. *LeRoux et al.* have reported that the dynamic shear modulus of the 2% (w/v) alginate gel fell by 84% over 15 hours in a bath of physiological NaCl and $CaCl_2$ when compared with the

gels placed in a $CaCl_2$ solution (102). And the concentrations of NaCl (0.15 M) and $CaCl_2$ (1.8 mM) in their study were chosen to match their respective concentrations in DMEM culture media. Since, *in vitro* micro-MRE requires mechanical coupling between the sample and the mechanical actuator, a hydrogel (e.g. agarose gel) is needed to transfer the shear wave motion from the actuator to the embedded samples. In our study, we found that by preparing the agarose with tissue culture medium, the shear stiffness of beads decreased over time. This decrease in shear stiffness is likely due to the loss of crosslinking over time from the competition between the calcium ions and non-crosslinking cations (e.g. K+, Na+, Mg^2+, etc.) in the medium. As the crosslinks were lost, the alginate beads swelled over time (***Figure 5.5b-1, b-2, b-3***) with an associated decrease in the solid volume fraction of alginate. In contrast, the alginate beads were found to be mechanically stable in agarose gel formed with 1 mM $CaCl_2$. The shear stiffness of the alginate beads embedded in medium-base gel were within the range (dynamic shear modulus of 1-2 kPa after 15 h in 0.15 M NaCl) reported by *LeRoux et al* and *Wan et al* (20,102).

For the chondrocyte pellet experiments, we prepared the agarose gel by making it with the tissue culture medium to maintain chondrocyte cell viability by minimizing osmotic and pH changes between the cell pellets and the supporting gels. The mechanical stability of pellets embedded in the medium-based gel was confirmed by the MRE measurements of pellets over 4 hours. However, to be safe, all MRE experiments were conducted in less than one hour to minimize any potential interference.

The shear stiffness values of chondrocyte pellets measured from micro-MRE method are also comparable with other *ex vivo*, but non-MRE, mechanical studies (20,92,105). *Graff et al.,* for example, measured an increase from 15.6 kPa to 50.7 kPa in the equilibrium compressive moduli of chondrocyte pellets over a 3-week culture period (105). It should be noted that in *Graff et al.*'s study, the investigators used a high cell density (1.6 million cells/ pellet) which exhibited a high synthetic rate – more than 3-folds of proteoglycan and collagen content per pellet – than was used in our study (0.5 million cells/ pellet). *Stading et al.* measured the complex shear modulus of PGA (polyglycolic acid)-based constructs under dynamic shear tests over an 8-week culture period. Their study found that the storage modulus increased from 1 kPa at week 1 to 15 kPa at week 8 (92). In another study reported by *Wan et al.*, the dynamic shear moduli of cell-seeded alginate constructs (30 million cells/mL) increased from 4 kPa at day 1 to 20 kPa at day 40 (20).

For structure-function correlations, *Stading et al.* reported a power law relationship between the shear properties and ECM components in a PGA-based cartilage construct over a 56-days culture period (92). And *Wan et al.* empirically determined an exponential relationship in their alginate-based cartilage constructs cultured over 40 days (20). In the present study, however, a linear relationship was found between the shear stiffness and ECM components in the chondrocyte pellets over 21 days. The linear dependence reported here may therefore only reflect the contributions of ECM constituents to the shear stiffness of the chondrocyte pellets over a shorter culture period (21 days), and a nonlinear relationship may develop

with following a longer culture time. As chondrocytes proliferated and secreted both proteoglycan and collagen, the development of a continuous matrix in the pellets was monitored by the shear stiffness, which expresses the elastic stiffness resulting from the solid ECM deformation. If the matrix were absent, the shear stiffness would only reflect the elastic properties of the chondrocyte pellets. Therefore, as the ECM structure develops in the sample, the shear stiffness would be expected to increase with increasing proteoglycan and collagen contents.

In this study, we used the LFE algorithm to estimate the wavelength and calculate the shear stiffness. The LFE technique has been shown to be a robust, noise-insensitive inversion because of the sophisticated multi-scale data averaging in the estimation. By using this method, the correct estimation is reached using only half a wavelength in a given region. It should be noted that there are 'holes' in the stiffness maps (***Figure 5.5c-3***, and ***Figure 5.7b-1, b-2, b-3***), which correspond to regions that LFE failed to estimate the wavelength. For example, in ***Figure 5.5c-3***, the shear stiffness can not be calculated in the center of the beads. Although geometric focusing is designed to compensate for wave attenuation, when the stiffness of the beads decreased to 2 kPa, the shear waves may dampen too fast in the center of the beads for accurate wavelength estimation. In ***Figure 5.7b-1***, the stiffness of the chondrocyte pellet at the right bottom corner cannot be determined. This may be due to the presence of a noticeable air bubble next to the right edge (***Figure 5.11***), which was accidently trapped while making the gel. Since an air bubble can generate a magnetic susceptibility artifact that extends beyond its diameter and shear waves cannot propagate in the air, the air bubble could

result in a noticeable wave distortion in the pellet next to it, and significantly affect the stiffness reconstruction around it.

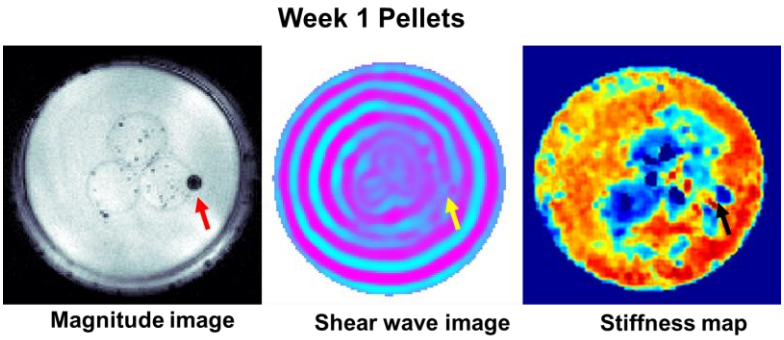

Figure 5.11. (a) Magnitude image, (b) shear wave image, and (c) stiffness map of week-1 pellets. A noticeable air bubble was found next to the bottom right pellet, which is indicated by the red arrowhead.

In addition to the restrictions on sample size and stiffness – discussed above – our micro-MRE system with geometric focusing exhibits other limitations from characteristic of MRI systems. For example, the inner diameter of the sample container (d) places a constraint on the maximum measurable wavelength $\lambda_s \leq 2d$, while the MR system resolution (Δx) places a constraint on the minimum measureable wavelength $\lambda_s \geq 2\Delta x$. Nevertheless, the primary advantages of MRE are that it does not require tissue sectioning and that it can provide a quantitative tissue stiffness map throughout an engineered construct. Thus, micro-MRE has the potential to address many of the needs expressed by tissue engineers for direct

monitoring and mapping of the mechanical properties of engineered tissue *in vitro* and *in situ*.

This chapter demonstrates that micro-MRE with geometric focusing can be used to nondestructively assess the shear properties of tissue-engineered cartilage at high frequencies (e.g., 5 kHz). The measured shear stiffness is sensitive to the formation of the solid ECM components (PG and collagen) during tissue development.

6 SIMULTANEOUS ACQUISITION OF MR RELAXATION, DIFFUSION, AND ELASTOGRAPHY

6.1 Introduction

As introduced in above chapters, MR Elastography (MRE) is a rapidly developing technology that can quantitatively assess tissue stiffness through the analysis of mechanically induced low-frequency shear waves (25). The MRE-derived tissue stiffness reflects the structural organization of cells and surrounding extracellular matrix. The changes in the compositional and structural integrity of tissue is depicted by the shear stiffness, which are the basis of the MRE contrast. To date MRE is useful in a variety of applications, from distinguishing normal versus diseased hepatic tissues to characterizing mechanical maturation of engineered cartilage tissue (26,103). In addition to MRE, $T_{1\rho}$ relaxation time and apparent diffusion coefficient (ADC) have been shown to be sensitive to the changes of the composition and structure of tissue matrix, respectively. $T_{1\rho}$ is sensitive to the slow molecular interactions between the water molecules and cartilage-specific macromolecules. The ADC explores the random motion of water molecules restricted by cell membranes and macromolecules. Combining MRE with MRI diffusion and $T_{1\rho}$ exploit differences in tissue cellularity and structure between different stages of engineered cartilage tissues. Given that $T_{1\rho}$, ADC, and MRE can probe differences in tissue composition, structure, and mechanical properties between different stages of engineered cartilage tissues (introduced in ***chapters 4*** and ***5***), it is natural to anticipate situations where three MR

methodologies may need to be employed. Therefore, it is necessary to design a way to increase the efficiency of MR characterization of engineered tissues.

Currently, conventional $T_{1\rho}$, diffusion, and MRE acquisitions are performed as separate measurements that prolong the imaging protocols, as shown in ***Chapters 2*** and ***3***. More specifically, in MRE, the harmonic mechanical vibration of the tissue is encoded into the phase part of MR signal through the application of synchronized motion-sensitizing gradients (MSG). Then the mechanical properties are recovered from the acquired phase data (25,26). In MRI diffusion, the random diffusive motion of water molecules induces MR signal loss with the application of bipolar diffusion-sensitizing gradients (46,47). In $T_{1\rho}$ relaxation measurement, the application of $T_{1\rho}$ preparatory spin-locking (SL) pulse to causes a $T_{1\rho}$ relaxation decay in MR signal (35,41). Among these three MR methods, MRE and diffusion MRI are motion sensitive techniques and encode the motion of the spins separately into the phase and magnitude part of MR signal, respectively. $T_{1\rho}$, rather than using any motion-sensitizing gradients, uses an independent preparatory pulse prior to any imaging sequence to induce signal loss in MR signal magnitude.

In this work, two new methods were introduced to acquire (1) MRE and diffusion MRI data, and (2) MRE and $T_{1\rho}$ MRI data simultaneously. Simultaneous acquisition of MRE and MRI data will reduce the scan time and allow immediate co-registration of elastogram and diffusion map or elastogram and $T_{1\rho}$ map, and even facilitate clinical assessment after transplantation. For simultaneous diffusion and MRE acquisition, the application of MSG causes a change of the MR signal

phase arise from intravoxel coherent spin motions, while the incoherent part of motion due to diffusion can be encoded simultaneously into the MR signal magnitude. In this approach, the bipolar gradients are used as both diffusion-sensitizing and motion-sensitizing gradients (dMSG). This approach is described as diffusion-MRE (dMRE). For simultaneous $T_{1\rho}$ and MRE acquisition, the application of SL pulse only affect the energy transfer between the spins and surrounding lattice, and has no effect on spins' translational motion induced by voxel vibration in MRE. Thus, $T_{1\rho}$ and MRE can be separately encoded into the magnitude and phase part of MRI signal by applying both SL pulse and MSG simultaneously. The $T_{1\rho}$ SL preparatory pulse is placed prior to a conventional MRE sequence. This method is described as $T_{1\rho}$-MRE. These two methods are validated in a soft tissue-mimicking phantom.

6.2 Theory

6.2.1 dMRE Theory

The dMRE technique is based on a conventional MRE pulse sequence; however, the timing is chosen such that the MSGs are sensitive to both the coherent and incoherent intravoxel motion. A diagram of the dMRE sequence is shown in ***Figure 6.1***. In dMRE, two symmetrical gradients (MSGs) are inserted on each side of the 180° refocusing pulse. In order to ensure MSGs are sensitive to both coherent and incoherent intravoxel motion, the diffusion time Δ must satisfy a time constraint given by (106)

$$\Delta = nT + \delta, (n = 1,2,3,...) \quad [6.1]$$

where T and δ are the period of the vibration and the gradient duration, respectively.

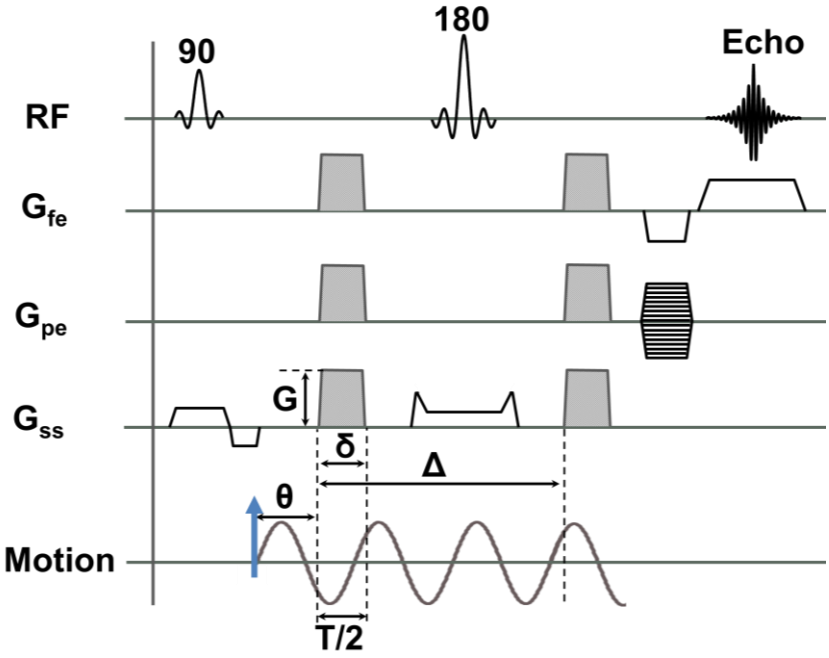

Figure 6.1. The dMRE pulse sequence diagram based on a SE readout. The diffusion/motion-sensitizing gradients (shaded regions) can be applied along any desired axis (adapted from (106)).

Considering an ideal rectangular gradient with δ = T/2, in the presence of simple coherent, harmonic excitation, all spins will move coherently between two gradients resulting a net phase shift given by ***Eq. 3.5*** for the case N = 1 where N is the number of MSG (52). Consequently, the effect of MRE coherent motion on detected MR signal is given by

$$\Phi_{MRE} = \exp(i\phi(\mathbf{r},\theta)) = \exp\left[i \frac{2\gamma T(\mathbf{G}\cdot\boldsymbol{\varepsilon}_0)}{\pi} \sin(\mathbf{k}\cdot\mathbf{r}+\theta) \right] \qquad [6.2]$$

where **k** is the wave number, ξ_0 is the peak displacement of the isochromat from its mean position, T is the angular frequency of the external vibration, and θ is the initial phase offset, **G** is the magnetic gradient vector, and **r** is the displacement vector. It is evident that the coherent harmonic motion will cause only a phase change rather than a signal decay.

Diffusion represents incoherent random motion with each spin moving independently. Due to the large number of spins involved and the Gaussian nature of diffusion, there is no net phase change. In the case of free diffusion and a pulse gradient waveform, the MR signal attenuation E_{Diff} is given by (46) (also explained in ***Chapter 2***, ***section 2.3.3***):

$$E_{Diff} = \exp(-\gamma^2 G^2 \delta^2 (\Delta - \delta/3) D) = \exp(-bD) \qquad [6.3]$$

where b is the diffusion weighting b-factor.

Therefore, in dMRE measurements, the acquired MRI signal detected at TE with normalizing to the signal obtained when G = 0, can be given by:

$$E(G,TE) = \frac{S(G,TE)}{S(G=0,TE)} = E_{Diff}(G,TE)\Phi_{MRE}(G,TE) \qquad [6.4]$$

where $E_{Diff}(G,TE)$ is the signal decay due to diffusion, and $\Phi_{MRE}(G,TE)$ represent the effect of harmonic motion on the MR signal. The harmonic vibration and diffusion can be encoded simultaneously and detected separately in the phase and in the magnitude of the MR signal.

Since diffusion and MRE motion-encoding gradient can be applied along any directions, the dMRE technique can be extended to the case of simultaneous

acquisition of DTI and 3D MRE: DTI-MRE (107,108). For example, 12 gradient directions can be chosen for DTI, which are uniformly distributed in 3D space (109). The twelve directions are clustered into four groups according to criterion (***Eq. 6.5***), allowing one to assign a unit vector e_i^p to each direction, with j = 1,2,3, and p being the group index p = 1,2,3,4. The directions are assigned to a group by the criterion that the function of scalar products (***Eq. 6.5***) is minimized.

$$\min \sum_{p=1}^{N_s} (\left|e_1^p \cdot e_2^p\right| + \left|e_1^p \cdot e_3^p\right| + \left|e_2^p \cdot e_3^p\right|) \qquad [6.5]$$

In doing so, the dMRE can be extended to the case of DTI-MRE.

6.2.2 $T_{1\rho}$-MRE Theory

A diagram of the $T_{1\rho}$-MRE sequence is shown in ***Figure 6.2***, where a $T_{1\rho}$ preparatory pulse cluster is placed before a MRE sequence. As in conventional MRE, the coherent, harmonic motion of spins is encoded into the MR phase signal by using MSGs. As introduced in ***6.2.1***, the coherent harmonic motion will cause only a phase change but no MR magnitude signal decay.

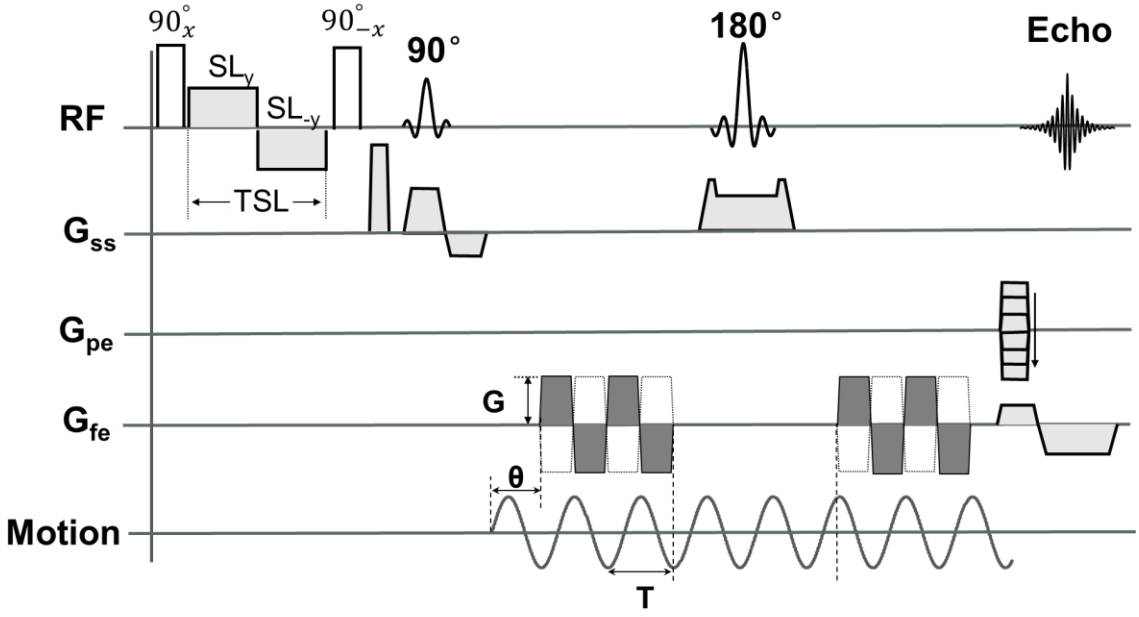

Figure 6.2. The $T_{1\rho}$-MRE pulse sequence diagram based on a SE-MRE sequence. The $T_{1\rho}$ self-compensation preparatory pulse clusters are place in front the MRE sequence.

In $T_{1\rho}$-MRE, the $T_{1\rho}$ self-compensation SL pulse clusters placed before the RF excitation enable the spin relaxation along the B_1 field of SL pulse (see ***section 2.2.2***). The application of SL pulse creates a new environment that affect spins' energy transfer with the lattice. This results a signal decay with the time constant $T_{1\rho}$. The intensity of the measured magnetization is given by (35),

$$M(t) = M_0[\exp(\frac{-t}{T_{1\rho}})]. \qquad [6.6]$$

where t is the duration of the SL pulse. It can be seen that $T_{1\rho}$ SL pulse only cause magnitude decay instead of net phase change.

Since the harmonic vibration and $T_{1\rho}$ relaxation have independent mechanism, by applying both SL pulse and MSGs simultaneously, these two phenomena can be encoded simultaneously and detected separately in the magnitude and phase part of the MR signal. The acquired MRI signal can be given by:

$$M(t) = M_0[\exp(\frac{-t}{T_{1\rho}})]\exp(i\phi_{MRE}(\mathbf{r},\theta)) \quad [6.7]$$

6.3 Material and Methods

6.3.1 Sample Preparation

The tissue-mimicking phantom (n = 3) consists of a spherical bead (1.5 cm diameter) embedded in a mixture of agarose and gelatin gel. The beads were formed from rehydration of dehydrated beads (Rainbow Water Beads, Greenville, SC) by immersion in distilled water for 12 hours. The liquid crystalline polymer in dehydrated beads can absorb water to form spherical beads. The background gel was made by mixing 4% (w/v) food grade gelatin (Knox) with 0.75% (w/v) agarose (SeaKem LE Agarose, Lonza, Rockland, ME), and dissolving in distilled water at 90°C. An individual bead was embedded in the mixture gel in a cylindrical plastic container (inner diameter = 30 mm; height = 40 mm) at 37°C. The phantoms were allowed to congeal overnight at 4°C prior to start of the measurements. ***Figure 6.3*** demonstrates the schematic structure of the phantom.

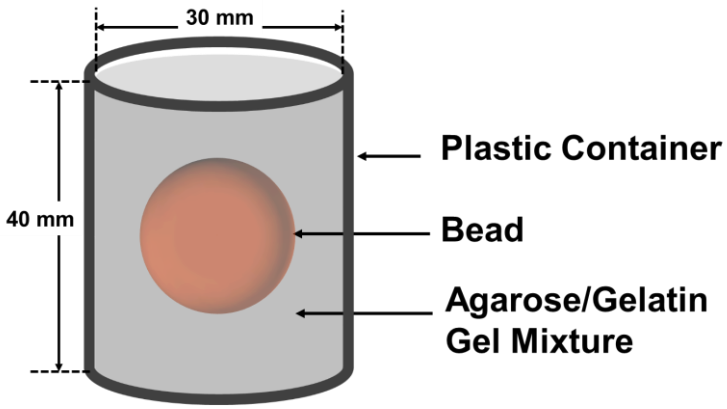

Figure 6.3. Schematic drawing of bead-gel phantom prepared in a cylindrical plastic container.

6.3.2 Experimental Setup and Pulse Sequence Control

All experiments were performed on a horizontal bore 9.4 T (400 MHz) Agilent animal MR scanner (310/ASR, Agilent Technologies, Santa Clara, CA) with self-shielded gradient coils (maximum gradient of 100 G/cm), and a 39 mm diameter quadrature RF coil. The scanner platform is Agilent Vnmrj 4.0. The MRI scanner is shown in ***Figure 6.4***.

Figure 6.4. Agilent 9.4 T MRI scanner.

The design and implantation of the micro-MRE actuation system can be found in previous publications (106). The agarose-filled container was attached to a preloaded piezo-actuator (P-840.1, Physik Instrumente (PI) GmbH & Co. KG, Germany), which was fixed to a plastic cradle and placed horizontally inside the center of the RF coil (see ***Figure 6.5***). The piezo-actuator was excited with an amplified sinusoidal waveform at a frequency of 500 Hz. The mechanical vibrations generated by the actuator were transmitted to the sample via the horizontal vibration of the plastic rod and wall of the sample container, resulting in a concentric wave pattern within the gel. This experimental setup also establishes concentric wave patterns within the gel, as in geometric focusing system introduced in ***5.2.2*** (61).

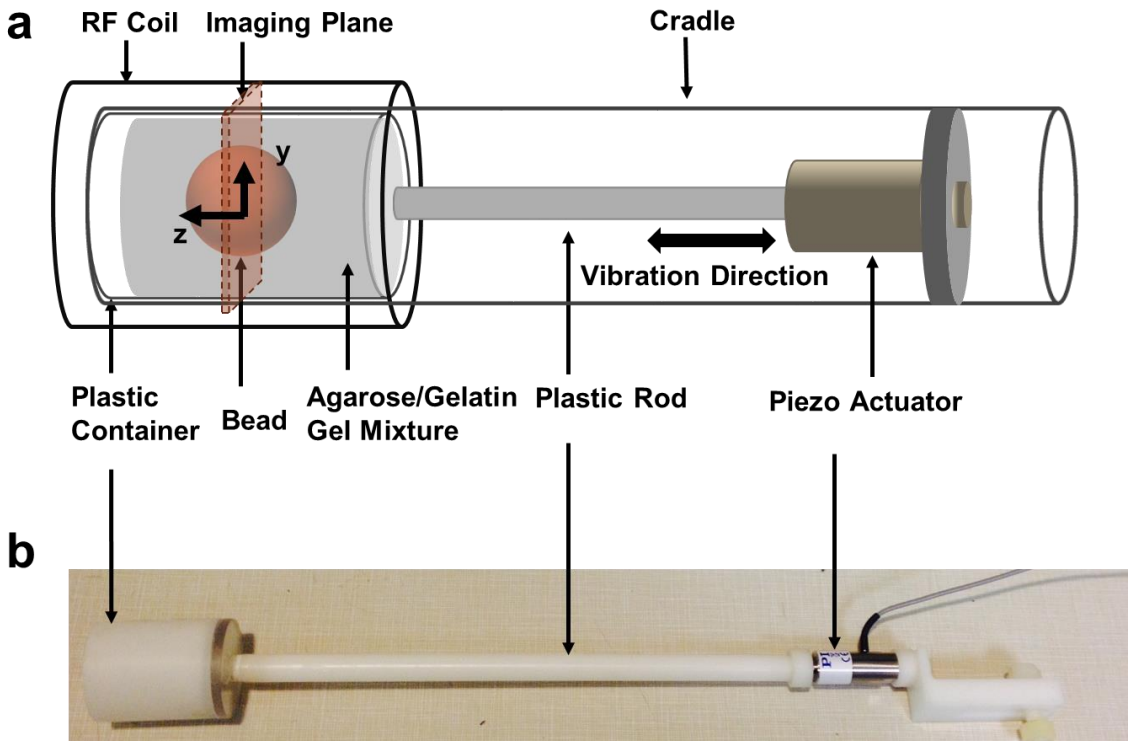

Figure 6.5. (a) Schematic diagram of the MRE excitation setup in the MRI scanner. The dashed plane indicates the position of the image plane (adapted from (106)). (b) Photography of MRE excitation setup.

a. dMRE Measurement

In this study, dMRE was performed based on a manufacturer supplied spin-echo imaging sequence (SEMS, Agilent). The sequence was developed with two symmetrical dMSGs inserted on each side of the 180° refocusing pulse. The diffusion time Δ was set as described in ***Eq. 6.1*** to allow the simultaneous encoding of MRE and diffusion. For MRE experiment, a series of four phase images was acquired by shifting the phase offset θ between the motion and the dMSG over one vibration period. Correspondingly, in order to obtain different b-values for ADC

measurement, the gradient amplitude was adjusted from one acquisition to the next.

Our new technique can be used with a variety of gradient waveforms as long as the timing is in accordance with the condition imposed by ***Eq. 6.1***. The shape, number, and duration of the gradient lobes can be adjusted flexibly to modulate the encoding efficiency of MRE and diffusion, respectively. As shown in ***Figure 6.6***, three waveforms were investigated in this study. (1) A trapezoidal gradient commonly used in conventional diffusion experiment. (2) An oscillating waveform with one and a half lobes on each side used to enhance the MRE encoding efficiency by a factor of three over multiple cycles of the synchronous gradients. (3) A camel-shaped waveform with only two positive lobes used to increase the diffusion encoding efficiency by a factor of four. The expression of the b-factor for each waveform is described in ***Appendix A***.

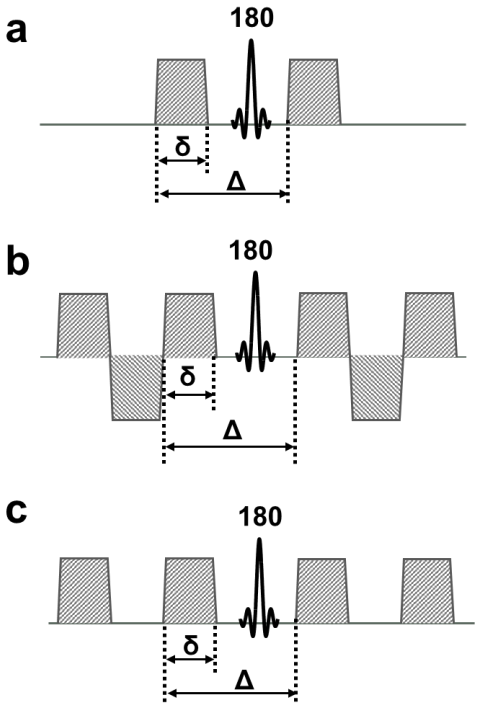

Figure 6.6. Three gradient waveforms used for dMRE encoding. (a) Single cycle trapezoidal waveform. (b) Oscillating waveform with one and a half lobes on each side. (c) Camel-shaped waveform with only two positive lobes (adapted from (106)).

The acquisition parameters were: TE/TR = 42/1000 ms; FOV = 4 cm × 4 cm; matrix size = 128×128; one axial slice; lice thickness = 2 mm; MRE frequency = 500 Hz; dMSG lobe duration δ = 1 ms; diffusion time Δ = 31 ms; 4 MRE time steps; 4 b-values = 100, 200, 500, and 1000 s/mm^2. For each gradient waveform, four different gradient amplitudes were employed at each MRE time step to maintain the same b-values. Algebraic details of which are provided in the ***Appendix A***: single trapezoid gradient: (0, 21.80, 31.24, 50.86, and 72.65 G/cm); one and one-half cycles of oscillating gradient: (0, 21.39, 30.66, 49.91, and 71.31 G/cm); and camel-shaped gradient: (0, 10.02, 14.36, 23.38, and 33.40 G/cm). Phase difference images were acquired with two acquisitions (inverted gradient

polarity) for each MRE time step. With an additional B0 image (b = 0 s/mm^2) for the ADC fitting, the dMRE measurement results in nine images with the total scan time of 19 minutes.

For comparison, conventional MRE and diffusion experiments were performed using a SE-MRE sequence and a SE-diffusion sequence, respectively, with the standard waveform of a single trapezoid lobe. The SE-MRE sequence is identical to the dMRE sequence except that the gradient amplitude was kept constant (40 G/cm) at each of the four time steps, corresponding to b = 347 s/mm^2, and when no scan was performed at b = 0 s/mm^2. The duration of SE-MRE was 17 minutes. The SE-diffusion measurement was performed without vibration and thus without an additional acquisition block with inverted gradient polarity as in dMRE. Acquisition time of the five b-values in SE-diffusion was 10 minutes and 40 sec resulting in a total measurement time of the comparative experiments of approximately 28 minutes. In all experiments, the dMSGs were applied along the slice direction, which represents the principle direction of vibration in our experimental setup.

b. $T_{1\rho}$-MRE Measurement

While $T_{1\rho}$-MRE is feasible using any type of readout sequences, the experiments in this study were performed using on a modified manufacturer supplied fast spin-echo imaging sequence (FSEMS, Agilent). The sequence was designed by placing a self-compensation pulse cluster before a FSE-MRE pulse sequence with the oscillating trapezoid gradient waveform (***Figure 6.7***). The duration of the SL pulse (TSL) is incremented while the amplitude of SL is fixed.

For MRE experiment, a series of four phase images was acquired by shifting the phase offset θ between the motion and the MSG over one vibration period. The number of TSL steps is set to be equal to the number of MRE time steps. The TSL was adjusted from one acquisition to the next for $T_{1\rho}$ measurement.

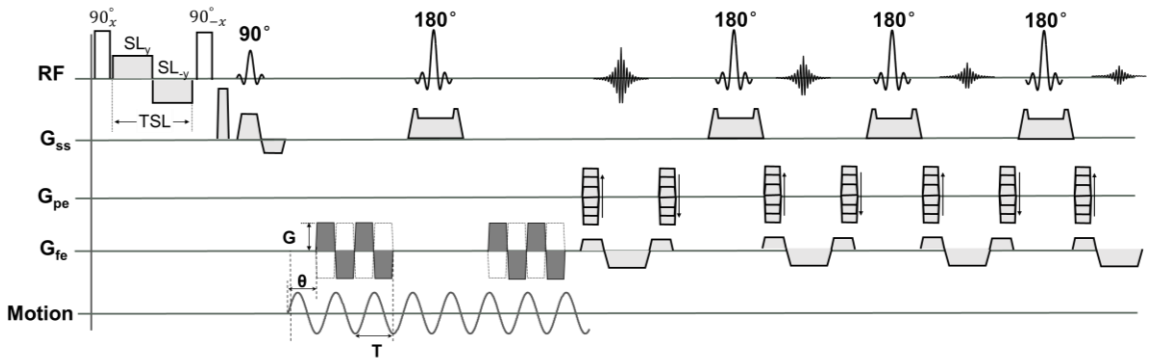

Figure 6.7. The diagram of $T_{1\rho}$ self-compensation MRE-FSE pulse sequence with echo train length (ETL) of 4 in one TR.

The acquisition parameters were: TR/TE = 1000/14 ms; SL frequency = 500 Hz; TSL = 0, 30, 80, and 150 ms; 4 MRE time steps; MSG frequency = 500 Hz; MSG cycles = 2; amplitude of MSG = 50 G/cm; vibration frequency = 500 Hz; FOV = 4 cm × 4 cm; matrix size = 128×128; one axial slice; slice thickness = 1.5 mm; ETL = 4. Four time steps were acquired for the vibration acquisition. Four different TSL were set at each MRE time step. At each time step, phase difference images were acquired with two acquisitions (inverted gradient polarity) for each MRE time step in order to reduce systematic phase errors. The total scan time of the $T_{1\rho}$-MRE experiment was 8 minutes and 34 seconds.

For comparison, conventional $T_{1\rho}$ and MRE experiments were performed using a FSE-$T_{1\rho}$ sequence and a FSE-MRE sequence, respectively, with the same acquisition parameters. The duration of FSE-MRE was 8 minutes and 34 seconds. The FSE-$T_{1\rho}$ measurement was performed without vibration and thus without an additional acquisition block with inverted gradient polarity as in $T_{1\rho}$-MRE. Acquisition time with four TSL was 4 minutes and 18 sec resulting in a total measurement time of the comparative experiments of approximately 13 minutes. In all experiments, the MSGs were applied along the slice direction, which represents the principle direction of vibration in our experimental setup.

6.3.3 Data Analysis

Custom toolbox was written in MATLAB (Mathworks, MA, USA) to analyze the MR data (see ***Figure 4.10*** and ***Figure 5.3***). For data analysis, selecting ROIs covered the entire regions of embedded samples. The $T_{1\rho}$ and ADC values were calculated through the exponential fitting of averaged MR signal to ***Eqs. 2.13*** and ***2.17***, respectively. The individual map was created on a pixel-by-pixel basis using exponential fitting.

The shear stiffness values were calculated according to ***Eq. 3.11***. The wavelengths λ were estimated using a 2D local frequency estimation (LFE) algorithm (104). The shear stiffness maps were created on a pixel-by-pixel basis. It should be noted that in dMRE, the gradient amplitude was different at each time step. Therefore, in dMRE, the accumulated MR signal phase was compensated for by the different encoding efficiency as illustrated in ***TABLE I***. Here, the MRE encoding efficiency is calculated by using the gradient waveform illustrated in

Figure 6.6a, in which G1, G2, G3, and G4 is gradient amplitude at each MRE time step. However, this is not the case in $T_{1\rho}$-MRE. All data are reported as mean ± standard deviation.

TABLE I. AN ILLUSTRATION OF DMRE COMPENSATION FACTOR WITH 4 TIME STEPS AND 4 DIFFERENT B-VALUES.

MRE Time Step	Gradient Amplitude	MRE Encoding Efficiency	Compensation Factor
1	G_1	$\frac{2}{\pi}\gamma T G_1$	$\times \frac{G_4}{G_1}$
2	G_2	$\frac{2}{\pi}\gamma T G_2$	$\times \frac{G_4}{G_2}$
3	G_3	$\frac{2}{\pi}\gamma T G_3$	$\times \frac{G_4}{G_3}$
4	G_4	$\frac{2}{\pi}\gamma T G_4$	$\times 1$

6.4 Results

6.4.1 dMRE Results

The diffusion data fitting for selecting ROI in the bead is plotted in ***Figure 6.8***. Here, data were obtained using single trapezoid gradient waveforms for both SE-diffusion and dMRE measurements. The image displayed in ***Figure 6.8*** corresponds to the magnitude image for a b-value of 500 s/mm^2 acquired from the dMRE measurements.

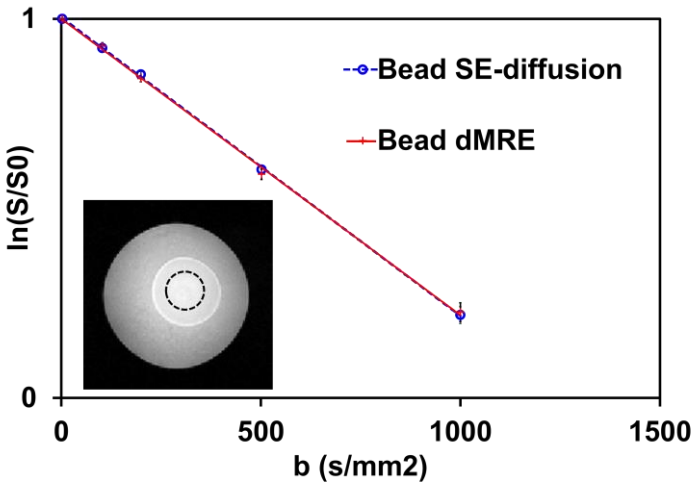

Figure 6.8. Normalized signal intensity plotted versus b for selected ROIs in the MR image in samples of bead, for both SE-diffusion and dMRE measurements acquired using single trapezoid gradient waveforms (adapted from (106)).

The corresponding ADC maps, complex wave images, and shear stiffness maps acquired from dMRE, SE-MRE, and SE-diffusion are shown in ***Figure 6.9***. It is apparent that tissue vibration does not interfere with the calculated diffusion parameters, as long as the timing constrains are satisfied. The averaged ADC values of the bead over ROIs were 1.75 ± 0.16 $\mu m^2/ms$ and 1.74 ± 0.16 $\mu m^2/ms$ for SE-diffusion and dMRE methods, respectively. The amplitude differences between the calculated displacements for the two methods were small (< 10%). The averaged shear stiffness of the beads, determined using LFE over the same ROIs, was 2.45 ± 0.23 kPa and 2.42 ± 0.20 kPa for SE-MRE and dMRE, respectively.

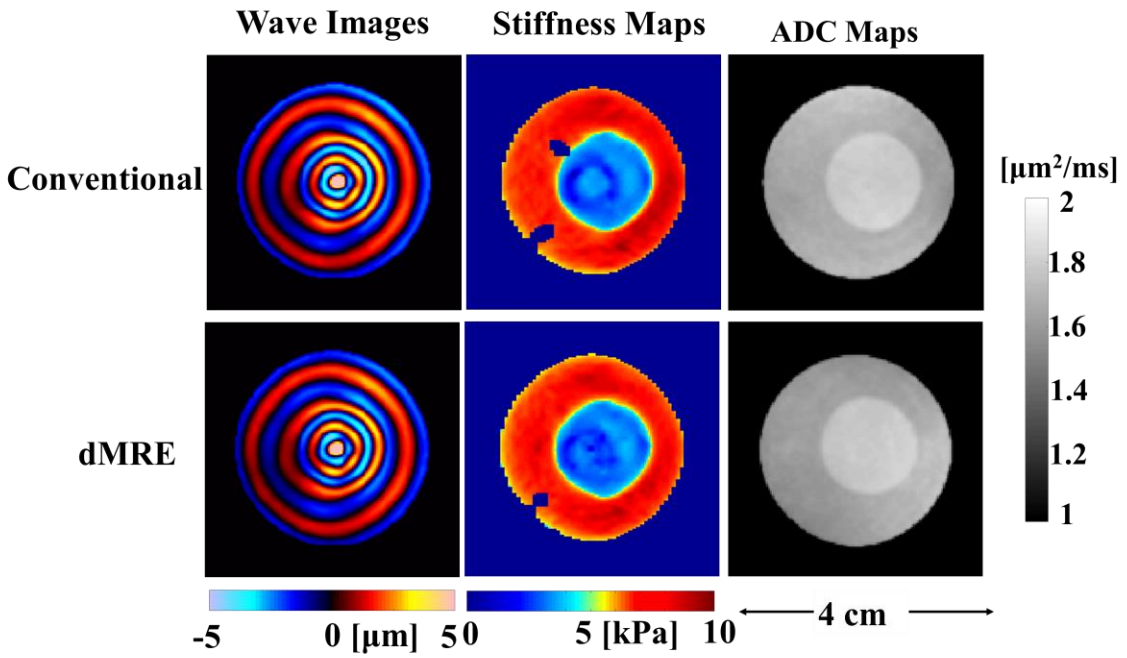

Figure 6.9. Complex wave images (left column), shear stiffness maps (middle column), and ADC maps (right column) at 500 Hz acquired with the conventional methods (top) and the dMRE (bottom) measurements, using single trapezoid gradient waveform (adapted from (106)).

A comparison of the ADC and the shear stiffness results acquired from SE-diffusion, SE-MRE, and using dMRE with different gradient waveforms is presented in ***TABLE II***. In all dMRE experiments, we observed no interference between the MRE and the diffusion acquisitions.

TABLE II. RESULTS OF ADC AND SHEAR STIFFNESS VALUES ACQUIRED FROM SE-DIFFUSION, SE-MRE, AND DMRE WITH THREE DIFFERENT GRADIENT WAVEFORMS.

	Sample (n = 3)	SE-diffusion (Single trapezoid gradient)	SE-MRE (Single trapezoid gradient)	dMRE (Single trapezoid gradient)	dMRE (Oscillating gradients)	dMRE (Camel-shaped gradients)
ADC ($\mu m^2/ms$)	Bead	1.75 ± 0.16	N/A	1.74 ± 0.16	1.75 ± 0.09	1.71 ± 0.10
	Gel	1.55 ± 0.11	N/A	1.56 ± 0.13	1.56 ± 0.12	1.56 ± 0.11
Shear Stiffness (kPa)	Bead	N/A	2.45 ± 0.23	2.42 ± 0.20	2.41 ± 0.24	2.39 ± 0.26
	Gel	N/A	7.22 ± 0.39	7.15 ± 0.77	7.48 ± 0.73	7.46 ± 0.59

6.4.2 $T_{1\rho}$-MRE Results

The $T_{1\rho}$ fitting for ROIs selected in the bead is plotted in ***Figure 6.10a***. The image displayed in ***Figure 6.10a*** corresponds to the magnitude image with TSL = 150 ms from the $T_{1\rho}$-MRE measurements. The corresponding $T_{1\rho}$ maps are shown in ***Figure 6.10b***. It is apparent that tissue vibration does not interfere with the calculated $T_{1\rho}$ values. The averaged values of the bead over ROIs were 205 ± 3 ms and 208 ± 3 ms for conventional $T_{1\rho}$ and $T_{1\rho}$-MRE methods, respectively.

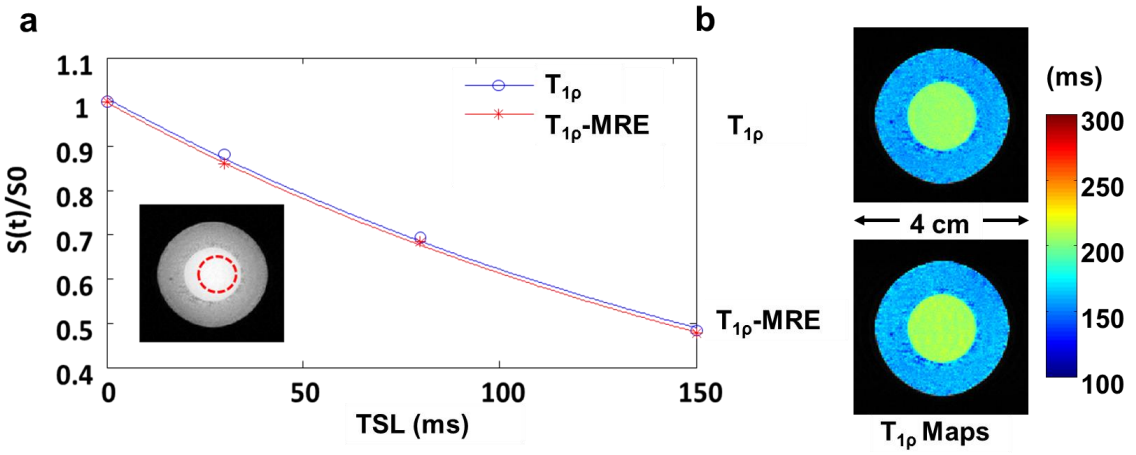

Figure 6.10. (a) Normalized signal intensity plotted versus TSL for selected ROIs in the MR image, for both $T_{1\rho}$ and $T_{1\rho}$-MRE measurements. (b) The corresponding $T_{1\rho}$ maps acquired from the $T_{1\rho}$ and $T_{1\rho}$-MRE measurements.

The complex wave images acquired from conventional MRE and $T_{1\rho}$-MRE acquisitions are shown in ***Figure 6.11***. The averaged shear stiffness of the beads, determined using LFE over the same ROIs, was 2.88 ± 0.2 kPa and 2.78 ± 0.2 kPa for conventional MRE and $T_{1\rho}$-MRE, respectively. The amplitude differences between the calculated displacements for the two methods were small (< 10%). A comparison of $T_{1\rho}$ values and the shear stiffness results acquired from conventional $T_{1\rho}$, MRE, and $T_{1\rho}$-MRE is presented in ***TABLE III***. In all $T_{1\rho}$-MRE experiments, we observed no interference between the MRE and the $T_{1\rho}$ acquisitions.

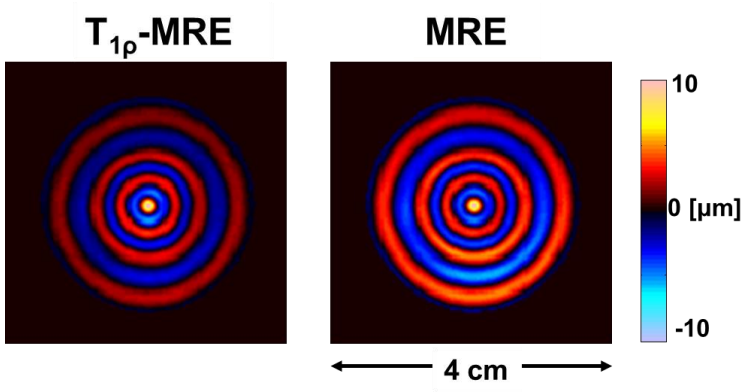

Figure 6.11. Complex wave images (real part) at 500 Hz acquired with the $T_{1\rho}$-MRE (left) and the conventional MRE (right) measurements.

TABLE III. RESULTS OF T_{1P} AND SHEAR STIFFNESS VALUES ACQUIRED FROM T_{1P}, MRE, AND T_{1P}-MRE MEASUREMENTS.

	Sample (n = 3)	**$T_{1\rho}$**	**MRE**	**$T_{1\rho}$-MRE**
$T_{1\rho}$ (ms)	Bead	205 ± 3	N/A	208 ± 3
	Gel	157 ± 5	N/A	158 ± 6
Shear Stiffness (kPa)	Bead	N/A	2.77 ± 0.2	2.77 ± 0.2
	Gel	N/A	8.82 ± 0.7	8.82 ± 0.7

6.5 Discussion and Conclusion

In this section, two new approaches (dMRE and $T_{1\rho}$-MRE) for simultaneous encoding are described. In the first approach, diffusion and MRE information are encoded into the magnitude and phase components of the MR signal, respectively; while in the second approach, $T_{1\rho}$ and MRE information are acquired in a similar manner. We used dMRE and $T_{1\rho}$-MRE in this phantom study to analyze a phantom

consisting of a spherical gel bead embedded in a background gel. We demonstrated that simultaneous acquisition is feasible with no observable interference between the two acquisitions.

Simultaneous dMRE and $T_{1\rho}$-MRE can provide the two pieces of information in a single scan. Thus, it requires less time than using separate, conventional acquisitions. However, the total time saved depends on the specific pulse sequence. In the present dMRE study, four time steps with two acquisitions (inverted gradient polarity) at each time step were acquired for the MRE acquisition, and an additional B0 image (b = 0 s/mm^2) for the ADC fitting, resulting in 9 images for the dMRE measurements. While maintaining the same acquisition parameters, 4 time steps with inverted gradient polarity in SE-MRE, and 5 b-values (including b = 0 s/mm^2) in SE-diffusion, the dMRE can save 30% time when compared with conventional methods. However, the time saving factor can be improved to 44-50% by omitting the second acquisition block for MRE by using an inverted polarity of the dMSG. In this case, the phase errors could be viewed on the DC component after the Fourier transformation of the phase images.

Furthermore, dMRE can readily be applied to other approaches of MRE and diffusion, such as 3D MRE (110), multi-frequency MRE (111), DTI (112) and HARDI (113), which require acquisitions at multiple frequencies or with the dMSGs oriented along multiple directions. In the current study, we have shown that observation of the timing constraint (***Eq. 6.1***) allows the simultaneous encoding of coherent spin motion due to vibration of the voxel and of incoherent spin motion within one voxel due to diffusion processes into the phase and the magnitude of

the MR signal, respectively. Therefore, we acquired the MRE information “for free” during the diffusion acquisition at one specific b-value (or vice versa the diffusion information during the MRE acquisition) without observable interference. The durations of individual diffusion MRI and MRE scans are similar. Hence, the measurement time saving factor of dMRE compared to applying MRE and diffusion MRI consecutively can be as high as 50%. As an example, a HARDI protocol, which applies dMSGs along 36 directions and which observes the dMRE timing constraint (***Eq. 6.1***), would enable the simultaneous acquisition of the 3D displacement field at a spectrum of three frequencies. In MRE, typically a minimum of four time steps is used for the derivation of the displacement vector. At each time step, the MSGs have to be applied along three linear independent directions. Thus, the full 3D displacement vector at a specific frequency can be derived from twelve dMRE direction acquisitions, while the gradients are oriented in mutually different directions. Consequently, 36 such acquisitions are needed for the measurement of the three-frequency vibration spectrum. Alternatively, instead of increasing the spectral range of MRE, the vibration frequency could be kept constant in the 36 acquisitions. Using this approach the determined mono-frequency 3D displacement vector would correspond to three averages. In essence, dMRE can potentially decrease the measurement time by a factor of two, since diffusion and MRE information are acquired simultaneously. Depending on the spectral range chosen in a specific study, the same vibration information may be acquired in various dMRE scans. While this would decrease the time saving

factor, these additional experiments can be used for increasing the SNR of the MRE wave images by averaging.

The time saving factor for $T_{1\rho}$-MRE also depends on the specific pulse sequence design. In the present study, four time steps with two acquisitions (inverted gradient polarity) at each time step were acquired for the MRE acquisition, resulting in 8 images for the $T_{1\rho}$-MRE measurements. While maintaining the same acquisition parameters, 4 time steps with inverted gradient polarity in conventional MRE, and four TSL in conventional $T_{1\rho}$, the $T_{1\rho}$-MRE can save 33% time when compared with conventional methods. However, the time saving factor can be improved to 50% by skipping the second acquisition block for MRE by using an inverted polarity of the MSG, as indicated in dMRE.

The proposed dMRE method relies on the timing constraint as described in ***Eq. 6.1***. Based on this condition, the shape, number, and duration of the gradient lobes can be adjusted to provide flexibility for the encoding efficiency. In the present study, three different gradient waveforms were investigated. The trapezoid gradient pulse shape is the most common waveform used for MRE and diffusion measurements. However, in dMRE, this waveform can lead to a low diffusion weighting b-factor particularly in the case of high MRE frequency, where a limited gradient strength is available. For example, if an MRE excitation frequency of 1 kHz is applied, the gradient lobe duration δ is set equal to half a period of the harmonic vibration (~ 0.5 ms) and diffusion time Δ is set equal to 30.5 ms. Then, when using the standard trapezoid gradient and a maximum gradient amplitude of 100 G/cm, as in our system, the maximum b-value achieved is only 543 s/mm^2. To

overcome this limitation, the camel-shaped gradient can be used to increase the diffusion weighting b-value by a factor of 4, i.e., to 2213 s/mm^2. In this case, compared with the single trapezoid gradient, the MRE encoding efficiency is increased by a factor of 2. In addition, when the oscillating gradient waveform with one and a half lobes on each side of the refocusing pulse is compared with the single trapezoid gradient, the MRE encoding efficiency is increased by a factor of 3 over multiple cycles of the synchronous gradients, while maintaining a similar diffusion weighting b-factor (555 s/mm^2). It should be noted that the increased number of gradient lobes requires a longer TE and thus lowers the signal, so the best waveform for a particular application depends on the optimization of this tradeoff. Another feature of the arrangement of dMSGs in dMRE is that it is not bound to a specific sequence type, but can be integrated into most pulse sequences typically used in MRE and diffusion MRI, such as the gradient-echo, spin-echo and EPI sequences.

In the presented dMRE measurements, the gradient amplitude was changed at each time step to achieve different b-values, which results in a different phase-to-noise ratio (PNR) in the MR phase signal, where the PNR is proportional to the SNR and to the gradient amplitude (37). It should be noted that in $T_{1\rho}$-MRE, the gradient amplitude for MRE is not changing, but the SNR at each time step is different due to $T_{1\rho}$ decay. Since the PNR is proportional to the SNR, $T_{1\rho}$-MRE also leads to a varying PNR at each time step. While the varying PNR did not show observable distortion in the MRE wave image reconstruction, this finding needs to be further studies at lower magnetic fields used in clinical scanners. Furthermore,

in this chapter, dMRE measurements were performed only in one direction. This is not a constraint on the method and dMRE can be easily extended to multiple directions allowing the simultaneous acquisition of DTI and MRE data, which will be further discussed in ***Chapter 7***. Although we observed no major deleterious interference in phantom experiments, these simultaneous acquisition methods must be more completely studied on a human clinical scanner. We speculate that the advantages of dMRE and $T_{1\rho}$-MRE may play a role in improving the use of MR relaxation, diffusion, and MRE for the characterization of the tissue-engineered cartilage during its development in future studies.

7 CONCLUSIONS

7.1 Summary

The ultimate goal of this study is to develop a combined MR relaxation, diffusion, elastography method to fully characterize the development of tissue-engineered cartilage in terms of the changes in its composition, structure, and mechanical properties during tissue growth.

In this study, in addition to the conventional T_2 and ADC, we have shown that $T_{1\rho}$ and MRE can be used as potential biomarkers to assess the specific changes in PG content and mechanical properties of engineered cartilage during tissue growth. For scaffold-free chondrocyte pellets, we observed the significant decreases (~ 33%) in $T_{1\rho}$, T_2, and ADC (***Figure 4.18***) and a significant increase in shear stiffness day 3 through day 21 (***Figure 5.8***). The measured changes were correlated with PG and collagen contents at different development stages (***Figure 4.20*** and ***Figure 5.10***). The stronger $T_{1\rho}$-PG correlation reflects the successful accumulation of PG in chondrocyte pellets as we expected. The strong T_2-collagen, T_2-PG, ADC-collagen, ADC-PG correlations reflect that the ECM becomes more organized with a general increase in PG and collagen contents, but the collagen network in tissue-engineered cartilage was not as heterogeneous as that in native tissues. Because in native cartilage tissue, T_2 is prone to the integrity of collagen network instead of PG distribution (***Figure 4.16***). ***Figure 7.1*** illustrates a proposed ECM diagram of tissue-engineered cartilage. The good correlation between shear stiffness and macromolecular contents also indicates that chondrocytes not only

simply secrete PG and collagen, but also form a continuous matrix structure with increased stiffness to deformation.

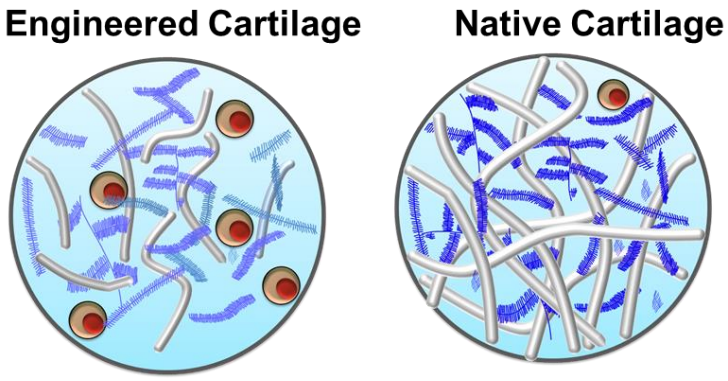

Figure 7.1. Schematic diagrams of ECM composition of the proposed engineered cartilage tissue (left) and native cartilage tissue (right). The collagen fibers in tissue-engineered cartilage are not heterogeneously oriented as in native cartilage tissue but of random nature.

Since MR relaxation, diffusion, and elastography exploit different aspects of properties of engineered tissues, to increase the efficiency of MR characterization of engineered tissues, in this study, we have developed two new methodologies for simultaneous acquisition of MRI and MRE data: (1) diffusion and MRE (dMRE) and (2) $T_{1\rho}$ and MRE ($T_{1\rho}$-MRE). In the first approach, diffusion and MRE information are encoded into the magnitude and phase components of the MR signal, respectively; while in the second approach, $T_{1\rho}$ and MRE information are acquired in a similar manner. These two methods allow simultaneous characterization of both biochemical and mechanical properties of biological

tissues. The feasibilities of the two new methods have been validated in tissue-mimicking phantoms. We demonstrated that simultaneous acquisition is feasible with no observable interference between the two acquisitions.

7.2 Contributions

This Ph.D. project focuses on the development of combined MR relaxation, diffusion, elastography methods for the characterization of tissue-engineered cartilage, and have several unique contributions.

Aim 1: Although there was one pervious study using $T_{1\rho}$ to compare a 8-week cartilage-tissue with native cartilage tissue, it only provided a single time-point measurement and did not show the change of $T_{1\rho}$ during the tissue development. To the best of our knowledge, this work provides the **first** $T_{1\rho}$ relaxation time characterization of the growth of engineered cartilage in an *in vitro* system (114). In this study, we have shown that $T_{1\rho}$ can be used as a potential biomarker to assess the specific changes in PG content of engineered cartilage during tissue growth.

Aim 2: This work provides the **first** MRE study of tissue-engineered cartilage (103). The geometric focusing MRE method was initially developed to compensate wave attenuations at higher excitation frequency. This work demonstrates that MRE with geometric focusing can be used to nondestructively assess the shear properties of tissue-engineered cartilage at high-frequencies (e.g. 5 kHz). The measured shear stiffness is sensitive to the formation of the solid ECM components (PG and collagen) during tissue development.

Aim 3: In this work, **two new** techniques (dMRE and $T_{1\rho}$-MRE) were proposed to allow the simultaneous acquisition of (1) diffusion and MRE (2) $T_{1\rho}$ and MRE (106). In dMRE, the pulse sequence timing is adjusted so that the shear wave motion and MR signal decay due to diffusion can be encoded into the phase and magnitude components of the MR signal by using the same pair of bipolar gradients. A **new** camel-shaped gradient was proposed to increase both the diffusion and MRE encoding efficiencies. In $T_{1\rho}$-MRE, MR signal decay arising from $T_{1\rho}$ relaxation and shear wave motion in MRE can be separately encoded into the magnitude and phase part of MRI signal by applying both SL pulse and MSGs simultaneously. The dMRE and $T_{1\rho}$-MRE could be applied not only to cartilage tissue engineering, but also to other kinds of tissue engineering, such as osteogenic and adipose tissue engineering, or other diseases associated with macromolecular/structural changes.

7.3 Limitations

A few limitations should be mentioned in this study.

Aim 1: We measured the $T_{1\rho}$, T_2, and ADC changes of tissue-engineered cartilage with the accumulation of both PG and collagen content. We showed that $T_{1\rho}$, T_2, and ADC can be used as potential biomarkers to biochemically characterize the matrix change. However, at this point, we have not fully separate out the individual contribution from each matrix component in our MRI results. Besides PG and collagen, which are major components of cartilage, three are other ECM components may also contribute to the final results. It is difficult so far to separate out the exact individual contribution from each component of matrix.

Aim 2: In this study, the LFE algorithm was used to estimate the shear stiffness, in which the local wavelength was estimated but wave attenuation was not accounted. The resulting shear stiffness then only represent the magnitude of shear modulus rather than the complex value. In order to extract the attenuation and shear modulus with a higher confidence level, other inversion algorithms such as, direction inversion of wave equation (57) and finite element analysis (115), should be investigated in the future studies. Such inversion methods require all the components of motion within samples in three orthogonal directions to ensure the accurate calculation. However, the MRE acquisition in the current work was performed in a single direction (out of plane) that captured only one component of the displacement. Future MRE experiments should be performed so that the MSG directions are varied to capture all three orthogonal components of displacement.

In addition, in order to apply geometric focusing μMRE to even stiffer materials, such as fully developed engineered constructs with the stiffness of native cartilage (MPa), higher mechanical excitation frequencies (i.e. above 9 kHz) are required. Furthermore, while μMRE itself is a nondestructive evaluation method, the current μMRE technique requires embedding the engineered constructs in a hydrogel for MRE force transduction. This prevents completely non-invasive measurements on intact tissue constructs. Further improvements in MRI hardware and the MRE mechanical excitation setup are needed to overcome these shortcomings, such as, an MRI compatible bioreactor with a small MRE actuator attached.

Aim 3: Although dMRE and $T_{1\rho}$-MRE have been successfully applied to tissue-mimicking phantoms, the performance of these simultaneous acquisition methods for characterization of tissue-engineered cartilage must be more completely studied in future work, not only *in vitro*, but also *in vivo*.

7.4 Recommendation for Future Work

There are some future directions that should be considered:

Aim 1: In future MRI study, multi-exponential T_2 analysis (76,116), $T_{1\rho}$ dispersion analysis (117), and fractional ordered calculus diffusion analysis (50) may be used as potential ways to investigate the individual contribution from each component to MR T_2 and $T_{1\rho}$ relaxation and diffusion signal.

Aim 2: Future 3D MRE studies should be performed to capture all three orthogonal components of displacement so that one can extract the attenuation and shear modulus with a higher confidence level. Moreover, multi-frequency MRE should also be considered to study the viscoelastic behaviors of engineered tissue systems (54).

Aim 3: The dMRE and $T_{1\rho}$-MRE methods should be applied to tissue-engineered cartilage in future studies, not only *in vitro*, but also *in vivo*. Moreover, the dMRE and $T_{1\rho}$-MRE could be applied not only to cartilage tissue engineering, but also to other kinds of tissue engineering, such as osteogenic and adipose tissue engineering, or other diseases associated with macromolecular/structural changes.

Furthermore, dMRE can be easily extended to multiple directions allowing the simultaneous acquisition of DTI and 3D MRE data, here shows an example of DTI-MRE data acquired from an *ex vivo* mouse brain tissue (***Figure 7.2***) (107,108). DTI-MRE enables the simultaneous acquisition of DTI and MRE data. While the presented *ex vivo* results indicate no interference between MRE and DTI acquisitions, the in vivo feasibility of DTI-MRE has to be verified in future studies.

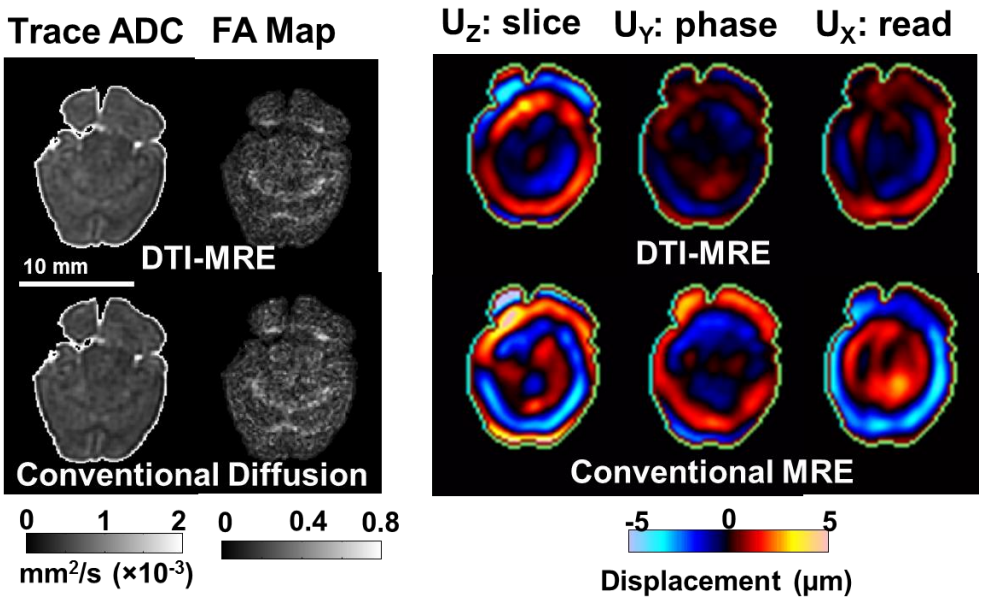

Figure 7.2. Comparison of DTI-MRE (top) and conventional acquisition schemes (bottom) in an *ex vivo* mouse brain. Similar maps of trace ADC, FA, and 3D wave field images were determined using DTI-MRE and conventional methods.

APPENDICES

APPENDIX A

Diffusion b-Factor Calculation for Three Gradient Waveforms

In diffusion MRI, the *b*-factor is used to characterize the sensitivity of MR signal decay to an arbitrary gradient waveform $G(t')$. For a pulse gradient spin echo pulse sequence, the *b*-factor is described by the following equation (37):

$$b = \gamma^2 \int_0^{TE} \left[\int_0^t G(t')dt' \right]^2 dt. \qquad \text{[A1]}$$

In the present dMRE work, three different gradient waveforms (trapezoid, oscillating, and camel-shaped, as shown in ***Figure 6.6***) were studied. Under the assumption that the ramp times are negligible, the three can be described by:

$$\begin{aligned} G_{trapezoid}(t) &= +|G|; t \in [0, T/2] \\ G_{oscillating}(t) &= \begin{cases} +|G|; t \in [0, T/2], [T, 3T/2] \\ -|G|; t \in [T/2, T] \end{cases} \\ G_{camel-shaped}(t) &= \begin{cases} +|G|; t \in [0, T/2], [T, 3T/2] \\ 0; t \in [T/2, T] \end{cases} \end{aligned} \qquad \text{[A2]}$$

where $T = 2\delta$, and δ is the gradient duration of one lobe. Substituting ***Eq. A2*** into ***Eq. A1*** and solving yields:

$$\begin{aligned} b_{trapezoid} &= (\gamma G \delta)^2 (\Delta - \delta/3) \\ b_{oscillating} &= (\gamma G \delta)^2 (\Delta + \delta) \\ b_{camel-shaped} &= (2\gamma G \delta)^2 (\Delta + 5\delta/6) \end{aligned} \qquad \text{[A3]}$$

APPENDIX A (continued)

where the diffusion time Δ is defined as illustrated in ***Figure 6.6***. When integrating the gradient time series, it should be noted that in all cases two dMSGs were used per acquisition (i.e., one on each side of the refocusing pulse).

As another example, if sinusoids are chosen as the basis set, then the gradient waveforms are given by:

$$\begin{aligned} G_{half-sine}(t) &= G\sin(\omega t), t \in [0, T/2] \\ G_{oscillating}(t) &= G\sin(\omega t), t \in [0, 3T/2] \\ G_{camel-shaped}(t) &= \begin{cases} G\sin(\omega t); t \in [0, T/2], [T, 3T/2] \\ 0; t \in [T/2, T] \end{cases} \end{aligned} \quad \text{[A4]}$$

where $\omega = 2\pi/T$, $T = 2\delta$, and δ is the gradient duration of one lobe. By following a similar analysis as in ***Eqs. A1-A3***, the resulting expressions for the *b* factor are:

$$\begin{aligned} b_{half-sine} &= \left(2\pi^{-1}\gamma G\delta\right)^2(\Delta - \delta/4) \\ b_{oscillating} &= \left(2\pi^{-1}\gamma G\delta\right)^2(\Delta + 5\delta/4) \\ b_{camel-shaped} &= \left(4\pi^{-1}\gamma G\delta\right)^2(\Delta + 7\delta/8) \end{aligned} \quad . \quad \text{[A5]}$$

APPENDIX B

Copyright From Mary Ann Liebert, Inc.

APPENDIX C

Copyright From John Wiley and Sons

JOHN WILEY AND SONS LICENSE
TERMS AND CONDITIONS
Aug 03, 2014

This is a License Agreement between Ziying Yin ("You") and John Wiley and Sons ("John Wiley and Sons") provided by Copyright Clearance Center ("CCC"). The license consists of your order details, the terms and conditions provided by John Wiley and Sons, and the payment terms and conditions.

All payments must be made in full to CCC. For payment instructions, please see information listed at the bottom of this form.

License Number	3441450141069
License date	Aug 03, 2014
Licensed content publisher	John Wiley and Sons
Licensed content publication	Magnetic Resonance in Medicine
Licensed content title	Simultaneous MR elastography and diffusion acquisitions: Diffusion-MRE (dMRE)
Licensed copyright line	Copyright © 2014 Wiley Periodicals, Inc.
Licensed content author	Ziying Yin,Richard L. Magin,Dieter Klatt
Licensed content date	Mar 19, 2014
Start page	1682
End page	1688
Type of use	Dissertation/Thesis
Requestor type	Author of this Wiley article
Format	Print and electronic
Portion	Full article
Will you be translating?	No
Title of your thesis / dissertation	MR Relaxation, Diffusion, and Stiffness Characterization of Engineered Cartilage Tissue
Expected completion date	Aug 2014

Expected size (number of pages)	155
Total	0.00 USD

Terms and Conditions

Terms and Conditions

This copyrighted material is owned by or exclusively licensed to John Wiley & Sons, Inc. or one of its group companies (each a"Wiley Company") or handled on behalf of a society with which a Wiley Company has exclusive publishing rights in relation to a particular work (collectively "WILEY"). By clicking accept in connection with completing this licensing transaction, you agree that the following terms and conditions apply to this transaction (along with the billing and payment terms and conditions established by the Copyright Clearance Center Inc., ("CCC's Billing and Payment terms and conditions"), at the time that you opened your Rightslink account (these are available at any time at http://myaccount.copyright.com).

Terms and Conditions

- The materials you have requested permission to reproduce or reuse (the "Wiley Materials") are protected by copyright.

- You are hereby granted a personal, non-exclusive, non-sub licensable (on a stand-alone basis), non-transferable, worldwide, limited license to reproduce the Wiley Materials for the purpose specified in the licensing process. This license is for a one-time use only and limited to any maximum distribution number specified in the license. The first instance of republication or reuse granted by this licence must be completed within two years of the date of the grant of this licence (although copies prepared before the end date may be distributed thereafter). The Wiley Materials shall not be used in any other manner or for any other purpose, beyond what is granted in the license. Permission is granted subject to an appropriate acknowledgement given to the author, title of the material/book/journal and the publisher. You shall also duplicate the copyright notice that appears in the Wiley publication in your use of the Wiley Material. Permission is also granted on the understanding that nowhere in the text is a previously published source acknowledged for all or part of this Wiley Material. Any third party content is expressly excluded from this permission.

- With respect to the Wiley Materials, all rights are reserved. Except as expressly granted by the terms of the license, no part of the Wiley Materials may be copied, modified, adapted (except for minor reformatting required by the new Publication), translated, reproduced, transferred or distributed, in any form or by any means, and no derivative works may be made based on the Wiley Materials without the prior permission of the respective

copyright owner. You may not alter, remove or suppress in any manner any copyright, trademark or other notices displayed by the Wiley Materials. You may not license, rent, sell, loan, lease, pledge, offer as security, transfer or assign the Wiley Materials on a stand-alone basis, or any of the rights granted to you hereunder to any other person.

- The Wiley Materials and all of the intellectual property rights therein shall at all times remain the exclusive property of John Wiley & Sons Inc, the Wiley Companies, or their respective licensors, and your interest therein is only that of having possession of and the right to reproduce the Wiley Materials pursuant to Section 2 herein during the continuance of this Agreement. You agree that you own no right, title or interest in or to the Wiley Materials or any of the intellectual property rights therein. You shall have no rights hereunder other than the license as provided for above in Section 2. No right, license or interest to any trademark, trade name, service mark or other branding ("Marks") of WILEY or its licensors is granted hereunder, and you agree that you shall not assert any such right, license or interest with respect thereto.

- NEITHER WILEY NOR ITS LICENSORS MAKES ANY WARRANTY OR REPRESENTATION OF ANY KIND TO YOU OR ANY THIRD PARTY, EXPRESS, IMPLIED OR STATUTORY, WITH RESPECT TO THE MATERIALS OR THE ACCURACY OF ANY INFORMATION CONTAINED IN THE MATERIALS, INCLUDING, WITHOUT LIMITATION, ANY IMPLIED WARRANTY OF MERCHANTABILITY, ACCURACY, SATISFACTORY QUALITY, FITNESS FOR A PARTICULAR PURPOSE, USABILITY, INTEGRATION OR NONINFRINGEMENT AND ALL SUCH WARRANTIES ARE HEREBY EXCLUDED BY WILEY AND ITS LICENSORS AND WAIVED BY YOU WILEY shall have the right to terminate this Agreement immediately upon breach of this Agreement by you.

- You shall indemnify, defend and hold harmless WILEY, its Licensors and their respective directors, officers, agents and employees, from and against any actual or threatened claims, demands, causes of action or proceedings arising from any breach of this Agreement by you.

- IN NO EVENT SHALL WILEY OR ITS LICENSORS BE LIABLE TO YOU OR ANY OTHER PARTY OR ANY OTHER PERSON OR ENTITY FOR ANY SPECIAL, CONSEQUENTIAL, INCIDENTAL, INDIRECT, EXEMPLARY OR PUNITIVE DAMAGES, HOWEVER CAUSED, ARISING OUT OF OR IN CONNECTION WITH THE DOWNLOADING, PROVISIONING, VIEWING OR USE OF THE MATERIALS REGARDLESS OF THE FORM OF ACTION, WHETHER FOR BREACH OF CONTRACT, BREACH OF WARRANTY, TORT, NEGLIGENCE, INFRINGEMENT OR OTHERWISE (INCLUDING, WITHOUT LIMITATION, DAMAGES BASED

ON LOSS OF PROFITS, DATA, FILES, USE, BUSINESS OPPORTUNITY OR CLAIMS OF THIRD PARTIES), AND WHETHER OR NOT THE PARTY HAS BEEN ADVISED OF THE POSSIBILITY OF SUCH DAMAGES. THIS LIMITATION SHALL APPLY NOTWITHSTANDING ANY FAILURE OF ESSENTIAL PURPOSE OF ANY LIMITED REMEDY PROVIDED HEREIN.

- Should any provision of this Agreement be held by a court of competent jurisdiction to be illegal, invalid, or unenforceable, that provision shall be deemed amended to achieve as nearly as possible the same economic effect as the original provision, and the legality, validity and enforceability of the remaining provisions of this Agreement shall not be affected or impaired thereby.

- The failure of either party to enforce any term or condition of this Agreement shall not constitute a waiver of either party's right to enforce each and every term and condition of this Agreement. No breach under this agreement shall be deemed waived or excused by either party unless such waiver or consent is in writing signed by the party granting such waiver or consent. The waiver by or consent of a party to a breach of any provision of this Agreement shall not operate or be construed as a waiver of or consent to any other or subsequent breach by such other party.

- This Agreement may not be assigned (including by operation of law or otherwise) by you without WILEY's prior written consent.

- Any fee required for this permission shall be non-refundable after thirty (30) days from receipt by the CCC.

- These terms and conditions together with CCCs Billing and Payment terms and conditions (which are incorporated herein) form the entire agreement between you and WILEY concerning this licensing transaction and (in the absence of fraud) supersedes all prior agreements and representations of the parties, oral or written. This Agreement may not be amended except in writing signed by both parties. This Agreement shall be binding upon and inure to the benefit of the parties' successors, legal representatives, and authorized assigns.

- In the event of any conflict between your obligations established by these terms and conditions and those established by CCCs Billing and Payment terms and conditions, these terms and conditions shall prevail.

- WILEY expressly reserves all rights not specifically granted in the combination of (i) the license details provided by you and accepted in the course of this licensing transaction, (ii) these terms and conditions and (iii) CCCs Billing and Payment terms and conditions.

- This Agreement will be void if the Type of Use, Format, Circulation, or Requestor Type was misrepresented during the licensing process.

- This Agreement shall be governed by and construed in accordance with the laws of the State of New York, USA, without regards to such states conflict of law rules. Any legal action, suit or proceeding arising out of or relating to these Terms and Conditions or the breach thereof shall be instituted in a court of competent jurisdiction in New York County in the State of New York in the United States of America and each party hereby consents and submits to the personal jurisdiction of such court, waives any objection to venue in such court and consents to service of process by registered or certified mail, return receipt requested, at the last known address of such party.

WILEY OPEN ACCESS TERMS AND CONDITIONS

Wiley Publishes Open Access Articles in fully Open Access Journals and in Subscription journals offering Online Open. Although most of the fully Open Access journals publish open access articles under the terms of the Creative Commons Attribution (CC BY) License only, the subscription journals and a few of the Open Access Journals offer a choice of Creative Commons Licenses:: Creative Commons Attribution (CC-BY) license Creative Commons Attribution Non-Commercial (CC-BY-NC) license and Creative Commons Attribution Non-Commercial-NoDerivs (CC-BYNC-ND) License. The license type is clearly identified on the article. Copyright in any research article in a journal published as Open Access under a Creative Commons License is retained by the author(s). Authors grant Wiley a license to publish the article and identify itself as the original publisher. Authors also grant any third party the right to use the article freely as long as its integrity is maintained and its original authors, citation details and publisher are identified as follows: [Title of Article/Author/Journal Title and Volume/Issue. Copyright (c) [year] [copyright owner as specified in the Journal]. Links to the final article on Wileys website are encouraged where applicable.
The Creative Commons Attribution License

The Creative Commons Attribution License (CC-BY) allows users to copy, distribute and transmit an article, adapt the article and make commercial use of the article. The CC-BY license permits commercial and non-commercial re-use of an open access article, as long as the author is properly attributed.

The Creative Commons Attribution License does not affect the moral rights of authors, including without limitation the right not to have their work subjected to derogatory treatment. It also does not affect any other rights held by authors or third parties in the article, including without limitation the rights of privacy and publicity. Use of the article must not assert or imply, whether implicitly or explicitly,

numbers, DOI and the link to the definitive published version on Wiley Online Library) should be maintained. Copyright notices and disclaimers must not be deleted.

- Any translations, for which a prior translation agreement with Wiley has not been agreed, must prominently display the statement: "This is an unofficial translation of an article that appeared in a Wiley publication. The publisher has not endorsed this translation."

Use by commercial "for-profit" organisations

Use of Wiley Open Access articles for commercial, promotional, or marketing purposes requires further explicit permission from Wiley and will be subject to a fee. Commercial purposes include:

- Copying or downloading of articles, or linking to such articles for further redistribution, sale or licensing;

- Copying, downloading or posting by a site or service that incorporates advertising with such content;

- The inclusion or incorporation of article content in other works or services (other than normal quotations with an appropriate citation) that is then available for sale or licensing, for a fee (for example, a compilation produced for marketing purposes, inclusion in a sales pack)

- Use of article content (other than normal quotations with appropriate citation) by for-profit organisations for promotional purposes

- Linking to article content in e-mails redistributed for promotional, marketing or educational purposes;

- Use for the purposes of monetary reward by means of sale, resale, licence, loan, transfer or other form of commercial exploitation such as marketing products

- Print reprints of Wiley Open Access articles can be purchased from:

  corporatesales@wiley.com

Further details can be found on Wiley Online Library http://olabout.wiley.com/WileyCDA/Section/id-410895.html

Other Terms anConditions: v1.9

You will be invoiced within 48 hours of this transaction date. You may pay your invoice by credit card upon receipt of the invoice for this transaction. Please follow instructions provided at that time.
To pay for this transaction now; please remit a copy of this document along with your payment. Payment should be in the form of a check or money order referencing your account number and this invoice number RLNK501368031. Make payments to "COPYRIGHT CLEARANCE CENTER" and send to:

Copyright Clearance Center
Dept 001
P.O. Box 843006
Boston, MA 02284-3006
Please disregard electronic and mailed copies if you remit payment in advance. Questions? customercare@copyright.com or +1-855-239-3415 (toll free in the US) or +1-978-646-2777.

Gratis licenses (referencing $0 in the Total field) are free. Please retain this printable license for your reference. No payment is required.

REFERENCES

1. Prevalence and most common causes of disability among adults--United States, 2005. Morb Mortal Wkly Rep. 2009;58(16):421-426.

2. Prevalence of doctor-diagnosed arthritis and arthritis-attributable activity limitation — United States, 2010–2012. Morb Mortal Wkly Rep. 2013;62(44):869-873.

3. Hunziker EB. Articular cartilage repair: basic science and clinical progress. A review of the current status and prospects. Osteoarthritis and cartilage / OARS, Osteoarthritis Research Society. 2002;10:432-463.

4. Huey DJ, Hu JC, Athanasiou KA. Unlike bone, cartilage regeneration remains elusive. Science. 2012;338:917-921.

5. Marcacci M, Filardo G, Kon E. Treatment of cartilage lesions: what works and why? Injury. 2013;44 Suppl 1:S11-15.

6. Mow VC, Ratcliffe A, Robin PA. Cartilage and diarthrodial joints as paradigms for hierarchical materials and structures. Biomaterials. 1992;13:67-97.

7. Buckwalter JA, Mankin HJ, Grodzinsky AJ. Articular cartilage and osteoarthritis. Instr Course Lect. 2005;54:465-480.

8. Buckwalter JA. Articular cartilage injuries. Clin Orthop Relat Res. 2002;402:21-37.

9. Mankin HJ. The response of articular cartilage to mechanical injury. J Bone Joint Surg Am. 1982;64:460-466.

10. Murphy L, Helmick CG. The impact of osteoarthritis in the United States: a population-health perspective: A population-based review of the fourth most common cause of hospitalization in U.S. adults. Orthop Nurs. 2012;31:85-91.

11. Temenoff JS, Mikos AG. Review: tissue engineering for regeneration of articular cartilage. Biomaterials. 2000;21:431-440.

12. Kuo CK, Li WJ, Mauck RL, Tuan RS. Cartilage tissue engineering: its potential and uses. Curr Opin Rheumatol. 2006;18:64-73.

13. Harrison RH, St-Pierre JP, Stevens MM. Tissue engineering and regenerative medicine: a year in review. Tissue Eng Part B Rev. 2014;20:1-16.

14. Chung C, Burdick JA. Engineering cartilage tissue. Adv Drug Deliv Rev. 2008;60:243-262.

15. Iwasa J, Engebretsen L, Shima Y, Ochi M. Clinical application of scaffolds for cartilage tissue engineering. Knee Surg Sports Traumatol Arthrosc. 2009;17:561-577.

16. Johnstone B, Alini M, Cucchiarini M, et al. Tissue engineering for articular cartilage repair--the state of the art. Eur Cell Mater. 2013;25:248-267.

17. Pelttari K, Wixmerten A, Martin I. Do we really need cartilage tissue engineering? Swiss Med Wkly. 2009;139:602-609.

18. Danisovic L, Varga I, Zamborsky R, Bohmer D. The tissue engineering of articular cartilage: cells, scaffolds and stimulating factors. Exp Biol Med (Maywood). 2012;237:10-17.

19. Mauck RL, Soltz MA, Wang CC, Wong DD, Chao PH, Valhmu WB, Hung CT, Ateshian GA. Functional tissue engineering of articular cartilage through dynamic loading of chondrocyte-seeded agarose gels. J Biomech Eng. 2000;122:252-260.

20. Wan LQ, Jiang J, Miller DE, Guo XE, Mow VC, Lu HH. Matrix deposition modulates the viscoelastic shear properties of hydrogel-based cartilage grafts. Tissue Eng Part A. 2011;17:1111-1122.

21. Lauterbur PC. Image formation by induced local interactions. Examples employing nuclear magnetic resonance. 1973. Clin Orthop Relat Res. 1989:3-6.

22. Bloembergen N, Purcell EM, Pound RV. Relaxation effects in nuclear magnetic resonance absorption. Phys Rev. 1948;73:679-712.

23. Knispel RR, Thompson RT, Pintar MM. Dispersion of proton spin-lattice relaxation in tissues. J Magn Reson (1969). 1974;14:44-51.

24. Brandl M, Haase A. Molecular diffusion in NMR microscopy. J Magn Reson, Series B. 1994;103:162-167.

25. Muthupillai R, Lomas DJ, Rossman PJ, Greenleaf JF, Manduca A, Ehman RL. Magnetic resonance elastography by direct visualization of propagating acoustic strain waves. Science. 1995;269:1854-1857.

26. Mariappan YK, Glaser KJ, Ehman RL. Magnetic resonance elastography: a review. Clin Anat. 2010;23:497-511.

27. Xu H, Othman SF, Magin RL. Monitoring tissue engineering using magnetic resonance imaging. J Biosci Bioeng. 2008;106:515-527.

28. Kotecha M, Klatt D, Magin RL. Monitoring cartilage tissue engineering using magnetic resonance spectroscopy, imaging, and elastography. Tissue Eng Part B Rev. 2013;19:470-484.

29. Hashemi RH, Bradley WG. MRI the basics. Pennsylvania: Lippincott Williams & Wilkins; 1997. p. 23.

30. Haacke EM, Brown RW, Thompson MR, Venkatesan R. Magnetic resonance imaging: physical principles and sequence design. New York City: John Wiley & Sons, Inc.; 1999. p. 17-47.

31. McRobbie DW, Moore EA, Graves MJ, Prince MR. MRI from picture to proton. United Kingdom: Cambridge; 2007. p. 137-179.

32. Dwek RA. Nuclear Magnetic Resonance in Biochemistry: Applications to Enzyme Systems: Oxford University Press; 1973.

33. Packer KJ, Dick DAT, Wilkie DR. The dynamics of water in heterogeneous systems [and discussion]. Phil Trans R Soc Lond B. 1977;278:59-87.

34. Redfield AG. Nuclear magnetic resonance saturation and rotary saturation in solids. Phys Rev. 1955;98:1787-1809.

35. Sepponen RE, Pohjonen JA, Sipponen JT, Tanttu JI. A method for T1rho imaging. J Comput Assist Tomogr. 1985;9:1007-1011.

36. Charagundla SR. T1ρ-weighted magnetic resonance imaging: Principles and diagnostic application. Appl Radiol. 2004;33:32-43.

37. Bernstein MA, King KF, Zhou XJ. Handbook of MRI pulse sequences. Burlington: Elsevier Academic Press; 2004.

38. Carr HY, Purcell EM. Effects of diffusion on free precession in nuclear magnetic resonance experiments. Phys Rev. 1954;94:630-638.

39. Meiboom S, Gill D. Modified spin-echo method for measuring nuclear relaxation times. Rev Sci Instrum. 1958;29:688-691.

40. Beall PT. NMR data handbook for biomedical applications: Pergamon Pr; 1984.

41. Charagundla SR, Borthakur A, Leigh JS, Reddy R. Artifacts in T1ρ-weighted imaging: correction with a self-compensating spin-locking pulse. J Magn Reson. 2003;162:113-121.

42. Fick A. Über diffusion. Ann Phys. 1855;94:59-86.

43. Brown R. A brief account of microscopical observations made in the months of June, July, and August, 1827, on the particles contained in the pollen of

plants; and on the general existence of active molecules in organic and inorganic bodies. Phil Mag. 1828;4:161–173.

44. Einstein A. Über die von der molekularkinetischen Theorie der wärme gefordete Bewegung von in ruhenden Flüssigkeiten suspendierten Teilchen. Ann Physik. 1905;4:549–560.

45. Johansen-Berg H, T.E.J. B. Diffusion MRI: From quantitative measurement to in-vivo neuroanatomy: Academic Press; 2009. p. 3-49.

46. Stejskal EO, Tanner JE. Spin diffusion measurements: spin echoes in the presence of a time-dependent field gradient. J Chem Phys. 1965;42:288-292.

47. Le Bihan D, Mangin JF, Poupon C, Clark CA, Pappata S, Molko N, Chabriat H. Diffusion tensor imaging: concepts and applications. J Magn Reson Imaging. 2001;13:534-546.

48. Niendorf T, Dijkhuizen RM, Norris DG, van Lookeren Campagne M, Nicolay K. Biexponential diffusion attenuation in various states of brain tissue: Implications for diffusion-weighted imaging. Magn Reson Med. 1996;36:847-857.

49. Bennett KM, Schmainda KM, Bennett RT, Rowe DB, Lu H, Hyde JS. Characterization of continuously distributed cortical water diffusion rates with a stretched-exponential model. Magn Reson Med. 2003;50:727-734.

50. Magin RL, Abdullah O, Baleanu D, Zhou XJ. Anomalous diffusion expressed through fractional order differential operators in the Bloch-Torrey equation. J Magn Reson. 2008;190:255-270.

51. Jensen JH, Helpern JA, Ramani A, Lu H, Kaczynski K. Diffusional kurtosis imaging: The quantification of non-gaussian water diffusion by means of magnetic resonance imaging. Magn Reson Med. 2005;53:1432-1440.

52. Muthupillai R, Rossman PJ, Lomas DJ, Greenleaf JF, Riederer SJ, Ehman RL. Magnetic resonance imaging of transverse acoustic strain waves. Magn Reson Med. 1996;36:266-274.

53. Doyley MM. Model-based elastography: a survey of approaches to the inverse elasticity problem. Phys Med Biol. 2012;57:R35.

54. Klatt D, Yasar TK, Royston TJ, Magin RL. Sample interval modulation for the simultaneous acquisition of displacement vector data in magnetic resonance elastography: theory and application. Phys Med Biol. 2013;58:8663-8675.

55. Yasar KT, Klatt D, Magin LR, Royston JT. Selective spectral displacement projection for multifrequency MRE. Phys Med Biol. 2013;58:5771-5781.

56. Parker KJ, Doyley MM, Rubens DJ. Imaging the elastic properties of tissue: the 20 year perspective. Phys Med Biol. 2011;56:R1.

57. Oliphant TE, Manduca A, Ehman RL, Greenleaf JF. Complex-valued stiffness reconstruction for magnetic resonance elastography by algebraic inversion of the differential equation. Magn Reson Med. 2001;45:299-310.

58. Manduca A, Oliphant TE, Dresner MA, Mahowald JL, Kruse SA, Amromin E, Felmlee JP, Greenleaf JF, Ehman RL. Magnetic resonance elastography: Non-invasive mapping of tissue elasticity. Med Image Anal. 2001;5:237-254.

59. Othman SF, Xu H, Royston TJ, Magin RL. Microscopic magnetic resonance elastography (mMRE). Magn Reson Med. 2005;54:605-615.

60. Knutsson H, Westin CF, Granlund G. Local multiscale frequency and bandwidth estimation. Image Processing Proceedings ICIP-94, IEEE International Conference, Austin, Texas, 1994. p. 36-40

61. Yasar TK, Royston TJ, Magin RL. Taking MR elastography (MRE) to the microscopic scale (mMRE). Biomedical Imaging: From Nano to Macro, 2011 IEEE International Symposium on, Chicago, IL, 2011. p. 1618-1623.

62. Yasar TK, Royston TJ, Magin RL. Wideband MR elastography for viscoelasticity model identification. Magn Reson Med. 2013;70:479-489.

63. Akella SVS, Regatte RR, Gougoutas AJ, Borthakur A, Shapiro EM, Kneeland JB, Leigh JS, Reddy R. Proteoglycan-induced changes in T1rho-relaxation of articular cartilage at 4T. Magn Reson Med. 2001;46:419-423.

64. Nieminen MT, Rieppo J, Toyras J, Hakumaki JM, Silvennoinen J, Hyttinen MM, Helminen HJ, Jurvelin JS. T2 relaxation reveals spatial collagen architecture in articular cartilage: a comparative quantitative MRI and polarized light microscopic study. Magn Reson Med. 2001;46:487-493.

65. Xia Y, Farquhar T, Burton-Wurster N, Vernier-Singer M, Lust G, Jelinski LW. Self-diffusion monitors degraded cartilage. Arch Biochem Biophys. 1995;323:323-328.

66. Potter HG, Foo LF. Magnetic resonance imaging of articular cartilage: trauma, degeneration, and repair. Am J Sports Med. 2006;34:661-677.

67. Regatte RR, Akella SV, Borthakur A, Kneeland JB, Reddy R. Proteoglycan depletion-induced changes in transverse relaxation maps of cartilage: comparison of T2 and T1rho. Acad Radiol. 2002;9:1388-1394.

68. Duvvuri U, Reddy R, Patel SD, Kaufman JH, Kneeland JB, Leigh JS. T1rho-relaxation in articular cartilage: effects of enzymatic degradation. Magn Reson Med. 1997;38:863-867.

69. Duvvuri U, Goldberg AD, Kranz JK, Hoang L, Reddy R, Wehrli FW, Wand AJ, Englander SW, Leigh JS. Water magnetic relaxation dispersion in biological systems: the contribution of proton exchange and implications for the noninvasive detection of cartilage degradation. Proc Natl Acad Sci U S A. 2001;98:12479-12484.

70. Potter K, Butler JJ, Adams C, Fishbein KW, McFarland EW, Horton WE, Spencer RGS. Cartilage formation in a hollow fiber bioreactor studied by proton magnetic resonance microscopy. Matrix Biol. 1998;17:513-523.

71. Potter K, Butler JJ, Horton WE, Spencer RGS. Response of engineered cartilage tissue to biochemical agents as studied by proton magnetic resonance microscopy. Arthritis Rheum. 2000;43:1580-1590.

72. Chen CT, Fishbein KW, Torzilli PA, Hilger A, Spencer RG, Horton WE, Jr. Matrix fixed-charge density as determined by magnetic resonance microscopy of bioreactor-derived hyaline cartilage correlates with biochemical and biomechanical properties. Arthritis Rheum. 2003;48:1047-1056.

73. Miyata S, Numano T, Homma K, Tateishi T, Ushida T. Feasibility of noninvasive evaluation of biophysical properties of tissue-engineered cartilage by using quantitative MRI. J Biomech. 2007;40:2990-2998.

74. Nugent AE, Reiter DA, Fishbein KW, McBurney DL, Murray T, Bartusik D, Ramaswamy S, Spencer RG, Horton WE, Jr. Characterization of ex vivo-generated bovine and human cartilage by immunohistochemical, biochemical, and magnetic resonance imaging analyses. Tissue Eng Part A. 2010;16:2183-2196.

75. Greco JB, Spencer RG. Cartilage growth in magnetic resonance microscopy-compatible hollow fiber bioreactors. In: Chaudhuri J, Al-Rubeai M, editors. Bioreactors for Tissue Engineering: Springer Netherlands; 2005. p. 135-163.

76. Irrechukwu ON, Reiter DA, Lin PC, Roque RA, Fishbein KW, Spencer RG. Characterization of engineered cartilage constructs using multiexponential T(2) relaxation analysis and support vector regression. Tissue Eng Part C Methods. 2012;18:433-443.

77. Reiter DA, Irrechukwu O, Lin PC, Moghadam S, Von Thaer S, Pleshko N, Spencer RG. Improved MR-based characterization of engineered cartilage using multiexponential T2 relaxation and multivariate analysis. NMR Biomed. 2012;25:476-488.

78. Novotny JE, Turka CM, Jeong C, Wheaton AJ, Li C, Presedo A, Richardson DW, Reddy R, Dodge GR. Biomechanical and magnetic resonance characteristics of a cartilage-like equivalent generated in a suspension culture. Tissue Eng. 2006;12:2755-2764.

79. Hardingham TE, Fosang AJ. Proteoglycans: many forms and many functions. FASEB J. 1992;6:861-870.

80. Cancedda R, Dozin B, Giannoni P, Quarto R. Tissue engineering and cell therapy of cartilage and bone. Matrix Biol. 2003;22:81-91.

81. Zhang Z, McCaffery JM, Spencer RGS, Francomano CA. Hyaline cartilage engineered by chondrocytes in pellet culture: histological, immunohistochemical and ultrastructural analysis in comparison with cartilage explants. J Anat. 2004;205:229-237.

82. Cheuk YC, Wong MW, Lee KM, Fu SC. Use of allogeneic scaffold-free chondrocyte pellet in repair of osteochondral defect in a rabbit model. J Orthop Res. 2011;29:1343-1350.

83. Petit B, Masuda K, D'Souza AL, et al. Characterization of crosslinked collagens synthesized by mature articular chondrocytes cultured in alginate beads: comparison of two distinct matrix compartments. Exp Cell Res. 1996;225:151-161.

84. Hsu EW, Schoeniger JS, Bowtell R, Aiken NR, Horsman A, Blackband SJ. A modified imaging sequence for accurate T2 measurements using NMR microscopy. J Magn Reson B. 1995;109:66-69.

85. Creemers LB, Jansen DC, van Veen-Reurings A, van den Bos T, Everts V. Microassay for the assessment of low levels of hydroxyproline. Biotechniques. 1997;22:656-658.

86. Xia Y. Relaxation anisotropy in cartilage by NMR microscopy (μMRI) at 14-μm resolution. Magn Reson Med. 1998;39:941-949.

87. Wheaton AJ, Borthakur A, Corbo M, Charagundla SR, Reddy R. Method for reduced SAR T1rho-weighted MRI. Magn Reson Med. 2004;51:1096-1102.

88. Erickson SJ, Prost RW, Timins ME. The "magic angle" effect: background physics and clinical relevance. Radiology. 1993;188:23-25.

89. Anderer U, Libera J. In vitro engineering of human autogenous cartilage. J Bone Miner Res. 2002;17:1420-1429.

90. Hayes WC, Bodine AJ. Flow-independent viscoelastic properties of articular cartilage matrix. J Biomech. 1978;11:407-419.

91. Little CJ, Bawolin NK, Chen X. Mechanical properties of natural cartilage and tissue-engineered constructs. Tissue Eng Part B Rev. 2011;17:213-227.

92. Stading M, Langer R. Mechanical shear properties of cell-polymer cartilage constructs. Tissue Eng. 1999;5:241-250.

93. Neu CP, Hull ML, Walton JH, Buonocore MH. MRI-based technique for determining nonuniform deformations throughout the volume of articular cartilage explants. Magn Reson Med. 2005;53:321-328.

94. Neu CP, Arastu HF, Curtiss S, Reddi AH. Characterization of engineered tissue construct mechanical function by magnetic resonance imaging. J Tissue Eng Regen Med. 2009;3:477-485.

95. Othman SF, Curtis ET, Plautz SA, Pannier AK, Butler SD, Xu H. MR elastography monitoring of tissue-engineered constructs. NMR Biomed. 2011;25:452-463.

96. Curtis ET, Zhang S, Khalilzad-Sharghi V, Boulet T, Othman SF. Magnetic resonance elastography methodology for the evaluation of tissue engineered construct growth. J Vis Exp. 2012;60:e3618.

97. Xu H, Othman SF, Hong L, Peptan IA, Magin RL. Magnetic resonance microscopy for monitoring osteogenesis in tissue-engineered construct in vitro. Phys Med Biol. 2006;51:719-732.

98. Othman SF, Xu H, Mao JJ. Future role of MR elastography in tissue engineering and regenerative medicine. J Tissue Eng Regen Med. 2013.

99. Lopez O, Amrami KK, Manduca A, Rossman PJ, Ehman RL. Developments in dynamic MR elastography for in vitro biomechanical assessment of hyaline cartilage under high-frequency cyclical shear. J Magn Reson Imaging. 2007;25:310-320.

100. Huang CC, Ravindran S, Yin Z, George A. 3-D self-assembling leucine zipper hydrogel with tunable properties for tissue engineering. Biomaterials. 2014;35:5316-5326.

101. Kuo CK, Ma PX. Maintaining dimensions and mechanical properties of ionically crosslinked alginate hydrogel scaffolds in vitro. J Biomed Mater Res A. 2008;84:899-907.

102. LeRoux MA, Guilak F, Setton LA. Compressive and shear properties of alginate gel: effects of sodium ions and alginate concentration. J Biomed Mater Res. 1999;47:46-53.

103. Yin Z, Schmid TM, Yasar TK, Liu Y, Royston TJ, Magin RL. Mechanical characterization of tissue-engineered cartilage using microscopic magnetic resonance elastography. Tissue Eng Part C Methods. 2014;20:611-619.

104. Manduca A, Muthupillai R, Rossman PJ, Greenleaf JF, Ehman RL. Image processing for magnetic-resonance elastography. Proc SPIE 2710, Medical Imaging 1996: Image Processing, Newport Beach, CA, 1996. p. 616-623.

105. Graff RD, Kelley SS, Lee GM. Role of pericellular matrix in development of a mechanically functional neocartilage. Biotechnol Bioeng. 2003;82:457-464.

106. Yin Z, Magin RL, Klatt D. Simultaneous MR elastography and diffusion acquisitions: Diffusion-MRE (dMRE). Magn Reson Med. 2014;71:1682-1688.

107. Yin Z, Richard LM, Klatt D. Extending diffusion-MRE (dMRE) to simultaneous measurement of DTI (diffusion tensor imaging) and MRE. Frontiers in Elastography Symposium, Urbana, Illinois, 2014. p. 23.

108. Klatt D, Yin Z, Magin LR. Simultaneous acquisition of diffusion MRI and MR elastography data. The 36th Annual International Conference of the IEEE Engineering in Medicine and Biology Society, Chicago, Illinois, 2014.

109. Jones DK, Horsfield MA, Simmons A. Optimal strategies for measuring diffusion in anisotropic systems by magnetic resonance imaging. Magn Reson Med. 1999;42:515-525.

110. Hirsch S, Klatt D, Freimann F, Scheel M, Braun J, Sack I. In vivo measurement of volumetric strain in the human brain induced by arterial pulsation and harmonic waves. Magn Reson Med. 2012. doi: 10.1002/mrm.24499.

111. Klatt D, Hamhaber U, Asbach P, Braun J, Sack I. Noninvasive assessment of the rheological behavior of human organs using multifrequency MR elastography: a study of brain and liver viscoelasticity. Phys Med Biol. 2007;52:7281-7294.

112. Basser PJ, Jones DK. Diffusion-tensor MRI: theory, experimental design and data analysis - a technical review. NMR Biomed. 2002;15:456-467.

113. Tuch DS, Reese TG, Wiegell MR, Makris N, Belliveau JW, Wedeen VJ. High angular resolution diffusion imaging reveals intravoxel white matter fiber heterogeneity. Magn Reson Med. 2002;48:577-582.

114. Yin Z, Schmid TM, Madsen L, Kotecha M, Magin RL. Monitoring the Formation of Tissue-Engineered Cartilage in Scaffold-Free Pellet Culture Using Magnetic Resonance Imaging. International Society for Magnetic

Resonance in Medicine (ISMRM) 20th Annual Meeting and Exhibition, Melbourne, Australia, 2012. p. 740.

115. Donald BP, Jonathan B, Abbas S, Justin S. Visualization and quantification of breast cancer biomechanical properties with magnetic resonance elastography. Phys Med Biol. 2000;45:1591.

116. Magin RL, Li W, Pilar Velasco M, Trujillo J, Reiter DA, Morgenstern A, Spencer RG. Anomalous NMR relaxation in cartilage matrix components and native cartilage: Fractional-order models. J Magn Reson. 2011;210:184-191.

117. Chen E-l, Kim RJ. Magnetic resonance water proton relaxation in protein solutions and tissue: T1r dispersion characterization. PLoS ONE. 2010;5(1):e8565.

VITA

Education

Doctor of Philosophy (Bioengineering), July 2014

University of Illinois at Chicago, Chicago, IL,

Dissertation: MR Relaxation, Diffusion, and Stiffness Characterization of Engineered Cartilage Tissue

Advisor: Richard L. Magin

Master of Science (Computer Application and Technology), July 2008

Beijing Jiaotong University, Beijing, China

Thesis: Design and Realization of Control System of High Intensity Focused Ultrasound System

Advisor: Bingyi Hu

Bachelor of Science (Biomedical Engineering), July 2006

Beijing Jiaotong University, Beijing, China

Thesis: Registration of Human Abdomen's Anatomical Image and CT Image

Advisor: Bingyi Hu

Research Experience

Research Assistant 2010 – 2014

Diagnostic Imaging System Group (DIS), Department of Bioengineering, University of Illinois at Chicago, Chicago, IL

Research Assistant & **Student Technician 2006 – 2008**

Biomedical Engineering lab, Beijing Jiaotong University, Beijing, China & Medsonic Medical Equipment Manufacturing Co., Ltd., Henan, China

Publications

Articles in Journals:

Z. Yin, R. L. Magin, and D. Klatt. Simultaneous MR Elastography and Diffusion Acquisitions: Diffusion-MRE (dMRE). Magn Reson Med, 71: 1682–1688. doi: 10.1002/mrm.25180. 2014.

C. Huang, S. Ravindran, **Z. Yin**, and A. George. 3-D Self-Assembling Leucine Zipper Hydrogel with Tunable Properties for Tissue Engineering. Biomaterials, 35(20):5316-26. doi: 10.1016/j.biomaterials. 2014.

Z. Yin, T. M. Schmid, T. K. Yasar, Y. Liu, T. J. Royston, and R. L. Magin. Mechanical Characterization of Tissue-Engineered Cartilage Using Microscopic Magnetic Resonance Elastography (μMRE). Tissue Eng Pt C: Methods, (in press). doi:10.1089/ten.TEC.2013.0408. 2013.

M. Kotecha, **Z. Yin**, and R. L. Magin. Monitoring Tissue Engineering and Regeneration by Magnetic Resonance Imaging and Spectroscopy. J Tissue Sci Eng S11:007. doi: 10.4172/2157-7552.S11-007. 2013.

Articles in Conference Proceedings:

B. Schwartz, **Z.Yin**, R.L. Magin. Mathematical Modeling of Multiply Connected Structures for Elastographic Imaging. 2014 Biomedical Engineering Society (BMES) Annual Meeting; 2014.

B. Duan, **Z. Yin**, L. Hockaday, R.L. Magin, J. Butcher. Dynamic Modulation Of Myofibroblast/Osteoblast Differentiation And Biomechanical Remodeling By Valve Interstitial Cells By Initial Tissue Stiffness. 2014 Biomedical Engineering Society (BMES) Annual Meeting; 2014. **Selected for Oral presentation.**

D. Klatt, **Z. Yin**, and R. L. Magin. Simultaneous Acquisition of Diffusion MRI and MR Elastography Data. 36th Annual International Conference of the IEEE Engineering in Medicine and Biology Society. Chicago, Illinois, USA; 2014

A.Q. Ye, P.L. Hubbard, Feng-Lei Zhou, **Z. Yin**, G.J.M. Parker, and R. L. Magin. Diffusion Tensor MRI Phantom Exhibits Anomalous Diffusion. 36th Annual International Conference of the IEEE Engineering in Medicine and Biology Society. Chicago, Illinois, USA; 2014

Z. Yin, Kaspar-Josche Streitberger, J. Guo, I. Sack, R. L. Magin, and D. Klatt. Diffusion Weighted MR Elastography (DW-MRE) of Glioblastoma Multiforme: A

New Way to Gain Quantitative Information from MRE Magnitude Data. Symposium of Frontiers in Elastography. Urbana, Illinois, USA; 2014.

Z. Yin, R. L. Magin, and D. Klatt. Extending Diffusion-MRE (dMRE) to Simultaneous Measurement of DTI (Diffusion Tensor Imaging) and MRE. Symposium of Frontiers in Elastography. Urbana, Illinois, USA; 2014.

Z. Yin, R. L. Magin, and D. Klatt. New Pulse Sequence Combining Diffusion MRI and MR Elastography (dMRE). Proc 22nd Annual Meeting ISMRM. Milan, Italy; 2014:0087. **Selected for PowerPoster presentation.**

A. Q. Ye, T. K. Yasar, A. Khan, **Z. Yin**, D. Klatt, T. J. Royston, and R. L. Magin. Application of SLIM-MRE on an In-Vivo Murine Model. Proc 22nd Annual Meeting ISMRM. Milan, Italy; 2014:7046.

A. Q. Ye, **Z. Yin**, T. K. Yasar, A. Khan, D. Klatt, and R. L. Magin. In vivo Monitoring of Chondrogenic Differentiation in Biomimetic Extracellular Matrix-Incorporated Scaffold via MRI. Proc of 2013 Biomedical Engineering Society (BMES) Annual Meeting; Seattle, Washington, USA; 2013.

Z. Yin, A. S. Lee, G. S. Van Thiel, V. Karas, K. Hussey, E. F. Shewman, D. R. Sumner, B. J. Cole, V. M. Wang, and R. L. Magin. Quantitative 11.7 T MRI and EPIC-μCT Assessment of Cartilage Repair in a Rabbit Glenohumeral Joint Model following Microfracture and Autologous Matrix Induced Chondrogenesis. Proc 21nd Annual Meeting ISMRM. Salt Lake City, UT, USA; 2013:436. **Selected for Oral presentation in MSK study group.**

Z. Yin, Y. Liu, T. M. Schmid, T. J. Royston, and R. L. Magin. Evaluation of Tissue Engineered Cartilage using Microscopic Magnetic Resonance Elastography. Proc 54th Annual Meeting ENC. Pacific Grove, CA, USA; 2013. **Selected for Oral presentation.**

W. M. Vincent, **Z. Yin**, A. Lee, G. S. Van Thiel, V. Karas, K. Hussey, E. F. Shewman, R. L. Magin, and B. J. Cole. Analysis of Cartilage Regeneration in a Rabbit Glenohumeral Joint Model following Microfracture and Autologous Matrix Induced Chondrogenesis using High-field (11.7 Tesla) MRI. Proc of 2013 Orthopaedic Research Society (ORS) Annual Meeting; San Antonio, TX, USA; 2013. **Selected for Oral presentation**.

Z. Yin, T. K. Yasar and R. L. Magin. Measurement of In Vitro Local Shear Stiffness of Alginate Beads Using Microscopic MR Elastography. Proc of 2012 Biomedical Engineering Society (BMES) Annual Meeting; Atlanta, GA, USA; 2012. **Selected for Oral presentation**.

M. Kotecha, **Z. Yin**, T. K. Yasar, D. Klatt, T. J. Royston, and R. L. Magin. High Field Magnetic Resonance Spectroscopy, Imaging and Elastography for Cartilage Tissue Engineering. Functional Imaging and Regenerative Medicine Workshop. Gaithersburg, MD, USA; 2012.

Z. Yin, T. M. Schmid, L. Madsen, M. Kotecha, R.L. Magin. Monitoring the Formation of Tissue-Engineered Cartilage in Scaffold-Free Pellet Culture Using Magnetic Resonance Imaging. Proc of 20nd Annual Meeting ISMRM; Melbourne, Australia; 2012:740.

Z. Yin, T. M. Schmid, M. Kotecha, and R. L. Magin. High-resolution T1ρ and T2 Maps of Articular Cartilage at 11.7 T. Proc 11th ICMRM Meeting; Beijing, China; 2011.

Patents

D. Klatt, **Z. Yin**, and R. L. Magin. “Simultaneous Acquisition of Diffusion Magnetic Resonance Imaging and Magnetic Resonance Elastography: Diffusion-MRE (dMRE),” 2013. Invention Disclosure at the University of Illinois at Chicago

B. Hu, Y. Li, **Z. Yin**, N. Liu and T. Yuan, “The Probe of Handheld OAE Measuring Instrument,” 2007 (No.: ZL 2006 2 0134075.X, issued in 2007).

Awards and Activities

ISMRM Member, 2012 - present

ISMRM Merit Award Summa Cum Laude, ISMRM abstract, 2014

ISMRM Merit Award Summa Cum Laude, ISMRM abstract, 2013

ISMRM Educational Stipend Award, 2012 – 2014.

The Glory honor graduate student, Beijing Jiaotong University, 2007

Mim-chueh Chang Scholarship, 2002